Probing the Large-scale Galaxy Density and Peculiar Velocity Fields

Kapukotuwe Walawwe Pulasthika Bethmini Senevirathne

Presented for the degree of

Master of Science

University of Glasgow

July 2010

This thesis is my own composition except where indicated in the text.

July 02, 2010

Bethmini Senevirathne

Abstract

This thesis focuses on constraining the linear redshift distortion parameter β, which is a critical variable in reconstructing the peculiar velocity field of the Local Universe and probing information of the distribution on dark matter. We used mock data samples of peculiar velocity fields that aim to mimic the next generation of galaxy peculiar velocity surveys such may become feasible for SKA and its precursors. The smoothed IRAS PSCz peculiar velocity field [Branchini et al., 1999] was used to generate the mock data samples, where the true value of β was considered to be 0.5 throughout this work (i.e. $\beta_{true} = 0.5$). The study was carried out considering two methods. First, we applied the χ^2 hypothesis test by comparing the observed and predicted peculiar velocity fields to constrain β from the mock peculiar velocity fields. In this case, the traditional distance indicators such as SNIa, TF and recently introduced gravitational wave standard sirens were considered. The distance scatter of each indicator was taken from literature and scatter in the predicted peculiar velocity (σ_v) was considered to be a variable. The best-fit value of β for the peculiar velocity models show a good agreement with β_{true} when $\sigma_v < 150$ km s^{-1}. Our calculations implied that, in order to fully exploit the potential of future improvement in the precision of β estimates, it is important also to improve the accuracy of the reconstructed peculiar velocity field predicted from all-sky redshift surveys. The second method is the ROBUST method originally introduced by Rauzy & Hendry for fitting peculiar velocity fields. The ROBUST method use the luminosity functions of the mock galaxies as the distance indicators, where the LF assumed to be independent of the spatial position of the galaxies. Our results are in a good agreement with $\beta_{true} = 0.5$, where the best fit values of the peculiar velocity models always centered around 0.5. Our results demonstrate the potential of the method, even in cases where the luminosity function is rather broad, provided it can be applied to sufficiently large peculiar velocity surveys - such as those which may be anticipated from e.g. the 6dF and WALLABY surveys in the relatively near future.

All things appear and disappear because of the concurrence of causes and conditions. Nothing ever exists entirely alone; everything is in relation to everything else. . . .

Lord Buddha

To my husband Sameera.....

Contents

List of Figures

List of Tables

Acknowledgments

I would like to express my sincere gratitude to my supervisor Dr. Martin A. Hendry for his help, advices and encouragement towards interesting topics, and for giving me the freedom to pursue it.

I gratefully acknowledge to Dr. Enzo Branchini (International School for Advanced Studies, Italy.) and Dr. D. J. Radburn-Smith (University of Washington) for providing us the data catalogues, which we used in this study.

My sincere thanks go to Dr. W. M. C. Sameera (University of Oxford) for his great support throughout my postgraduate studies.

I would like to thank present and past members of the Astronomy & Astrophysics Research Group in University of Glasgow, whose contribution has immensely benefited me in various ways in my work.

Preface

Cosmology is one of the most exciting fields in modern Physics because of the controversial concept of *dark matter* and *dark energy* - the origin and nature of which has not been completely established to date. The recent evidence explains that the dark energy accounts 3/4 of the matter and energy in the Universe. In 1998, the studies in type Ia Supernovae (SNIa) confirmed that the dark energy acts as anti-gravity that accelerates the expansion of the Universe (i.e. Λ CDM model) [Perlmutter et al., 1999]. The Infrared Astronomical Satellite (IRAS) Point Source catalogue redshift survey (PSCz) became a key role by providing information about 15,500 galaxies in nearby Universe. The future redshift surveys such as SKA and WALLABY would observe thousands of millions of objects, nourishing the analysis with a huge amount of data.

It is very important to use the large amount of available data to obtain well defined constraints on the constituent of the Universe, the evolution of growth perturbations, the expansion, whether it will expand forever, contract and collapse, or oscillate between expansion and contraction, and also the modification of gravity at large scales. The distribution of dark matter and dark energy plays a critical role in constructing cosmological models, and the development of such models is very important in understanding the fate of the Universe. The galaxy density and peculiar velocity field is a powerful probe of the distribution of dark matter in the Local Supercluster. This thesis basically aims to improve the present understanding about the distribution of dark matter *via* reconstructing the peculiar velocity field. Our main goal is to explore methods for constraining β, the linear redshift distortion parameter, which is one of the key aspects that needs a careful attention when reconstructing the galaxy

peculiar velocity field.

The outline of this thesis is organized as follows: Chapter 1 describes the basic theoretical aspects, which we need for our study. We describe the Freidmann equations, Gravitational instability, CMBR, redshift surveys and other important aspects along with the statistical applications we used for this study. Then the first part of Chapter 2 consists of a review for the linear redshift distortion parameter β. The studies in constraining β are accelerated in 1990s after the approach of the IRAS PSCz catalogue. The reconstruction methods for β are discussed and the differences between a density-density comparison (POTENT) and a velocity-velocity (VELMOD, ITF) comparison are explored. The application of POTENT favours a value of $\beta_I = 1.0$, while the VELMOD and ITF methods lead to a value of $\beta_I = 0.5$, which appeared to be more accurate.

In the later part of Chapter 2, we present our attempt of constraining β_I using a velocity-velocity comparison, where we apply the χ^2 hypothesis test for the calculations. We used the mock peculiar velocity field models that mimic the next generation of galaxy peculiar velocity surveys. With completeness and all-sky coverage the smoothed IRAS PSCz velocity field [Branchini et al., 1999] was used to generate the mock data and to provide a β-dependent predicted peculiar velocity field to compare with the observed radial peculiar velocities derived from combining observed red-shifts and redshift-independent estimates. We assumed that each mock galaxy position was coincident with one of the PSCz galaxies for simplicity. The traditional distance indicators SNIa, TF and the gravitational wave standard sirens have been considered for the distance and velocity measurements. We discuss about the information that would be essential to improve the accuracy of methods for reconstructing the peculiar velocity field, and our findings will be very useful in designing future redshift surveys such as those carried out by the SKA radio telescope and its precursors.

In Chapter 3, we present our work with the ROBUST method for fitting peculiar velocity models [Rauzy and Hendry, 2000]. Powerful statistical methods are very

important for the analysis of sparse and noisy distance and peculiar velocity surveys. Moreover, robust methods that require fewer prior assumptions concerning the distance indicator samples are very useful. Following this approach we present a new robust method for probing peculiar velocity field models based on a non-parametric treatment of the galaxy luminosity function. The basis of the method is to infer the *correct* peculiar velocity field as that which renders the corrected galaxy redshifts and luminosities as uncorrelated. We describe the application of this method for constraining the linear redshift-distortion parameter β, using a series of mock peculiar velocity surveys and assuming (as a proof-of-concept) a Gaussian luminosity function.

The luminosity functions of the mock galaxies were considered as the distance indicators, where we assumed the luminosity function is independent of the spatial position of the galaxies. We used the IRAS PSCz peculiar velocity field (the same data sample used in Chapter 2) to generate the mock catalogues, assuming that each mock galaxy position was coincident with one of the PSCz galaxies. Our main goals of applying ROBUST method are as follows;

1. Analyse the potential of ROBUST method with the future redshift surveys.
2. Explore the influence for the accuracy of the method if there is a high scatter in the luminosity function.
3. Compare the state of accuracy of the χ^2 hypothesis test and the ROBUST method in constraining β.

Finally, in the last chapter we discuss about the future approach of constraining β with a larger sample of galaxies than the PSCz galaxies, but nonetheless have the mocks mimicking the PSCz spatial distribution (or indeed any other desired spatial distribution function. In this case we propose to use the Probability Integral Transform (PIT) to generate the above sample.

Chapter 1

Introduction

The Big bang not only created the Universe but also creates numerous mysteries which make Cosmology a very challenging field of scientific research. In the early decades of the 20th Century Edwin Hubble's observations revealed the mysterious expansion of the Universe and Albert Einstein's General Theory of Relativity provided the theoretical framework to unravel that mystery. The discovery of the cosmic microwave background radiation (CMBR) provided strong evidence in support of the Big Bang model and its analysis has ultimately led to the standard *concordance* cosmological model, also known as the ΛCDM model. We dedicated this chapter to give the basic theoretical aspects in Cosmology, including the concepts we use in this thesis work.

1.1 Hubble's Law

Edwin Hubble discovered that the Universe is expanding [Hubble, 1929], and this discovery opened a new era in modern cosmology. Analysis of the line spectra of galaxies revealed a shift of the standard lines toward the red end for very distant galaxies. Furthermore, the relative shift in wavelength ($\Delta\lambda/\lambda$) appeared to be proportional to the distance of the galaxy. This implies that the recession velocity (cz) of a galaxy, due to the expansion of the Universe, is proportional to its distance (d), the proper distance that the light had traveled from the galaxy in the rest frame of the observer (Figure 1.1). This is called *Hubble's law*;

$$cz = H_0\, d, \tag{1.1}$$

where c is the velocity of light and z is the corresponding redshift and H_0 is the Hubble constant, which tells about the present expansion rate of the Universe. The subscript '0' represents the present time, and in general H is a function of time [i.e. $H = H(t)$]. The first estimate of H_0 was published by Hubble in 1936, where he used the luminosity of Cepheid variable stars, inferred from their Period-luminosity relation [Hubble, 1929] to obtain a value of $H_0 \approx 500\,\mathrm{km\,s^{-1}\,Mpc^{-1}}$. In 1958, however, Sandage emphasized some errors incorporated in Hubble's calibrations [Adler et al., 1965]. Over the next few decades numerous studies were carried out searching a promising value for H_0. Freedman et al. [2001] suggested that the best-fit value should be $H_0 = 72\pm 8$ km s^{-1} publishing their final results of the Hubble Space telescope (HST) Key Project to measure the Hubble constant. Riess et al. [2009] carried out a study as a redetermination of the Hubble constant, using the observations of 240 Cepheid variables obtained from the Near Infrared Camera and Multi-Object Spectrometer (NICMOS) Camera 2 through the F160W filter on the Hubble Space Telescope (HST). They obtained $\mathrm{H_0} = 74.2\pm 3.6$ km s^{-1} Mpc^{-1}. Most of the studies refer these values as their prior for the Hubble constant (see for example Sekiguchi et al. [2009]; Reid et al. [2010]). However it remains common for studies of galaxy surveys (Kovač et al. [2010]; Tonry et al. [2003]; Rauzy and Hendry [2000]) to set the present-day value as $H_0 = 100h$ km s^{-1} Mpc $^{-1}$, where h is a dimensionless parameter. In the case of measuring distances with km s^{-1}, the uncertainty of h can be neglected as the Hubble parameter becomes $H_0 = 1$. The inverse of the Hubble constant is called the *Hubble time*;

$$t_H \equiv \frac{1}{H_0} = 9.78 \times 10^9 h^{-1}\, yr = 3.09 \times 10^{17} h^{-1}\, s. \tag{1.2}$$

The Hubble distance D_H can be estimated by considering the multiplication of speed of light (c) and the Hubble time, (t_H) as follows;

$$D_H \equiv c\, t_H \equiv \frac{c}{H_0} = 3000\, h^{-1}\,\mathrm{Mpc}. \tag{1.3}$$

There are some specific conditions which have to be considered in the case of apply-

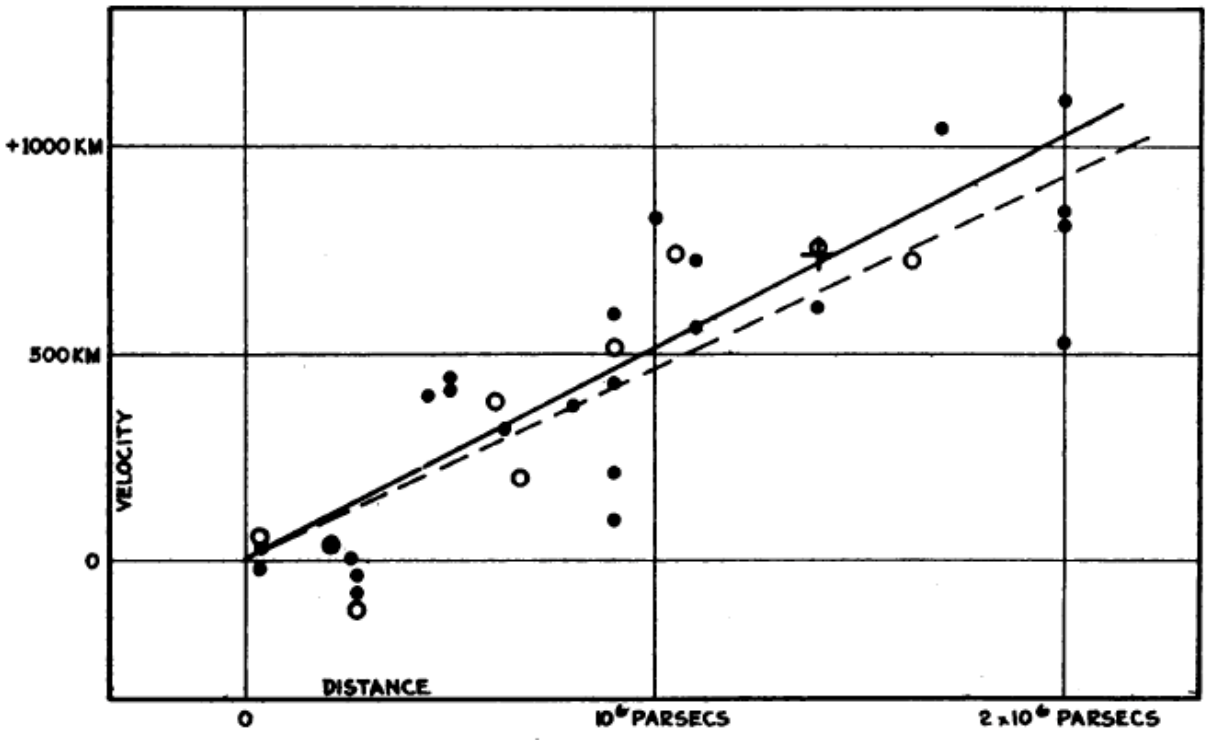

Figure 1.1: The original Hubble diagram constructed by Edwin Hubble to illustrate the expansion of the Universe. This diagram shows the proportionality between the recession velocity with the radial distance of galaxies. Figure 1, Hubble [1929].

ing the Hubble law for the nearby Universe, because the cosmological principle (i.e. homogeneous and isotropic universe) is invalid for the nearby galaxies. To consider these conditions further we need to develop the appropriate mathematical framework to describe space-time. When we discuss a Universe which is isotropic and homogeneous we work with a description of space-time discovered by Alexander Friedmann with Georges Lemaître, and again by Howard Percy Robertson as a collaboration with Arthur Geoffrey Walker [Robertson, 1935]. This is an exact solution of the Einstein field equations of the general relativity. As an honour of these four scientists, the space-time is named as the Friedmann- Lemaître- Robertson- Walker space-time.

1.2 The Friedmann equation

The Friedmann- Lemaître- Robertson-Walker space-time can be expressed in spherical polar coordinates (r, θ, ϕ);

$$ds^2 = c^2\,dt^2 - a(t)^2[\frac{d\,r^2}{1-kr^2} + r^2(d\theta^2 + \sin^2\theta\,d\phi^2)], \tag{1.4}$$

where a(t) is the scale factor and k is the space curvature constant, c is the velocity of light and r, θ and ϕ are the co-moving spatial coordinates. Here, ds^2 is the space-time interval of the FLRW metric. The Einstein's equation is given by

$$R^{\mu}_{\nu} - \frac{1}{2}\, g^{\mu}_{\nu}\, R = \frac{8\pi\, G}{c^2}\, T^{\mu}_{\nu}, \tag{1.5}$$

where T^{μ}_{ν} is the energy-momentum tensor, R^{μ}_{ν} is the Ricci tensor and G is the gravitational constant. By assuming that the Universe is a perfect fluid, the energy-momentum tensor can be expressed as;

$$T^{\mu}_{\nu} = (-\rho\, c^2, p, p, p), \tag{1.6}$$

where ρ is the mass density and p is the pressure. A dynamical solution for the scale factor $a(t)$ can be obtained from the time-time solution of Einstein's equation and considering the mass-energy content of the Universe as a perfect fluid.

$$\frac{\ddot{a}}{a} = -\frac{4}{3}\pi\, G\, (\rho + \frac{3P}{c^2}) + \frac{\Lambda\, c^2}{3}. \tag{1.7}$$

$$(\frac{\dot{a}}{a})^2 = \frac{8\,\pi\, G}{3}\rho + \frac{\Lambda\, c^2}{3} - \frac{k\, c^2}{a^2}, \tag{1.8}$$

where Λ is the cosmological constant originally introduced by Einstein to allow a static solution for $a(t)$. These expressions are called the Friedmann equations which describe the expansion of a homogeneous and isotropic Universe. Hubble's law can be explained using the Friedmann equation. The recession velocity $\mathbf{v}$ (i.e. cz) can be given as;

$$\mathbf{v} = \frac{d\mathbf{R}}{dt}, \tag{1.9}$$

$\mathbf{v}$ and $\mathbf{R}$ have the same direction and therefore;

$$\mathbf{v} = \frac{\left|\dot{\mathbf{R}}\right|}{|\mathbf{R}|}\mathbf{R} = \frac{\dot{a}}{a}\mathbf{R}. \tag{1.10}$$

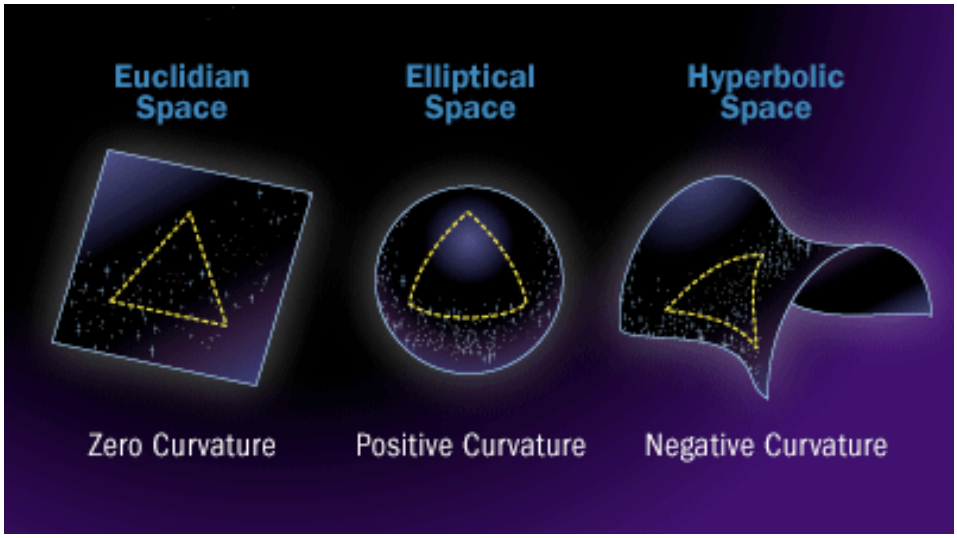

Figure 1.2: Models of the Universe. Here the zero curvature ($k = 0$) gives the flat Universe and the positive ($k = +1$) and negative ($k = -1$) curvatures are giving the closed and open models of the Universe.

The expression $\mathbf{R} = a(t)\,\boldsymbol{x}$ implies that the comoving position $\vec{\boldsymbol{x}}$ is a constant, by definition. Consequently, the Hubble's law $\mathbf{v} = H\,\mathbf{R}$ indicates that the Hubble parameter $H = H(t)$ should be identified as;

$$H = \frac{\dot{a}}{a}. \tag{1.11}$$

Then the Friedmann equation can be modified in terms of the Hubble parameter as follows,

$$H^2 = \frac{8\,\pi\,G}{3}\rho - \frac{kc^2}{a^2}. \tag{1.12}$$

Another important property of Friedmann equation is the behaviour of k, the *curvature of space-time*, which holds three principal values -1, 0 and 1. The curvature for the model of the Universe with $\Lambda = 0$, can be defined as open, flat or closed according to these values. These three models are shown in the figure 1.2 and summarized in Table 1.1.

Table 1.1: Models of the Universe, $\Lambda = 0$

Curvature	Geometry	Model	fate of the Universe
$k = -1$	Hyperbolic	Open	Expands forever
$k = 0$	Euclidian	Flat	Expands forever
$k = +1$	Elliptical	Closed	Big crunch

When $k = 0$, the Universe is considered to be flat and under this condition, the equation (1.12) can be modified as follow;

$$H^2 = \frac{8\,\pi\,G}{3}\,\rho. \tag{1.13}$$

Then ρ can be interpreted from the above equation by defining the critical density (i.e. ρ_c);

$$\rho_c = \frac{3\,H^2}{8\,\pi\,G}. \tag{1.14}$$

The critical density conveys information about the ultimate expansion or recollapse of the Universe (i.e. fate of the Universe). The dimensionless matter density parameter (Ω_m) can be expressed as;

$$\Omega_m = \frac{\rho}{\rho_c} = \frac{8\,\pi\,G\,\rho}{3\,H^2}. \tag{1.15}$$

The dimensionless energy density parameter Ω_Λ is,

$$\Omega_\Lambda = \frac{\Lambda\,c^2}{3\,H^2} \tag{1.16}$$

A third density parameter (Ω_k) measures the curvature of space, and can be defined by the following relationship,

$$\Omega_m + \Omega_\Lambda + \Omega_k = 1. \tag{1.17}$$

When the Universe is homogeneous, isotropic and matter-dominated, these parameters completely determine the geometry of the Universe [Hogg, 1999].

Talking about the formation of the Universe is also important as well as the models of the Universe. In the next section we discuss about the formation of structures in the Universe. In a situation where an object's self-gravity exceeds opposing forces such as internal gas pressure or material rigidity, the object collapses. For a gas,

gravitational instability sets in when the mass is greater than a certain critical value known as the Jean's mass (i.e. the critical mass a volume of space must contain before it will collapse under the force of its own gravity). In the early universe, instabilities were large enough to produce galaxies and clusters of galaxies.

1.3 Gravitational Instability

The Gravitational Instability is a universally accepted concept, which describes the formation of structures in the Universe. In the early Universe, there are small irregularities in the distribution of matter [Liddle, 2003]. These regions with more matter will make gravitational attraction on their neighbouring regions, bringing materials together, which cause more irregularities on density. When explaining the distribution and motion of the matter in the Universe, information about the gravity is very important because of the above phenomenon. The theory of gravitational instability can be discussed using the equation of mass continuity (1.18), equation of motion (1.19) and the Poisson equation for a fluid (1.20);

$$\frac{\partial \rho}{\partial t} + \nabla_r.(\rho \mathbf{V}) = 0 \tag{1.18}$$

$$\frac{\partial \mathbf{V}}{\partial t} + (\mathbf{V} \cdot \nabla_r)\mathbf{V} + \nabla_r \phi = 0 \tag{1.19}$$

$$\nabla_r^2 \phi = 4\pi G \rho. \tag{1.20}$$

The $\rho = \rho(\mathbf{r}, t)$ of the above equations defines a scalar mass density field. The velocity field is given by $\mathbf{V} = \mathbf{V}(\mathbf{r}, t)$. $\phi = \phi(\mathbf{r}, t)$ denotes the gravitational potential and ∇_r represents the gradient operator in proper coordinates.

The dimensionless density contrast can be defined as follows;

$$\delta(\mathbf{r}, t) = \frac{\rho(\mathbf{r}, t) - \bar{\rho}\,(t)}{\bar{\rho}(t)}, \tag{1.21}$$

where $\bar{\rho}(t)$ is the mean mass density .

Consider the linear terms of δ and $\mathbf{V}$ from the expanded expressions of the equations (1.18) and (1.19), then converting the gradient operator ∇_r to co-moving coordinates (coordinates fixed with respect to the overall Hubble flow of the Universe) and subtracting the zeroth order solution for the background solution;

$$\frac{\partial \delta}{\partial t} + \frac{1}{a}\nabla \mathbf{V} = 0, \tag{1.22}$$

$$\frac{\partial \mathbf{V}}{\partial t} + \frac{\dot{a}a}{\mathbf{V}} + \frac{1}{a}\nabla \phi = 0, \tag{1.23}$$

where $a = a(t)$ is the scalar factor. The substitution of the time derivative of equation (1.22) and the divergence of the equation (1.23) into the equation (1.20) yields;

$$\frac{\partial^2 \delta}{\partial t^2} + 2\frac{\dot{a}}{a}\frac{\partial \delta}{\partial t} = 4\pi G\bar{\rho}\delta. \tag{1.24}$$

The equation (1.24) is a second-order partial differential equation, which depends on time only. Therefore, a solution with the separate terms for spatial and time dependence can be obtained;

$$\delta = A(\mathbf{r})D_1(t) + B(\mathbf{r})D_2(t), \tag{1.25}$$

where D_1(t) and D_2(t) are the growing and decaying modes, respectively. D_1 increases with the increasing of a, the scale factor, whereas D_2 decreases with a.

For cosmological models with $\Omega_\Lambda = 0$, an analytic solution for δ can be found. In the case of the Einstein de Sitter model, with $\Omega_m = 0$ and $\Lambda = 0$, $a(t) \propto t^{2/3}$ and $\bar{\rho} \propto a(t)^{-3}$. Hence, the equation (1.24) becomes;

$$\frac{\partial^2 \delta}{\partial t^2} + \frac{4}{3t}\frac{\partial \delta}{\partial t} = \frac{2}{3t^2}\delta. \tag{1.26}$$

This has an analytic solution;

$$\delta(\mathbf{r}, t) = A(\mathbf{r})t^{\frac{2}{3}} + B(\mathbf{r})t^{-1}. \tag{1.27}$$

For more general cosmological models, the solution for δ depends on the value of Ω_m and Ω_Λ. For $\Omega_m < 1$, the expansion of the universe dominates the gravitational attraction of the matter. At late times, the second term of the analytic solution becomes negligible, and the equation (1.22) reduces to;

$$\nabla.\mathbf{V} = -a\,\delta\,\frac{\dot{D}_1}{D_1} = -a_0\,H_0\,f\delta, \tag{1.28}$$

where the growth factor, f can be written as;

$$f = \frac{1}{H_0 D_1}\frac{dD_1}{dt} = \frac{d\,\log\,D_1}{d\,\log\,a}. \tag{1.29}$$

D_1 is a function of Ω_m and Ω_Λ. Therefore, f is also a function of Ω_m and Ω_Λ. Lahav et al. [1991] provide an approximation to f as shown below;

$$f(\Omega_m, \Omega_\Lambda) = \Omega_m^{0.6} + \frac{\Omega_\Lambda}{70}(1 + \frac{1}{2}\Omega_m). \tag{1.30}$$

The influence of Ω_Λ on dynamics at low redshift is negligible [Lahav et al., 1991]. Hence, the equation (1.30) becomes;

$$f = \Omega_m^{0.6}. \tag{1.31}$$

Then the equation (1.28) can be modified as;

$$\nabla.\mathbf{V} = -a_0 H_0 \Omega_m^{0.6}\delta(\mathbf{r}). \tag{1.32}$$

Following the theorems of electrostatics, a solution for equation (1.32) can be obtained;

$$\mathbf{V}(\mathbf{r}) = \frac{H_0\Omega_m^{0.6}}{4\pi}\int\frac{d^3r'\delta(\mathbf{r}')(\mathbf{r}'-\mathbf{r})}{|\mathbf{r}'-\mathbf{r}|^3}, \tag{1.33}$$

where $\mathbf{r}$ is the position of galaxies, $\mathbf{r}'$ is a considered position in the space, $\mathbf{V}(\mathbf{r})$ denotes the peculiar velocity at position $\mathbf{r}$ and $\delta(\mathbf{r}')$ represents the galaxy number density at position $\mathbf{r}'$. This prediction has been widely used in studies of peculiar velocity fields.

1.4 Linear bias model

Even though the Universe mostly consists of dark matter (we discuss about dark matter in detail in Section 1.6), nobody has been observed this directly. Only the luminous matter, like galaxies can be observed. Therefore, a relationship between the density field of galaxies (i.e. luminous matter) and dark matter is very important. The most simplest argument is that the distribution of galaxies also contain the information about the dark matter distribution;

$$\delta_g(\mathbf{r}) = \delta(\mathbf{r}). \tag{1.34}$$

In relatively larger scales the distribution of galaxies is very uneven and this assumption is no longer valid. Kaiser [1984], proposed a method to address this behaviour, where he suggested that the galaxies form only at the high-density peaks of the mass density field. The galaxy clusters are then said to be biased with respect to the mass distribution. Bardeen et al. [1986], Peacock and Heavens [1985] and Davis and Djorgovski [1985] also proposed a similar effect between the galaxies and the dark matter allowing to use the peaks biasing model to obtain even more specific models. This model is called the *linear bias model*, which relates galaxy distribution and dark matter distribution;

$$\delta_{galaxies}(\mathbf{r}) = b\ \delta_{darkmatter}(\mathbf{r}), \tag{1.35}$$

where b is the *biasing parameter*, which is related to the threshold described above. For $b > 1$, this model is deviated as $\delta_{galaxies}$ and $\delta_{darkmatter}$ are bounded under -1, and therefore a modified version of the above equation has been considered;

$$1 + \delta_{galaxies}(\mathbf{r}) = [1 + \delta_{dark\ matter}(\mathbf{r})]^b. \tag{1.36}$$

A local relation between the galaxy and mass density fields provided a more general and less complex assumption [Weinberg, 1995];

$$\delta_g(r, R_s) = F[\delta(r, R_s)], \tag{1.37}$$

where F is an arbitrary function and R_s is some scale. The Taylor expansion for small fluctuation amplitude can be given by;

$$\delta_g = a + b_1\delta + \frac{b_2\delta^2}{2} + \frac{b_3\delta^3}{6} + \cdots \tag{1.38}$$

$$b_1 = F'(0),\ b_2 = F''(0),\ b_3 = F'''(0),\ \cdots \tag{1.39}$$

The constant a is fixed at any order by the requirement $\langle\delta_g\rangle = 0$. The linear bias model emerges as the first order expansion of this local model, with $b = b_1$ (i.e. Equation 1.35), suggesting that linear bias may often be an adequate description on scales where linear perturbation theory applies. The ratio of the fluctuations $\sigma(R_s)$ in the galaxies and dark matter is independent of scale R_s when the scales larger than 5 h^{-1} Mpc. This doesn't hold for non-biasing models, in which galaxy formation is influenced by events in far away distances (Babul and White [1991]; Bower et al. [1993]). Under these schemes, the ratio between the amplitude of dark matter and galaxy fluctuation become a function of scale.

The suggestion to relate $\delta_{galaxies}$ with $\delta_{dark\ matter}$ holds only in the mean density $\bar{\rho}$; at any given point in space there can be seen fluctuations around this mean density in the relation between the densities. A complete model of biasing should be able to describe these fluctuations. In the region that the linear bias model holds, the equation (1.28) is unable to restrict the quantity f *via* comparing the peculiar velocities and gravity. In this situation, the expression given below can be applied;

$$\beta = \frac{f(\Omega_m, \Omega_\Lambda)}{b}. \tag{1.40}$$

According to the prediction of $f(\Omega_m, \Omega_\Lambda)$, we can write $f = \Omega_m^{0.6}$ (i.e. equation 1.31). Therefore equation 1.40 can be rearranged as follows;

$$\beta = \frac{\Omega_m^{0.6}}{b}, \tag{1.41}$$

where β is known as the *redshift distortion parameter*.

Equation 1.32 can be rearranged with the substitution of β;

$$\nabla.\mathbf{V} = -a_0 \; H_0 \; \beta\delta_g \; (\mathbf{r}). \tag{1.42}$$

By applying the techniques of electrostatics, a relationship between peculiar velocity field and β, can be obtained;

$$\mathbf{V}(\mathbf{r}) = \frac{H_0\beta}{4\pi} \int \frac{\delta(\mathbf{r}^{'})(\mathbf{r}^{'} - \mathbf{r})}{|\mathbf{r}^{'} - \mathbf{r}|^3} d\,^3r^{'}. \tag{1.43}$$

Obtaining a better estimate of β could significantly improve the accuracy of reconstructed peculiar velocity fields, which is the subject of this thesis.

1.5 Cosmic Microwave Background Radiation

The early Universe was filled with ionized matter like electrons, protons and emitted radiation. As the Universe expanded and cooled down, the reactions between electrons and protons formed neutral atoms, and then eventually stars, galaxies etc (Figure 1.3). The radiations that were generated in the early stages of the evolution of the Universe form the Cosmic Microwave Background (CMB). The CMB radiation appears to have very similar temperature in all directions, which leads it to be called isotropic. The isotropy of the CMBR provides strong support for the cosmological principle, which states that large-scale of the Universe is *homogeneous* (same density at all points at a given time) and *isotropic* (same in all directions). However, the nearby Universe is not homogeneous and isotropic as it is a complex mixture of stars, planets, galaxies, clusters and super-clusters. Therefore, the cosmological principle is not valid for the nearby Universe (Figure 1.4).

Arno Penzias and Robert Wilson of AT&T Bell Laboratories detected the CMB radiation in 1965 while trying to find the source of a mysterious background noise in their radio antenna [Penzias and Wilson, 1965]. The CMB provides most promising result to support the big bang theory, which states that the early universe was a hot, dense plasma of charged particles and photons. The CMB has been cooled by the

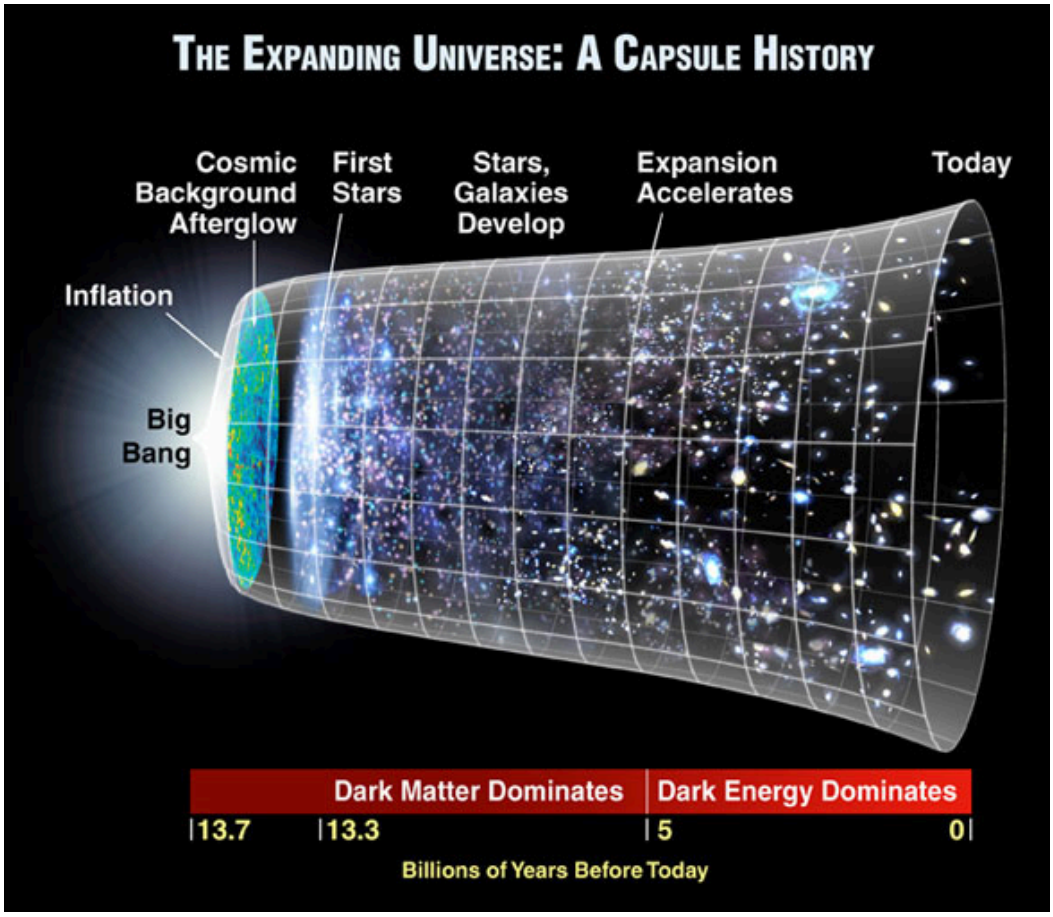

Figure 1.3: Time line of the Universe. NASA/WMAP Science Team

expansion of the universe, and it is extremely cold today-comparable to the radiation released by a body at a temperature of about 2.7 K. But at the time that the CMB was released, its temperature was nearly 3,000 K. In 1970's, the astronomers learnt about a dipole anisotropy in the CMB spatial temperature distribution (Corey and Wilkinson [1976], Fabbri et al. [1980]). In 1990, the COBE satellite (Cosmic Background Explorer) measured the spectrum of the CMB radiation and the COBE DMR experiment reported the first detection of cosmological anisotropy (apart from the previously detected dipole) in the temperature of the CMB (Smoot et al. [1992]; Bennett et al. [1992], Wright et al. [1992]). These small variations in the intensity of the CMB over the sky show how matter and energy was distributed in the early Universe. Depending on this key issue, astronomers focussed their attention on the temperature variations of the CMB with more sophisticated instruments and launched the Wilkinson Microwave Anisotropy Probe (WMAP) in 2001. The aim was to map the Cosmic Microwave Background (CMB) radiation over the entire sky in five frequency bands centered at 23 GHz (K band), 33 GHz (Ka band), 41 GHz (Q

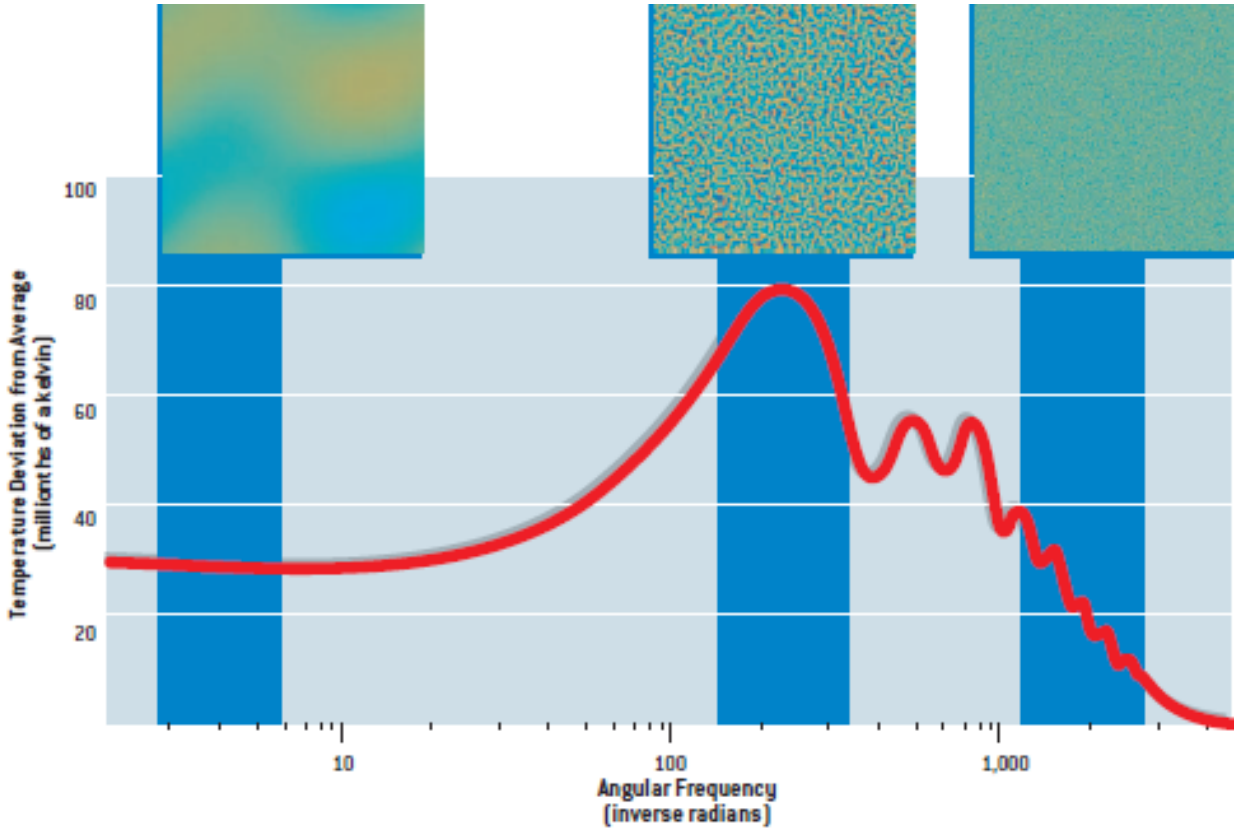

Figure 1.4: The variation of the temperature of CMBR at different scales of the Universe. The variations of lower amplitude at large scales corresponding to regions that stretch about 30 degrees across the sky (left) and at small scales corresponding to regions about a tenth of a degree across (right). But the temperature differences are quite distinct for regions about one degree across (middle). http://background.uchicago.edu / whu/Papers/HuWhi04.pdf

band), 61 GHz (V band) and 94 GHz (W band) (Bennett et al. [2003]; Jarosik et al. [2010]). It was launched in June 2001 (and still in operation) from Kennedy Space Flight Centre and began surveying the sky from its orbit around the Earth-Sun L2 point in August 2001 and recently published the seven-year observations (Jarosik et al. [2010]; Komatsu et al. [2010]). Results from the one-year, three-year and five-year results are summarized in , Bennett et al. [2003]; Jarosik et al. [2007] and Hinshaw et al. [2009], respectively.

The results from WMAP reveal that the CMB temperature variations follow a distinctive pattern predicted by cosmological theory: the hot and cold spots in the radiation fall into characteristic sizes. The origin of the dipole anisotropy is now widely accepted as a Doppler effect arising from the motion of the Sun with respect to the CMB rest frame. Measurements by the COBE, and WMAP, imply a Solar System velocity with respect to the CMB of 369.0 $\pm$ 0.9 km s^{-1} [Hinshaw et al., 2009]. Further the studies imply that the Local Group has a net peculiar velocity in excess of 600 km s^{-1} with respect to the rest frame of the CMB (Figure 1.5), in the direction $(l, b) \sim (276^o, 30^o)$ (Maller et al. [2003]; Erdoğdu et al. [2006]).

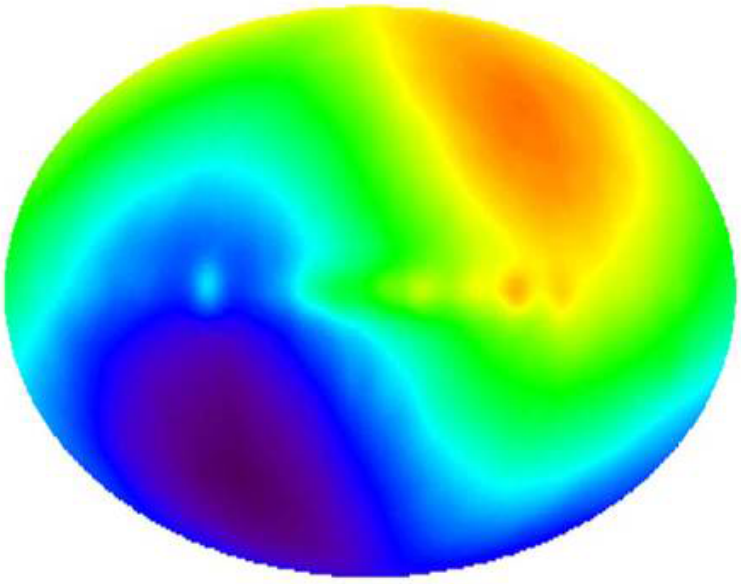

Figure 1.5: The CMB dipole. Radiation in the Earth's direction of motion appears blueshifted and hence hotter, while radiation on the opposite side of the sky is redshifted and colder. The map indicates that the Local Group moves at about 600 km s^{-1} relative to the CMB frame.

Astronomers plot the magnitude of the temperature variations against the sizes of

the hot and cold spots in a graph called a *power spectrum*. The first acoustic peak of the anisotropy power spectrum has been detected from COBE data (Mauskopf et al. [2000]; Miller et al. [1999]) and the power spectrum has been modified with the each data release of WMAP (Bennett et al. [2003]; Hinshaw et al. [2009]). The power spectrum drawn for the seven-year WMAP data [Komatsu et al., 2010] is shown in the figure 1.6. The temperature-polarization power spectra, drawn from CMB data, offer unique tests of the *standard cosmological model* providing evidence that the universe is close to spatially flat and indicate the existence of dark energy [Hu et al., 1999], the model that describes the evolution of the Universe. In this model the Universe is spatially flat, homogeneous and isotropic on large scales, composed of radiation, ordinary matter (electrons, protons, neutrons and neutrinos), non-baryonic cold dark matter, and dark energy.

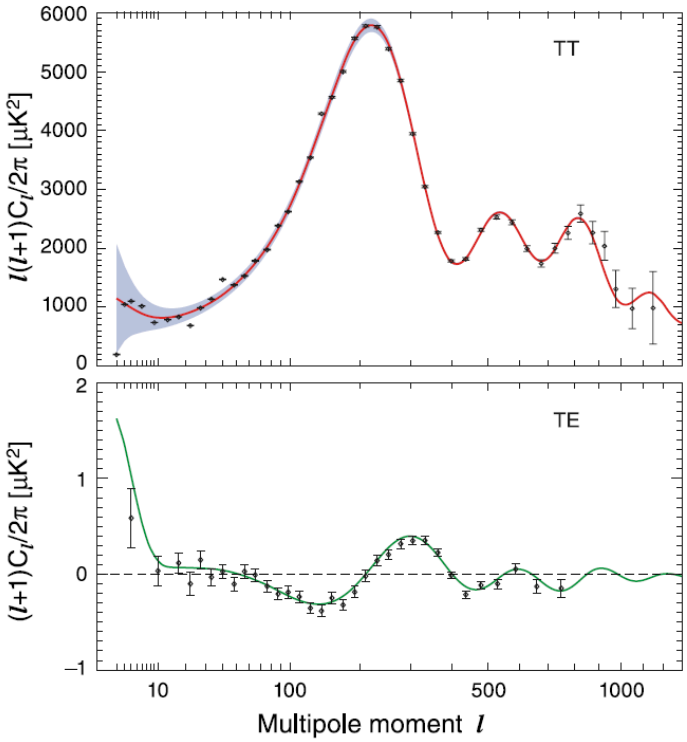

Figure 1.6: The temperature (TT) and temperature-polarization(TE) power spectra for the seven-year WMAP data set. The solid lines show the predicted spectrum for the best-fit flat ΛCDM model. Figure 9, Komatsu et al. [2010]

1.6 Dark matter and dark energy

Based on the latest observations, we can only observe 4 % of the total energy density which is called normal matter made up of stars, planets, galaxies and super clusters. About 22 % is assumed to be dark matter and the remaining 74 % is considered to be dark energy. In 1932, Oort found evidences for dark matter in the Milky Way galaxy and then in 1933 Fritz Zwicky inferred large density of matter within clusters of galaxies [Liddle, 2003]. These evidences implied that dark matter may explain the rotational speeds of galaxies, orbital velocities of galaxies in clusters, gravitational lensing of background objects of galaxy clusters, and the temperature distribution of hot gas in galaxies and clusters of galaxies. Figure 1.7 is an illustration of the content in the Universe, obtained from the WMAP data. The constraints on Ω_b (the baryonic matter) from nucleosynthesis indicate that the considerable amount of dark matter in the Universe is non-baryonic. There are three types of non-baryonic dark matter, namely hot dark matter (HDM), warm dark matter (WDM) and cold dark matter (CDM).

- HDM - Particles that decouple when ultra relativistic (i.e. move with a velocity $v \cong c$), and they have a number density roughly equal to that of photons.
- WDM - The particle decouples sufficiently early, which means relativistically.
- CDM - The particles decouple when they are nonrelativistic (i.e. $v << c$).

The cosmic microwave background (CMB) contains information about the dark components present in the early universe, specifically the ratio of non-relativistic or cold dark matter (CDM) to relativistic species such as the neutrino background radiation (NBR) and the ratio of the baryonic dark matter to the CMB itself [Hu et al., 1999]. The expansion is currently accelerating under the influence of the dark energy giving a non-zero cosmological parameter Λ [Perlmutter et al., 1999]. Komatsu et al. [2010] use seven-year WMAP data and obtained the matter density $\Omega_m h^2 = 0.1334^{+0.0056}_{-0.0055}$, dark matter density, $\Omega_c = 0.222 \pm 0.026$ and dark energy density, $\Omega_\Lambda = 0.734 \pm 0.029$.

The knowledge of dark matter is critical for explaining the structure formation and galaxy evolution. The peculiar velocities of galaxies are affected by the gravitational pull of the dark matter, and therefore the study of peculiar velocity field is very important in understanding the behaviour of dark matter.

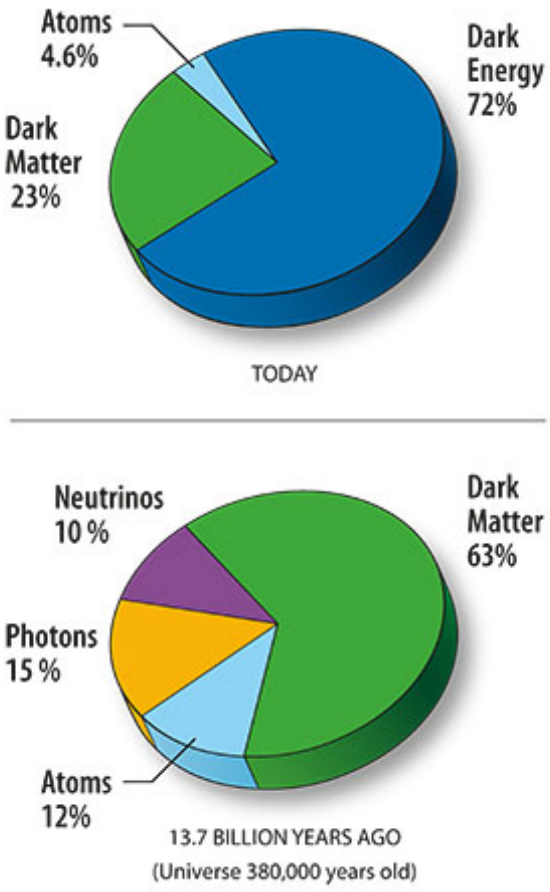

Figure 1.7: The content of the Universe. NASA / WMAP Science Team

1.7 Peculiar velocity field

Some regions of the Universe have more matter density ($> \rho_c$) compared to the other regions. As being carried along by the cosmic expansion with a recession velocity cz, galaxies are moving *through* the space towards more denser regions, due to their gravitational attraction. Further, these special motions are known as the *galaxy peculiar motions*. Hubble's law is unable to describe these motions as this law breaks down for nearby galaxies. Therefore, a modified expression of Hubble's law is necessary to describe peculiar velocities.

For a given galaxy, it is difficult to measure the recession velocity cz and the peculiar velocity $u(r)$, separately. However, the cosmological principle emphasis the typical size of the peculiar velocity would not depend on the position of the galaxy in the Universe [Liddle, 2003]. Consequently, the peculiar velocities are independent of the distance, and the Hubble velocity is proportional to distance (i.e.$H_0 r$).

Then, the peculiar velocity $u(r)$ can be expressed in the scalar form (1.44) and vector form (1.45) as,

$$u(r) = cz - H_0\ r. \tag{1.44}$$

$$u(r) = \hat{\mathbf{r}} \cdot [\mathbf{v}(\mathbf{r}) - \mathbf{v}(O)]\,, \tag{1.45}$$

where $\hat{\mathbf{r}}$ is the unit vector towards the considered galaxy, $\mathbf{v}(\mathbf{r})$ is the peculiar velocity at position $\mathbf{r}$, and $\mathbf{v}(O)$ is the peculiar velocity of the observer (i.e. Local Group velocity- v_{pec} = 600 kms^{-1}, CMB dipole). Then the modified expression of the Hubble's law can be obtained by rearranging the terms in the equation (1.44), which explains peculiar velocities;

$$cz = H_0\ r + u(r), \tag{1.46}$$

$$cz = H_0\ r + \hat{\mathbf{r}} \cdot [\mathbf{v}(\mathbf{r}) - \mathbf{v}(O)]\,. \tag{1.47}$$

The strength and the direction of peculiar velocities are related to the matter distribution around them. Therefore, the study of galaxy *peculiar motion* is very useful in understanding the distribution of dark matter in the Universe. Astronomers measure redshift cz from the redshift surveys. However, these surveys are unable to separate the peculiar velocity component from cz. As discussed earlier, peculiar velocities are independent of the distance, and therefore, in order to study the peculiar velocity field, *redshift-independent* distance measurements are critical. Hence, the peculiar velocity studies are based on the data sets obtained from the redshift and redshift-independent distance measurements. All these redshift surveys are only able to measure the *radial component* of the peculiar velocity. Astronomers use the expression of distance modulus to represent the distance measurements, which is the

subject of the next section.

1.8 Distance modulus

The *distance modulus* basically depends on magnitude, which can be considered as the *apparent magnitude* and the *absolute magnitude*. The apparent magnitude, m, is the brightness of the object (i.e. galaxies, stars, planets, clusters) as seen by the observer on the earth. Further, the apparent magnitude depends on two factors, the luminosity of the object and the distance of the object from the Earth. The absolute magnitude, M only depends on the luminosity of the object, which can be considered as an intrinsic property of the object. Moreover, the absolute magnitude is defined as the apparent magnitude of an object if it were at a distance of 10 parsecs from the Earth. A galaxy's luminosity, L, is the total amount of energy radiated per unit time. The absolute magnitude, M, of a galaxy is related to its luminosity in the same way as apparent magnitude, m, is related to flux F. A relation for the difference of absolute magnitudes M_1 and M_2 of two galaxies can be obtained by comparing the ratio of their luminosities;

$$M_1 - M_2 = -2.5 \log \frac{L_1}{L_2}. \tag{1.48}$$

Distance Modulus, μ, is the difference between apparent (m) and absolute magnitudes (M). A relationship between M and m, and distance, d, can be expressed using μ. The inverse square law tells that the flux is inversely proportional to the square of d. Consider a galaxy at distance d (parsecs), with observed flux F_m. Then its flux F_M at 10 parsecs would be given by following the inverse square law;

$$\frac{F_M}{F_m} = \frac{d^2}{10^2}. \tag{1.49}$$

This equation can be combined with equation (1.48), which gives the *distance modulus equation*;

$$\mu \equiv m - M = 5 \log d - 5. \tag{1.50}$$

We can obtain the *luminosity-distance relation* through the equation (1.50);

$$m = M + 5 \log d - 5. \tag{1.51}$$

If the absolute and apparent magnitudes of the galaxy are known, then the distance to the galaxy can be calculated using the distance modulus;

$$d = 10^{0.2(\mu+5)} \tag{1.52}$$

If we consider the distance in units of Mpc, the equation (1.50) has to be rearranged as follows;

$$\mu \equiv m - M = 5 \log d + 25. \tag{1.53}$$

The required measurements for the distances can be estimated using redshift, which is the theme of the next section.

1.9 Redshift

Relative motion of a light source and an observer is subjected to the *Doppler Effect*. Further, the wavelength of light increases as it passes through the expanding universe between the points of emission and the observation, resulting a shift towards the red end of the electromagnetic spectrum. The increment of the wavelength is proportional to the expansion of the universe. This phenomenon is called the *cosmological redshift*. Almost all the galaxies are receding from the earth [Liddle, 2003], and the cosmological redshift explains this motion clearly, as;

$$z \equiv \frac{\nu_e - \nu_o}{\nu_o} = \frac{\lambda_o - \lambda_e}{\lambda_e}, \tag{1.54}$$

where ν_e and λ_e are the emitted frequency and wavelength, and ν_o and λ_o are the observed frequency and wavelength, respectively. In special relativity, redshift is related to the radial velocity v by;

$$1 + z = \sqrt{\frac{1 + v/c}{1 - v/c}}. \tag{1.55}$$

There is a difference between the measured redshift z_{obs}, and the cosmological redshift, z_{cos}, of an object. This deviation occurs due to the influence of the radial peculiar velocity of the object (Section 1.7). The relation between the peculiar velocity and the redshift difference can be expressed as [Hogg, 1999],

$$v_{pec} = c\,\frac{(z_{obs} - z_{cos})}{(1+z)}. \tag{1.56}$$

Applying the binomial expansion to the equation (1.55), the following expression can be obtained for small redshifts (in the case of small v/c);

$$z \approx \frac{v}{c}. \tag{1.57}$$

For small distance d, the recession velocity is linearly proportional to the distance;

$$v = H_0\, d = cz. \tag{1.58}$$

Therefore,

$$z \approx \frac{v}{c} = \frac{d}{D_H}. \tag{1.59}$$

Many galaxy redshift surveys use the non-relativistic approximation $v = cz$, when presenting redshifts as radial velocities.

1.10 Redshift-independent distance indicators

Accurate measurement of distance is critical in predicting peculiar velocities. Moreover, the uncertainty of the distance of a galaxy is highly influential on the accuracy of the galaxy peculiar velocity. *Standard candle distance indicators* are the most prominent methods of obtaining the distances of galaxies with high level of accuracy. An astrophysical object, such as a supernova or variable star with known absolute magnitude, is referred to as a standard candle. This absolute magnitude is assumed to be a constant for a corresponding standard candle. If an object can be identified as a standard candle, then the distance of the object can be obtained using the lumi-

nosity distance relationship (i.e. equation 1.51), which involves the known absolute magnitude M and the measured apparent magnitude m. A sequence of techniques has been used to estimate the distance of remote objects, the so-called *distance ladder*. Each technique in the sequence is calibrated by the previous techniques, and extends the range of measurement to greater distances.

The distance indicators in the distance ladder can be divided into two groups, the primary and secondary distance indicators. The *primary distance indicators* (PDI) measure distances calibrated from the observations taken from the Local Group or from the theoretical considerations. When we have established the distances to nearby galaxies with primary methods, we use them to calibrate the less secure secondary methods, which have to be used to find the distances to distant galaxies. The major PDI used in distance measurements are the Cepheid variable stars and RR Lyrae variable stars.

1.10.1 RR Lyrae variable stars (< 1 Mpc)

RR lyrae variable stars (RRL) are important mostly for measuring distances of the old, low-mass stars [Smith et al., 2003]. The most popular approach to estimate the RR Lyrae distances is the M_V -[Fe/H] relation and this only requires two observables, the apparent visual magnitude and the metallicity (i.e. the proportion of matter of an object made up of chemical elements other than hydrogen and helium). According to the evidences from several recent theoretical and empirical studies the RR Lyrae stars are considered to be excellent standard candles in the near-infrared spectral range [Bono, 2003].

Longmore et al. [1986] discovered that the RRL variable stars obey a *period-luminosity (P-L)* relation in the near-infrared K-band. This finding allowed to apply infrared versions of the Baade-Wesselink method to calibrate the luminosities and distances of RRL stars (Liu and Janes [1990]; Skillen et al. [1993]; Jones et al. [1996]). The first theoretical constraints on the K-band P-L relation of RRL stars are based on non-linear convective pulsation models that were presented by Bono et al. [2001]. Further,

theoretical explorations of the RRL period-mean magnitude-metallicity relations in near-infrared pass bands were carried out by Bono et al. [2003]. They found the distance modulus of the LMC cluster Reticulum, a sizable sample of RR Lyrae, to be 18.45, using the K-band Period-Luminosity-Metallicity relation for RR Lyrae stars. With the approach of the Hubble space telescope, the RRL variable stars within a region up to a distance of 1 Mpc can be considered for distance measurements.

1.10.2 Cepheid variable stars ($\leq$ 20 Mpc)

One of the significant features of Cepheids is that they are readily observable in nearby galaxies and the Local Group. Further, Cepheids play a key role in distance determinations because of the correlation between their mean absolute magnitude and the period. This *Cepheid variable period-luminosity* (P-L) relation was discovered in 1907 by Henrietta Leavitt. Sandage [1958] found that the displacement of the points in the period-luminosity diagram from the average line is correlated with the mean colour of the star, measured by the blue-visual colour index B-V. This *period-luminosity-colour* (P-L-C) relation appeared to be the most accurate way to measure distances with Cepheids.

The cosmic distance scale was usually established by defining the P-L relations for Cepheids in the Large Magellanic Cloud (LMC) and many of which have been discovered as a result of microlensing campaigns [Udalski et al., 1999]. The Cepheid P-L and P-L-C relations in the LMC were carefully analyzed by Martin and co-workers, where they obtained a distance modulus of 18.7 [Schommer et al., 1984], and roughly consistent results were obtained from several recalibrations done in the same period (Caldwell [1983] and Stothers [1983]). Schommer et al. [1984] found a distance modulus of 18.2 for *LMC* with a galactic Cepheid zero-point calibration. Sandage and Tammann obtained observations for NGC 2403 in the M81 group obtaining a distance 3.225 Mpc, and they calibrated this value using the stars of the Magellanic Clouds and the Milky Way [Rowan-Robinson, 1985].

Benedict used Wesenheit index [Madore and Freedman, 1991] with P-L relation

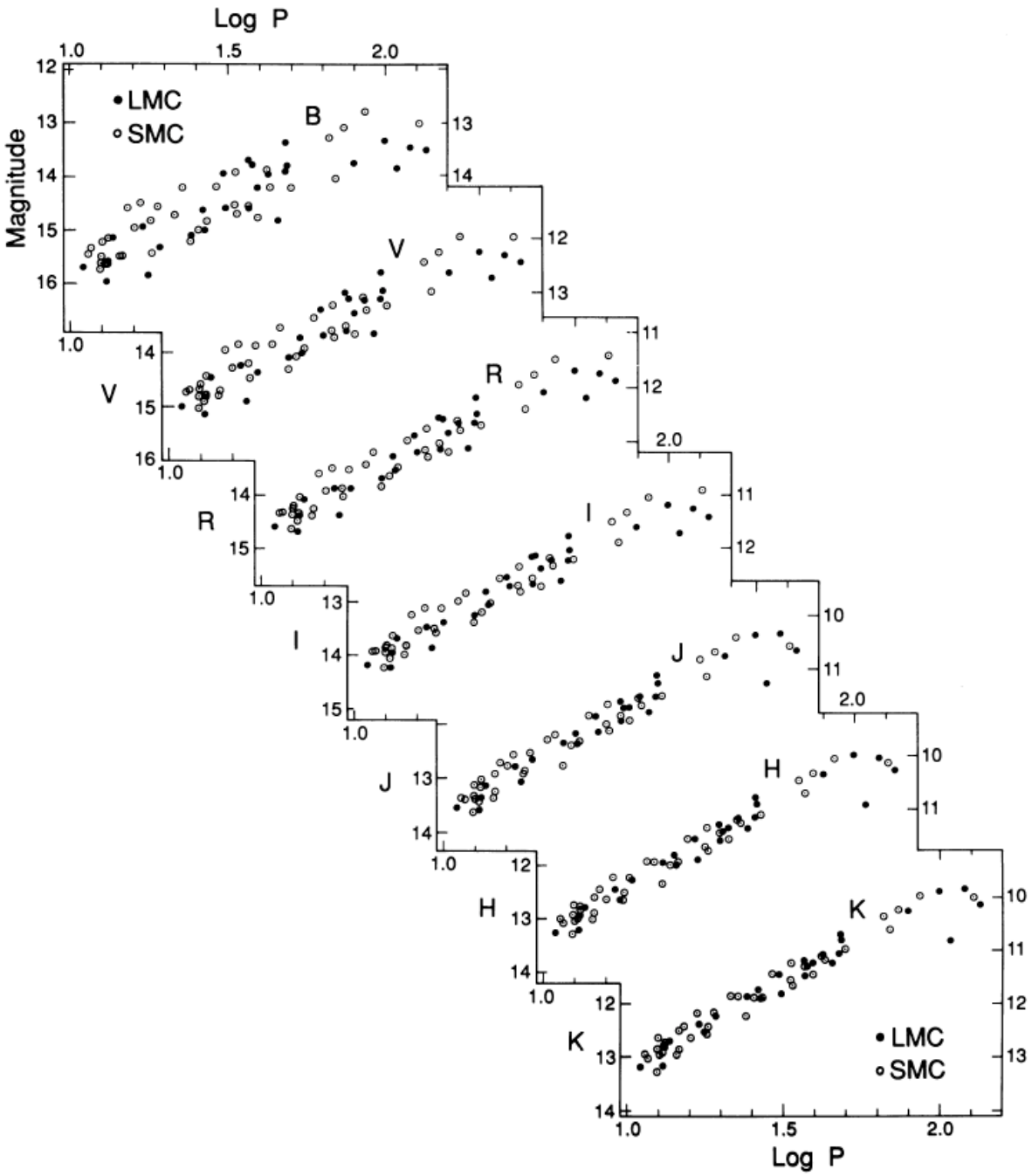

Figure 1.8: Magellenic Cloud Cepheid period-luminosity relationship at seven wavelengths, from the blue to near infrared. (Figure 4 of Madore and Freedman [1991])

[Benedict et al., 2007] and yielded a distance modulus 18.40, somewhat smaller than the value adopted by the Hubble Space Telescope Key Project (18.54) for *LMC* [Freedman et al., 2001]. An et al. [2007] derived distances to NGC 4258, in the LMC, and M33 of distance modulus = 29.28 ± 0.10, 18.34 ± 0.06, and 24.55 ± 0.28, respectively. While Cepheids are determining the distances within the Local Group, they are also involve in calibrating the secondary distance indicators which have been used to determine the Hubble constant, for example the projects like Hubble Space Telescope (HST) Key Project on the extragalactic distance scale [Freedman et al., 2001]. In the early stage of applying the primary distance indicators, Cepheids were only able to measure a distance up to 4 Mpc of the space. However, with the launch of the HST, this range can be extended to 20 Mpc.

1.11 Secondary distance indicators

Secondary distance indicators (*SDI*) are calibrated from the distances measured to nearby galaxies using primary distance indicators. Most of the *SDI* are calibrated against the distance to the LMC, M31 and M33 [Bothun, 1998]. Further, these *SDI* are used to measure the distances to more remote galaxies beyond the Local Group. This in turn extends the ability of distance measurements from 20 Mpc (boundary of PDI) to more than 1000 Mpc. Some of the reliable and well-known *SDI* are the type Ia supernovae (SNIa), the Tully Fisher (TF) relation and the luminosity functions of some astronomical objects.

1.11.1 Type Ia supernovae ($\leq$ 1000 Mpc)

SNIa are the thermonuclear explosions of degenerate white dwarfs (Figure 1.9(a))near the Chandrasekhar limit, i.e. 1.4 $M_\odot$ [Wheeler et al., 1990], or possibly mergers of white dwarfs in a binary system (Figure 1.9(b)) [Paczynski, 1985]. With their high intrinsic luminosity, SNIe have demonstrated their enormous potential as distance indicators (Riess et al. [1996]; Hamuy et al. [1995]). Astronomers believe that the SNIe can provide among the most accurate values of H_0, q_0 (the deceleration parameter), Ω_m (the matter density), and Λ (the cosmological constant, $\Lambda c^2/(3H_0^2)$).

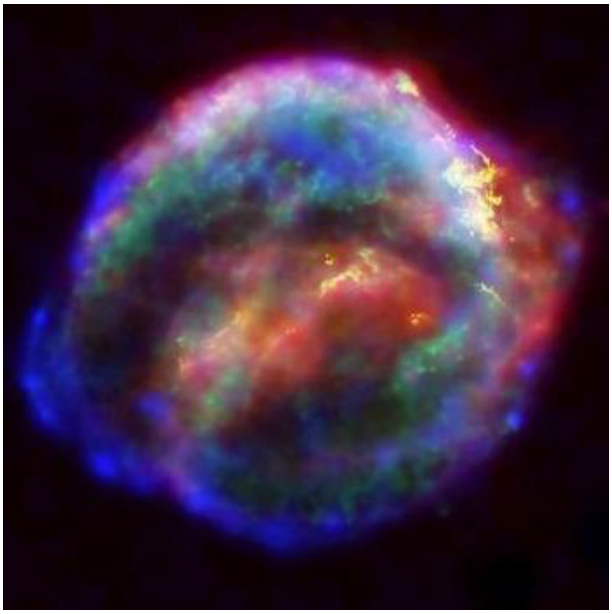

(a)

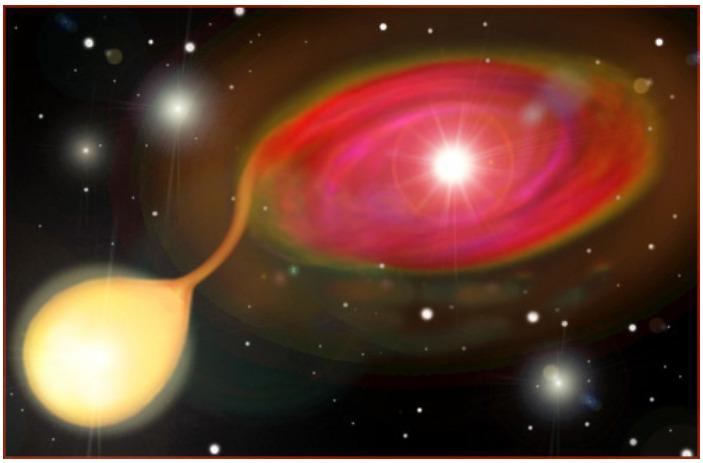

(b)

Figure 1.9: (a) A supernova occurred due to the thermonuclear explosions of degenerated white dwarfs. jumk.de/astronomie/sterne-a/novae.shtml (b) SNIe will result when a white dwarf star in a binary system accumulates enough matter from its larger companion. www.lbl.gov/.../sabl/2007/Nov /darkenergy2.html

Until the mid-1990s, the SNIa were considered in determining the cosmological distance under the assumption that they are perfect standard candles. The observed peak brightness of SNIa were considered for the measurements. It is assumed that the scatter in the peak blue luminosity is relatively small for SNIa ($\sigma_B \approx 0.4 - 0.5$ mag; Branch and Miller [1993]) and also that peculiar objects have been eliminated when taking the measurements. SNIa are not precisely standard candles, the variability in SNIa observables however introduces uncertainties that limit their effectiveness as distance indicators. The intrinsic dispersion in the peak brightness of SNIa events

can be constrained to about 0.2 magnitudes by calibrating the measured luminosity with corrections determined by the shape of the light curve [Phillips, 1993].

Phillips [1993] found that the rates of decline of the brightness of the SNIa are correlated with their peak luminosities, allowing new ways to measure the distances. The Phillips correlation between peak luminosity and $\Delta m_{15}(B)$ (a parameter that measures the total decline from B-band maximum in 15 days) has refined by Hamuy and co-workers. They used the SNIa discovered during the Calán/Tololo survey ($z \leq 0.1$) [Hamuy et al., 1995]. The scatter in the Hubble diagram of normal supernovae has reduced only to 0.17 in B band from this method.

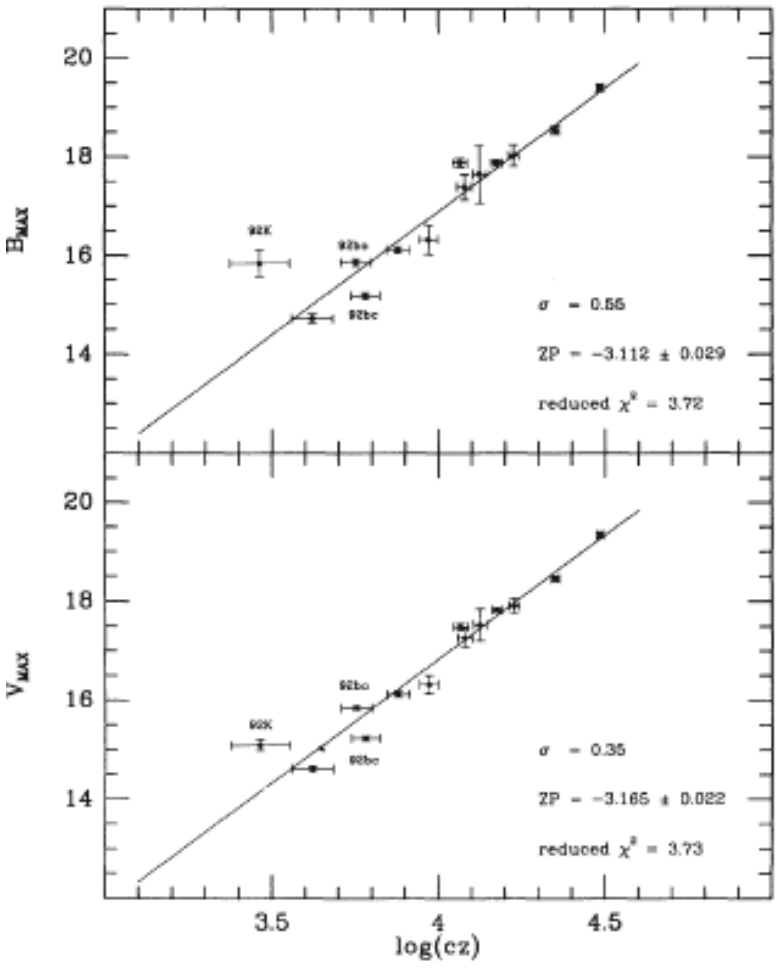

Figure 1.10: Hubble diagram of Type Ia supernovae. Figure 2, [Hamuy et al., 1995]

A correlation between the luminosity of SNIa with the shape of the overall light curve, the *Multi-colour Light-Curve Shape* (MLCS), has been discovered by Riess and co-workers [Riess et al., 1996]. Applying this method to 20 SNIa, Riess and

co-workers found out a decrease in the scatter from 0.52 mag to 0.12 mag [Riess et al., 1996]. Moreover, Jha et al. [2007] presented an updated version for MLCS, known as MLCS2k2 . They applied this method to 133 nearby SNIa, including 95 objects in the Hubble flow (cz = 2500 km s^{-1}), and found out an intrinsic dispersion of less than 7% in distance. SNIa light curves obtained by the Calan/Tololo survey indicated that it is possible to measure distances with SNIa light curves to a precision approaching 5% [Hamuy et al., 1995].

In the past few years, many nearby SNIa have been found by the industrious amateur astronomers including R. Arbour, M. Armstrong, T. Boles,T. Puckett, M. Schwartz, and others. The Lick Observatory Supernova Search (LOSS) got the credit of detecting SNIa [Filippenko, 2005] discovering 20 SNIa in 1998, 40 in 1999, 38 in 2000, 68 in 2001, 82 in 2002, and 95 in 2003. There are 250 high redshift SNIa ($z > 0.2$) and 57 low redshift SNIa ($z \leq 0.2$) in the Union data set [Kowalski et al., 2008]. The most recent Constitution data set is the largest sample, which have 147 nearby SNIa [Hicken et al., 2009]. The advantage of having a considerable amount of well-observed SNIa is calibrating the distance determinations more precisely. The near-infrared Hubble diagrams of SNIa constructed by [Krisciunas et al., 2004], using JHK light curves of nearby SNIa [Krisciunas et al., 2003], suggested that SNIa are better-behaved as standard candles in the near-infrared than in the optical.

Filippenko [2005] found that $H_0 t_0 = 0.96 \pm 0.04$ using about 200 SNIa and combining their results with large-scale structure surveys, they found a best fit for Ω_m and Ω_Λ of 0.28 and 0.72, respectively . Apart from the methods discussed above, there are a number of other methods that have been developed to model SNIa light curves. Some of them are stretch (stretch of the time axis of a fixed template to approximate different SN light curves) (Perlmutter et al. [1997]; Goldhaber et al. [2001], super stretch [Wang et al., 2006], $\Delta_m 15$ (an empirical method for fitting multicolour light curves of Type Ia supernovae) [Prieto et al., 2006], BATM (The Bayesian Adapted Template Match) [Tonry et al., 2003], CMAGIC (a color-magnitude intercept calibration (CMAGIC) method) [Wang et al., 2003], SALT (a spectral adaptive light curve

template for type Ia supernovae) [Guy et al., 2005], and SALT2 [Jennings et al., 2007]. In addition Conley and co-workers (2008) present a new empirical method for modelling SNIa light curves by manipulating a spectral template, namely SiFTO. This increases the ability of using more of the available data. Most of these current methods give relative distances to a precision of $\sim 7-10\%$ [Conley et al., 2008].

1.11.2 Tully Fisher Relation ($\leq$ 300 Mpc)

Tully and Fisher [1977] discovered a correlation between the absolute magnitude of a spiral galaxy and the width of the 21-cm emission line of neutral atomic hydrogen (HI 21 cm) . The width of the HI 21 cm line is a distance-independent observable which gives the rotational velocity of the spiral galaxy. This empirical relationship between the absolute magnitude and the maximum rotation velocity of spiral galaxies is well-known as the Tully - Fisher relation (TF). Specifically;

$$L \propto v_{rot}^{\alpha}, \tag{1.60}$$

or, in the logarithmic formulation;

$$M = A - b\eta, \tag{1.61}$$

where $M = -2.5\log(L) + \text{constant}$ is the absolute magnitude, and the velocity width parameter $\eta = \log(2v_{rot}) - 2.5$. The v_{rot} is a useful dimensionless measure of rotation velocity. It is important to note that the power law exponent α does not contain a unique value. The details of both the photometric and spectroscopic measurements affect on it. A typical result found in contemporary studies is $\alpha = 3$ [Willick, 1996].

Observers use different techniques to measure the relevant quantities like apparent magnitudes, diameters and internal velocity width. Further, they apply different corrections to the raw observables. As a result, there are various type of TF, K-band, B-band and R-band, for instance. Soon after the discovery of TF, it plays a vital role as a distance indicator, eventhough the physical origin of this relationship doesn't

understood clearly. Using TF, Sandage and Tammann recalibrated the previously determined distances to the M81-NGC and the Virgo cluster. The recalibrations results showed a similarity with previous results [Sandage and Tammann, 1976], proving that TF is a potential distance indicator. Another attempt carried out by Aaronson et al. [1979], an investigation performed with infrared photometry and TF, revealed that the dynamical origin of TF has a similar behaviour like $L = v^4$ power law for elliptical galaxies. Further, their studies confirmed TF as a powerful tool for determining the redshift-independent distances to the adjacent great clusters. The results from analyzes of 1,355 spirals using the Tully-Fisher relation to determine distances [Mathewson et al., 1992] lead to an appreciated coherence length and an amplitude of the local peculiar velocity coherence field. Numerous studies (Giovanelli et al. [1998]; Freudling et al. [1999]) emphasized the importance of TF as a secondary distance indicator in the study of the local peculiar velocity field.

Galaxy distance indicators are subjected to different uncertainties and biases, which may be reflected in the peculiar velocity field. Radial velocities used to infer the peculiar velocity of the galaxies, are often referred to the Cosmic Microwave Background frame. It should be remarked that galaxy distance estimates are subject to errors due to the scatter in the TF relation (Mo et al. [1998], Mathewson et al. [1992]) and uncertainties of the TF zero-point [Willick, 1991]. The possible presence of a small fraction of false velocities in the data induced by either galaxy peculiarities or observational errors in distance estimates should be taken into account. The scatter in Tully Fisher (σ_{TF}) can be discussed in three forms, magnitude and velocity width measurement errors, and intrinsic or *cosmic* scatter. Recent studies have suggested that the velocity width measurements errors and cosmic scatter are about equally important, contributing $0.25 - 0.3$ each [Willick, 1996]. The magnitude measurement errors are quite small compared to the others giving an overall σ_{TF} in about 0.4mag [Willick, 1996]. There is one galaxian property, where the TF scatter appears to vary, and that is the luminosity (velocity width) and brighter galaxies exhibit a smaller TF scatter than fainter ones (Federspiel et al. [1994]; Willick [1996]).

In 2008, Meyer and co-workers examined the optical and near-infrared Tully-Fisher relations for an HI-selected sample of galaxies. The intrinsic scatter and slope of the Tully-Fisher relation are measured by applying galaxy selection cuts to minimize observational errors [Meyer et al., 2008]. For the B-band relation, a slope of 3.40 $\pm$ 0.09 was obtained with an observed scatter of 0.40mag (intrinsic 0.33mag), and for the K-band relation a slope of 3.75 $\pm$ 0.08 was found with an observed scatter of 0.33mag (intrinsic 0.25mag). Including the observed HI masses to calculate baryonic relations, a slope of 3.91 $\pm$ 0.13 was obtained in B and 4.35 $\pm$ 0.14 in K. The baryonic Tully-Fisher relation (BTF) is a fundamental relation between baryonic mass and maximum rotation velocity. Trachternach and co-workers [Trachternach et al., 2009] found a scatter of 0.33 mag for the BTF relation using the data from the larger sample of Schombert et al. [1997], which is one of the largest samples of extreme field dwarf galaxies.

1.12 Malmquist bias

With the development of better observational methods, particularly resulting from the use of HST, the construction of the cosmological distance ladder is steadily improving. However, some fundamental difficulties occurred because of the noisiness of the distance indicators. For example, Tully-Fisher has a typical distance error dispersions of about 20% for an individual galaxy. When applying the distance indicators to estimate peculiar velocities these scatters would cause systematic errors for the results, and this effect is known generically in the literature as *Malmquist bias*.

According to Karl Gunnar Malmquist (1920), the Malmquist bias can be described as the bias occurs in a luminosity distribution of observable galaxies in a flux-limited sample. The mean luminosity of observable galaxies is brighter than the underlying population of galaxies because the intrinsically fainter galaxies would be missing from the sample at large distances. Nearer the observer, galaxies with average or below-average luminosity can also be seen. Hence, this bias depends on the distance from the observer. Malmquist bias is a statistical effect and formally can be evaluated

using probability theory.

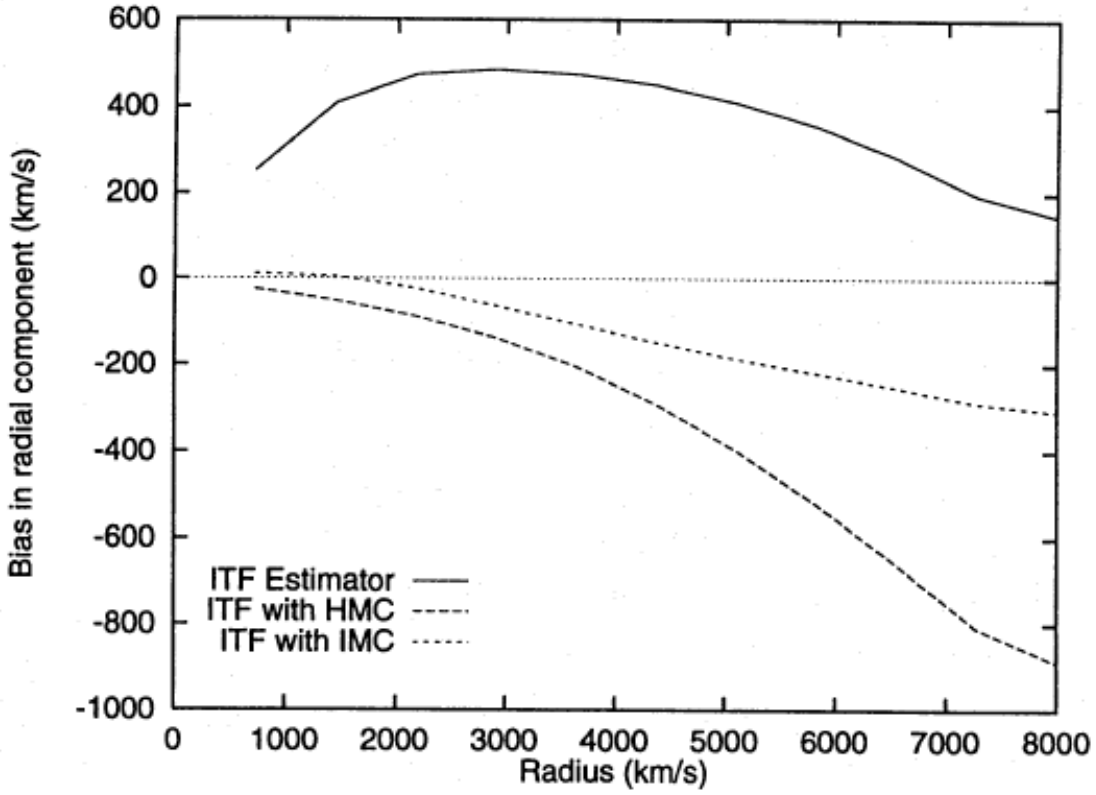

Figure 1.11: An example of the influence of the Malmquist bias in distance determination. This figure shows the bias as a function of distance for POTENT velocity recoveries of quiet Hubble flow with galaxies drawn from a homogeneous universe. Solid line referred to the inverse Tully-Fisher estimator in the raw form (ITF estimator). The dashed and the dotted lines referred to the homogeneous Malmquist correction (HMC) and the inhomogeneous Malmquist correction (IMC). Figure 4, Newsam et al. [1995].

Developing a method for correcting Malmquist bias is a widely discussed topic and numerous attempts have been reported (Willick [1994]; Hendry and Simmons [1995]; Teerikorpi [1998]; Gonzalez and Faber [1997]). Most of these studies were carried out by considering the Malmquist bias in two categories [Teerikorpi, 1998].

- The systematic average error in the distance modulus μ for a class of galaxies with *derived* $\mu = \mu_{der} =$ constant.

- The systematic error in the average derived distance modulus $[\mu_{der}]$ for the class of galaxies with *true* $\mu = \mu_{true} =$ constant.

Teerikorpi [1997] named these two as the *Malmquist bias of the first kind* and the *Malmquist bias of the second kind.* The bias of the first kind is the classical Malmquist

bias introduced by Malmquist (1920). In literature these two biases have appeared under different names (Table 1.2). Teerikorpi [1990a] separated the study of the Hubble diagram into *distance against velocity* and *velocity against distance*. Hendry and Simmons [1995] considered *Bayesian* and *frequentist* approaches in terms of mathematical statistics. Strauss and Willick [1995] used the terms *Malmquist bias* and *selection bias*, where they emphasized by selection the availability of galaxies restricted by some limit (flux, magnitude, angular diameter).

Table 1.2: Different names of the Malmquist bias

Author	Nomenclature	
Kapteyn [1914]	Problem II	Problem I
Landy and Szalay [1992]	General Malmquist bias	–
Han [1992]	Geometry bias	Selection effect
Teerikorpi [1990b]	V against r	r against V
Sandage [1988]	Classical	Distance-dependent
Hendry and Simmons [1995]	Bayesian	Frequentist
Willick [1994]	Inferred-distance problem	Calibration problem
Strauss and Willick [1995]	Malmquist bias	Selection bias
Teerikorpi [1995]	M-bias of the first kind	M-bias of the second kind

Gonzalez and co-workers found that the Malmquist bias associated with the H_0 Key Project, where determination of the distance to the Virgo cluster is of order 6-8% [Gonzalez and Faber, 1997]. While numerous studies are involved in methods of correcting the Malmquist bias, some are focused their studies to find methods to calibrate the distance indicators without using the Malmquist bias corrections.

According to a technique developed by Theureau et al. [1998], the normalized distance method (NDM) does not require any explicit bias correction for the calibration steps. This was introduced as a reliable method for correcting Tully-Fisher distances. Hendry & Rauzy introduced a ROBUST method for measuring the Hubble parameter and also for fitting peculiar velocity field models, which address selection effects but are completely independent of explicit Malmquist bias corrections (we discuss about this method in detail in Chapter 3). The value they obtained is $H_0 = 66$ km s^{-1} [Hendry et al., 2001] and $\beta = 0.6 \pm 0.125$ [Rauzy and Hendry, 2000] . A third bias has been introduced by Butkevich et al. [2005] the *integral bias*, an extension for the first kind and the second kind of bias, while developing a method for determination

of regions unaffected by the bias. With the development and approach of various techniques, the calibrations of the distance ladder with redshift-distance indicators would gain more accuracy, minimizing the influence of Malmquist bias. This will be a significant advantage for the galaxy distance determinations and studies on the peculiar velocity fields.

1.13 Redshift surveys

Redshift surveys of galaxies are useful tools in understanding the large scale structure of the Universe. The data gathered from these surveys can be used to measure the cosmological parameters. Specifically, these data are essential in obtaining data for the peculiar velocity field of galaxies, and compare the galaxy distribution to the mass distribution. These surveys provide important information to improve the statistical knowledge of the galaxy distribution. The data obtained from pencil-beam surveys (one-dimensional) of nearby clusters suggested that the galaxy distribution in the Universe was very uneven [da Costa et al., 1996]. Such a survey was carried out by Sandage in 1978 with a median redshift of 1500 km s^{-1}. Although, the pencil- beam surveys are able to cover very small region of the space, and they are too narrow to provide enough information about the large scale structure.

The *Centre for Astrophysical Redshift Survey* (*CfA*, 1977), opened up a new era for the large scale sky surveys. The first CfA Survey considered measurements of radial velocities for all galaxies brighter than 14.5 [Geller and Huchra, 1983]. This survey produces the first large area and reasonably deep maps of large scale structure in the nearby Universe. Soon after, there were several similar attempts went on surveying the large scale structure. The second CfA survey (CfA2) was started by John Huchra and Margaret Geller and provided data about 18,000 bright galaxies in the northern sky. There were number of efforts carried out by several groups, performing even larger surveys appeared to be critical with the aim of gaining in-depth knowledge of more complex problems in the Universe.

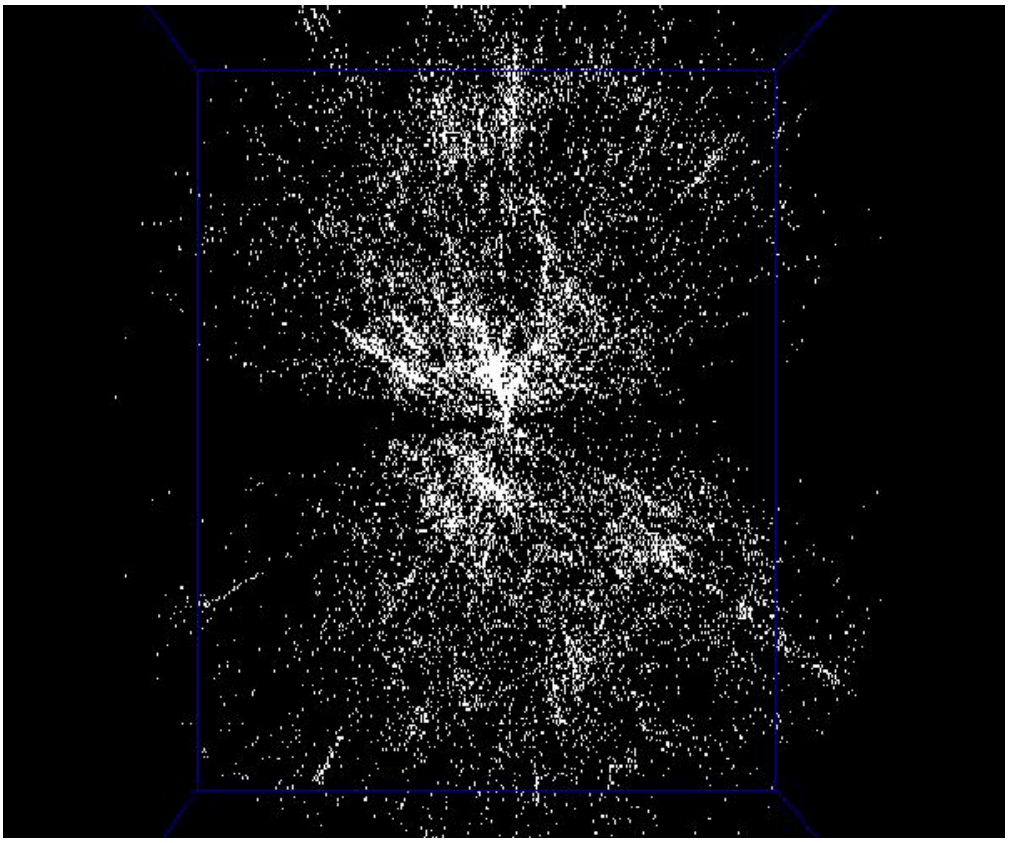

Figure 1.12: 3D distribution of approximately 30,000 galaxies from the CfA Catalog. The Milky Way is in the center of the plot. The dark empty horizontal cones are the areas in the zone of avoidance. The vertical scale of the plot is 160 Mpc ($q_o = 0.5$, $H_o = 100$).

1.13.1 IRAS

Zone of Avoidance: The dust and gas in the Milky Way absorbed the light from galaxies causing extinction at optical wavelengths, and therefore foreground stars can be confused with background galaxies. This band in the sky is well-known as the *Zone of Avoidance* (ZoA). Most of the redshift surveys encounter difficulties in detecting the objects in ZoA.

However, in the case of *longer wavelengths like infrared, the extinction becomes minor*. The Infrared Astronomical Satellite (IRAS) and 2MASS were designed using the above phenomenon. These surveys improved the sensitivity of the measurements allowing the astronomers to observe the unbiased all-sky at the infrared wavelengths [Neugebauer et al., 1984]. The IRAS, the first space-based observatory, was able to survey the 95% of all-sky in four wavelengths 12, 25, 60 and 100 μm. The point source catalogue (IRAS PSC) produced from this survey intended to be highly reliable ($> 99.8\%$). The survey reasonably cover over the unconfused portion of the sky

98% away from the galactic plane and other regions such as the Magellanic Clouds and the Gould belt [Rowan-Robinson et al., 1984]. Strauss et al. [1992] presented a redshift data for 2658 galaxies, from the IRAS database, and the sample is restricted to a flux of 1.936 Jy. A redshift survey with 2663 galaxies was given by Fisher in 1995. The galaxies are in the flux interval 1.2 - 1.936 Jy and considered to be an extension for the 1.936 Jy sample [Fisher et al., 1995a].

The IRAS Bright Galaxy Survey - Part I and Part II or BGS1 [Soifer et al., 1989] and BGS2 [Sanders et al., 1995] covers 83% of the sky. The BGS2, the extension of the original survey BGS1, use the optical telescopes in Mauna Kea and in Argentina, and extended the search for IRAS bright galaxies to southern declination ($\delta \leq$ -30°) and closer to the galactic plane ($5° < |b| \leq 30°$). These BGS1 and BGS2 surveys contain all extragalactic sources brighter than 5.24 Jy at 60 μm, and this was believed to be the best sample available in 1995, defining the infrared properties of galaxies in the local ($z \leq 0.1$) Universe [Sanders et al., 1995]. In 2003, Sanders and co-workers provided a new galaxy sample, namely the IRAS Revised Bright Galaxy Sample (RBGS) with 629 galaxies. This was a complete flux-limited survey of all extragalactic objects with total 60 μm flux density greater than 5.24 Jy [Sanders et al., 2003], which covered the entire sky surveyed by IRAS at Galactic latitudes $|b| > 5^0$ and a maximum redshift of 0.0876.

1.13.2 The IRAS PSCz survey

The IRAS Point Source Catalogue redshift (PSCz) survey is one of the surveys that involve in numerous studies in peculiar velocity field because of its completeness and the large sky coverage. The survey detected 15, 500 galaxies with a coverage of 84% of the sky and consists of redshifts for (almost) every galaxy in the IRAS PSC with 60 micron flux above 0.6 Jy (Saunders et al. [1999]; Saunders et al. [2000]). The redshift for 10,500 galaxies are taken form the literature and some other sources. Saunders and co-workers have observed the redshift for the other 4500 galaxies from January, 1992 to July, 1995. They used the Isaac Newton Telescope at La Palma Observatory, the Cerro Tololo Interamerican Observatory, and the Anglo-Australian Telescope for

their observations. The data catalogues we used for our study are obtained from this IRAS PSCz main catalogue.

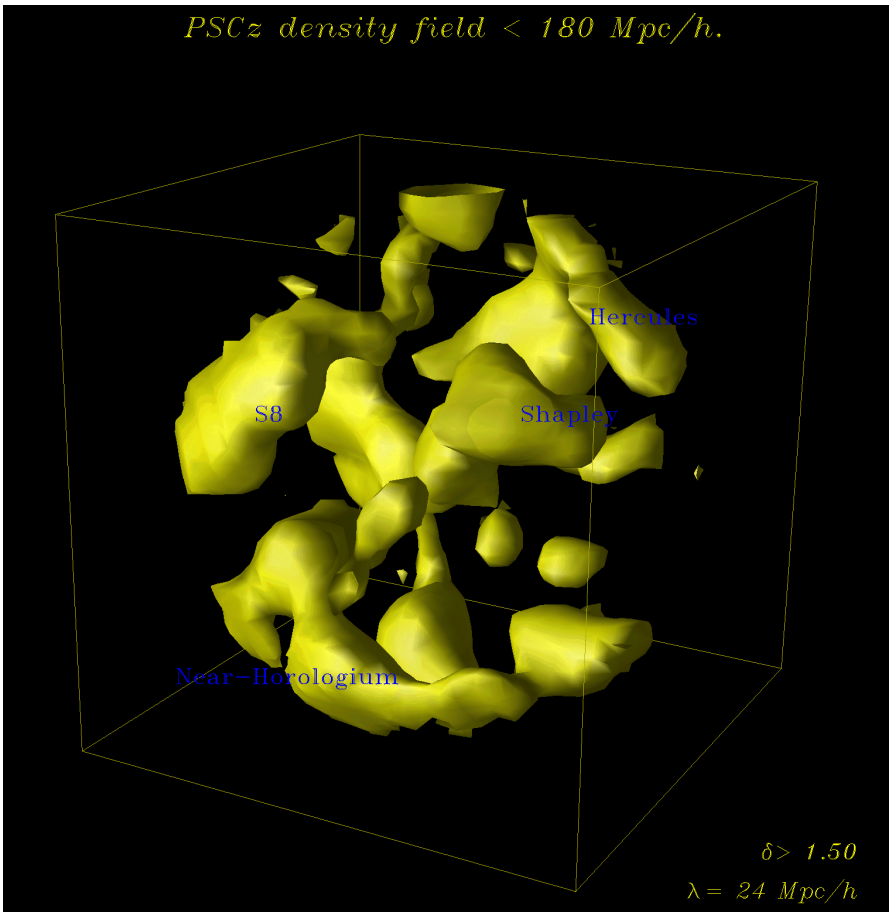

Figure 1.13: Isodensity contours of the galaxy distribution of PSCz galaxies within a sphere of radius 180 Mpc h^{-1}. icc.dur.ac.uk/Links/PSCz/psczM2-small.gif

1.13.3 SDSS

The Sloan Digital Sky Survey (SDSS), a digital photometric and spectroscopic survey, is one of the most significant low-redshift surveys. The SDSS covered 1/4 of the Celestial Sphere in the North Galactic cap and a sparser and deeper region in the Southern hemisphere [Abazajian et al., 2003], using a 2.5 meter telescope at Apache Point Observatory, in New Mexico. The flux densities of detected objects are measured almost simultaneously in five bands, which are u, g, r, i, and z [Lupton et al., 2001].

The SDSS-I (2000 - 2005) and SDSS-II (2005 - 2008) covered more than 8,000 square degrees of the sky and produced 3-D maps of 930,000 galaxies and more than 120,000

quasars. The main galaxy sample has a median redshift of 0.1, and there are redshifts for luminous red galaxies as far as $z = 0.4$. The third step of the survey, SDSS- III, is currently underway from 2008.

1.13.4 2dFGRS

The 2dF Galaxy Redshift Survey (2dFGRS), a major spectroscopic survey with high two degree field facilities, is designed to measure redshifts approximately for 250,000 galaxies. The 2dF multi-fibre spectrograph on the Anglo-Australian Telescope, which can observe 400 objects simultaneously over a 2° diameter field, was used for taking the observations [Colless et al., 2001]. A region spanning $80° \times 15°$ around the south galactic pole, another in the northern hemisphere spanning $75° \times 10°$ along the celestial equator, and also random fields scattered around the SGP strip were considered as the main survey regions. This survey covers 2,000 deg^2 and has a median depth of $z = 0.11$.

The 2dFGRS obtained spectra of 245,591 objects, in particular galaxies, brighter than a nominal extinction-corrected magnitude limit of $b_J = 19.45$ [Colless et al., 2001]. Reliable redshifts were obtained for 221,414 galaxies. Some of the main goals of 2dFGRS were to measure the galaxy power spectrum $P(k)$ on scales up to a few hundred Mpc, to measure the redshift-space distortion of the large-scale clustering that results from the peculiar velocity field, produced by the mass distribution and higher-order clustering statistics of the galaxy distribution to determine the bias parameter b [Colless et al., 2001].

1.13.5 2MASS

The Two Micron All Sky Survey (2MASS) is the large-area near-infrared survey which was carried out after the last near-infrared survey, the so-called Two Micron Sky Survey (TMSS; Neugebauer & Leighton 1969). TMSS covered 70% of the sky and detected about 5,700 celestial sources of infrared radiation. With the development of infrared detector technology, new sensitive array detectors can now detect astronom-

ical objects over 100 million times fainter than that of detected in the TMSS.

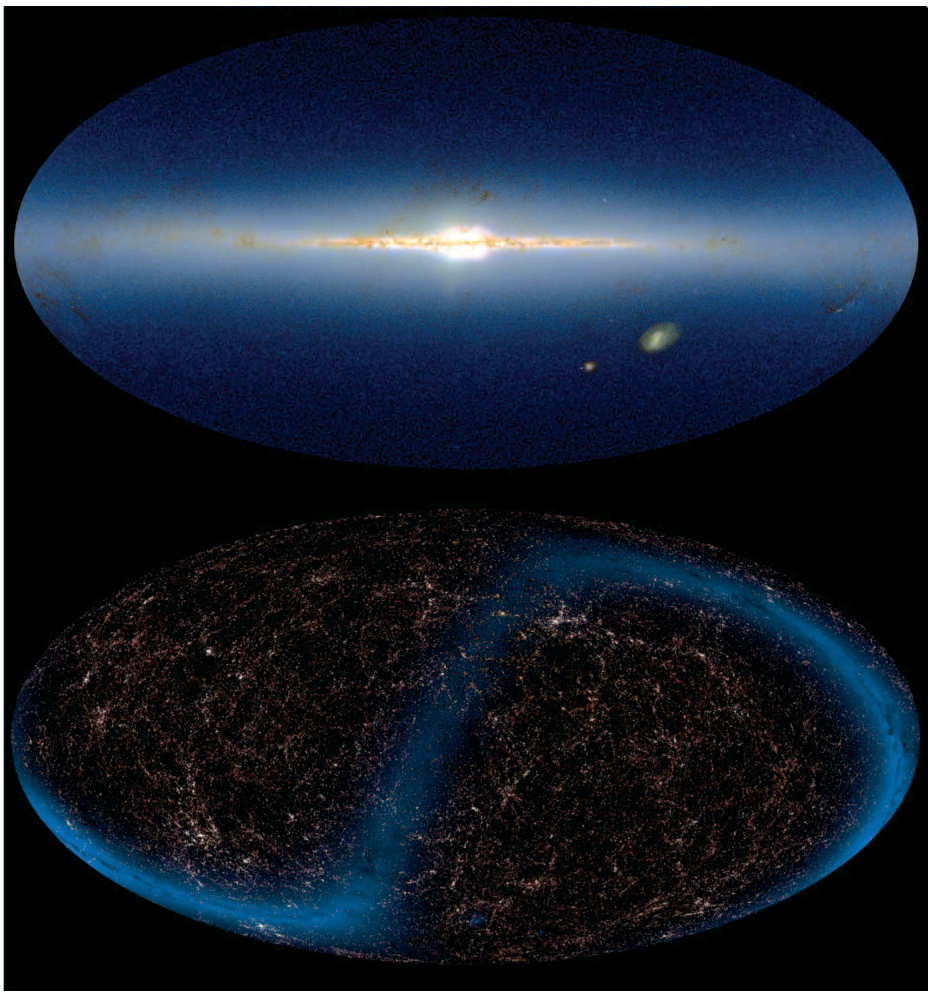

Figure 1.14: Full-sky distribution of point (2MASS PSC) (top) and extended (2MASS XSC) (bottom) sources. Point sources are presented in Galactic coordinates centered on $b = 0°$ and $l = 0°$. The extended source map is presented in equatorial coordinates and centered at $\alpha = 180°$ and $\delta = 0°$. The faint blue band in the extended source map traces the Galactic plane as represented by the Point Source Catalog. Intensity is proportional to source density. The images are a colour composite of source density in the J (blue),H (green), and Ks (red) bands. Figure 13 of Obrić et al. [2006]

The Two Micron All Sky Survey (2MASS) project is designed to close the gap between our current technical capability and knowledge of the near-infrared sky. This survey provided important information about the large-scale structure of the Milky Way and the Local Universe. Between 1997 June and 2001 February, 2MASS observed 99.998% of the celestial sphere in three near-infrared bands, using two 1.3 m diameter telescopes, one at Mount Hopkins, Arizona, and the other at Cerro Tololo, Chile [Skrutskie et al., 2006]. Each telescope was equipped with detectors which simultaneously observed in the J (1.25 μm), H (1.65 μm), and Ks (2.17 μm) bands.

The magnitude limits of the 2MASS, with respect to Vega, were 15.8, 15.1 and 14.3 respectively. The detectors were sensitive to point sources brighter than 1 mJy at the 10σ level, corresponding to these magnitude limiting. The point-source photometry is considerably better than 10% precision at this level, and the astrometric uncertainty for these sources is less than 0.2 arcsec. The 2MASS catalogs contain positional and photometric information for 470,992,970 point sources (2MASS PSC) and 1,647,599 extended sources (2MASS XSC) [Obrić et al., 2006]. Figure (1.14) illustrates the full-sky distribution of both these sources.

2MASS has achieved an 80,000-fold improvement in sensitivity relative to earlier surveys. This is a very important advantage for the next generation of infrared space missions, such as HST/NICMOS, the space Infrared Telescope Facility (SIRTF), and the James Webb Space Telescope. Further, this will be benefitted from for the powerful ground-based facilities, such as Keck I, Keck II, and Gemini, which require a new census with vastly improved sensitivity and astrometric accuracy.

1.13.6 6dF survey

The approach of the wide-field spectrographs is one of the major issues on the improvements of present knowledge of the structure and constituents of the low-redshift Universe. The 2dF Galaxy Redshift Survey (2dFGRS; [Colless et al., 2001]) and the Sloan Digital Sky Survey (SDSS; Abazajian et al. [2009]) provided data of luminosity and clustering properties of galaxies and the amount and spatial distribution of dark matter, with high precision [Jones et al., 2009]. Other advantages of such surveys are providing considerable constraints on ΛCDM models of the Universe. With these important applications it is understood that, a combined redshift and peculiar velocity survey has impressive ability to offer better constraints on parameters of cosmological interest than survey of redshift alone [Burkey and Taylor, 2004].

The 6dF Galaxy Survey (6dFGS) is a spectroscopic survey of the entire southern sky (83 %) with $|b| > 10$. This is a multi-fiber spectrograph attached to the UK Schmidt Telescope (UKST) and named after telescope's field of view, which is 6 de-

grees in diameter. 6dF is the third generation of multi-fiber spectrograph (Figure 1.15) on the UKST. The near-infrared total magnitudes are taken from the Two Micron All-sky Survey (2MASS) Extended Source Catalogue (XSC; Jarrett et al. [2000]) and the limits were (K,H,J) = (12.65, 12.95, 13.75) [Jones et al., 2009].

The measurements taken in between January 2002 and July 2003, for 52,048 spectra

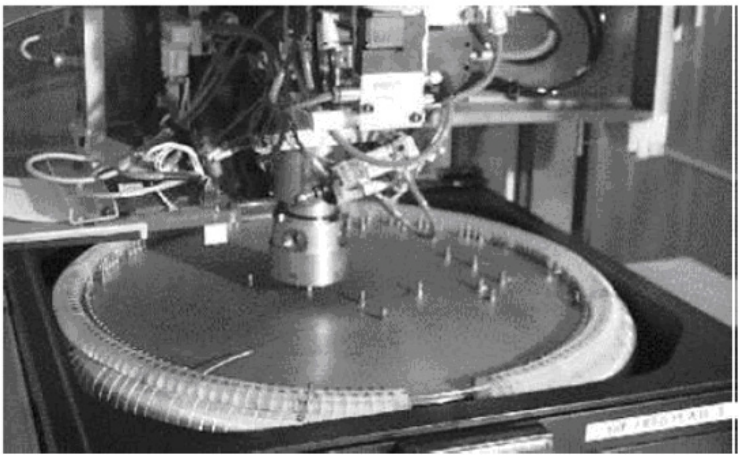

Figure 1.15: 6DF, an automated fiber positioner, configures magnetic fibre buttons on the curved focus of the field assembly under precise robotic control (5μ m) at the exact co-ordinates of celestial objects. Figure 1 of [Wakamatsu et al., 2003].

from 46,474 unique galaxy redshifts were published as the first data released (DR1), [Jones et al., 2004] The median survey redshift is $z = 0.055$, which is less than that of the 2dfGRS or SDSS surveys. The Second Incremental Data Release (DR2), also an extension for DR1, was contained observations from January 2002 to October 2004, with 89,211 spectra from 83041 unique galaxy redshifts over roughly two-third of the southern sky [Jones et al., 2005].

The final data release of the 6DF Galaxy Survey [Jones et al., 2009] contains 136,304 spectra which yields 110,256 new extragalactic redshifts and a new catalogue of 125,071 galaxies with a median redshift $z = 0.05$. A database including velocity dispersions, distances and peculiar velocity of more than 10,000 bright, early type galaxies will be released in the future. This will contain redshift maps of the southern local Universe ($z <= 0.1$), showing nearby large-scale structures unseen to date. Future surveys with next generation radio telescopes such as ASKAP and the SKA will also benefit from the legacy of 6dFGS, as they probe comparable volumes

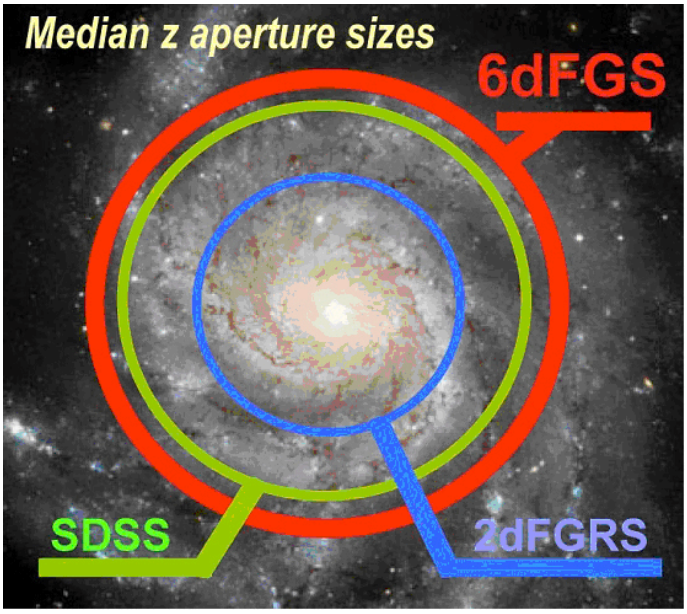

Figure 1.16: Comparison of 6dF with SDSS and 2dFGRS

in HI with the benefit of prior redshift information across most of the southern sky.

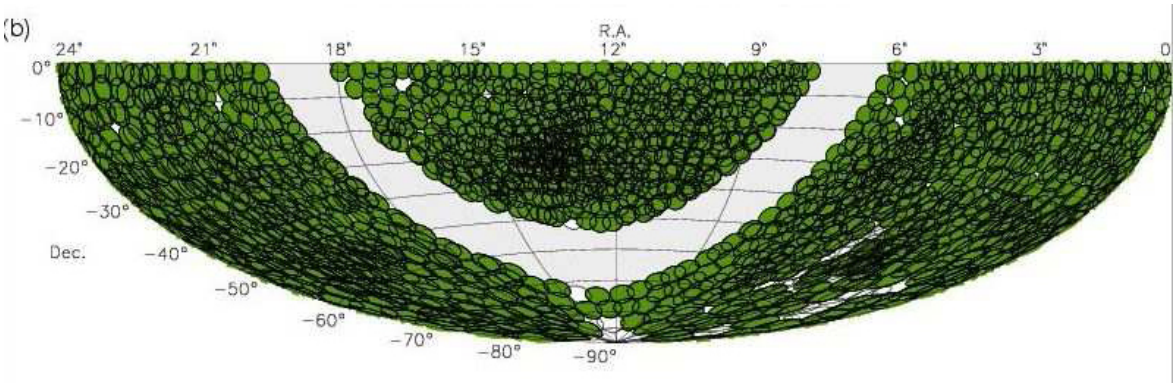

Figure 1.17: Full 6dFGRS field coverage (filled circles) and unobserved target fields (open circles). Figure 1 of Jones et al. [2009].

1.13.7 SKA

The Square Kilometre Array (SKA) is a global project to plan and construct the next-generation international radio telescope operating at metre to centimetre wavelengths with a total approximate collecting area of 1 km^2 [Schilizzi et al., 2008]. The concept of the SKA is based on develop a telescope to provide two orders of magnitude increase in sensitivity at metre to centimetre wavelengths.

There are five main goals in SKA;

1. Cradle of Life.

2. Probing the Dark Ages.

3. The origin and evolution of Cosmic Magnetism.

4. Strong field tests of gravity using pulsars and black holes.

5. Galaxy evolution, cosmology and dark energy.

As a global effort, SKA is currently governed by an international association of 15 countries. The two potential sites currently proposed for the SKA are, near Boolardy station in Western Australia, and in the Karoo region of South Africa [Gaensler, 2009]. With high flexibility of the instruments, SKA will cover large-area of the Universe in a broad range of frequencies from 0.07-0.25 GHz in many different operating modes. At an observing frequency of 1.4 GHz, the SKA will have a maximum angular resolution of $0.02''$ and a field of view of 20 square degrees. These qualities allow SKA to become the most sensitive (50 times more sensitivity than VLA - Very Large Array) radio telescope with outstanding survey capability compared to any other existing radio facility. A unique capability of radio arrays is that they can begin taking data long before the full facility is complete. Under these abilities SKA going to begin its operations in around 2016 [Gaensler, 2009].

1.13.7.1 SKA Polarization Pathfinders

Although the complete construction of the array takes most of the next decade, a large number of pathfinder facilities are already taking data or under construction [Gaensler, 2009]. Many of these will conduct experiments on polarimetry, Faraday rotation and magnetic fields.

New telescopes with such capabilities include:

- The Galactic Arecibo L-Band Feed Array Continuum Transit Survey (GALFACTS), a 1.4-GHz survey [2008 - 2012], which will map the entire polarized sky visible to Arecibo.

- The Low Frequency Array (LOFAR) is situated in the Netherlands and Germany, which explores polarization over the whole northern sky at very low

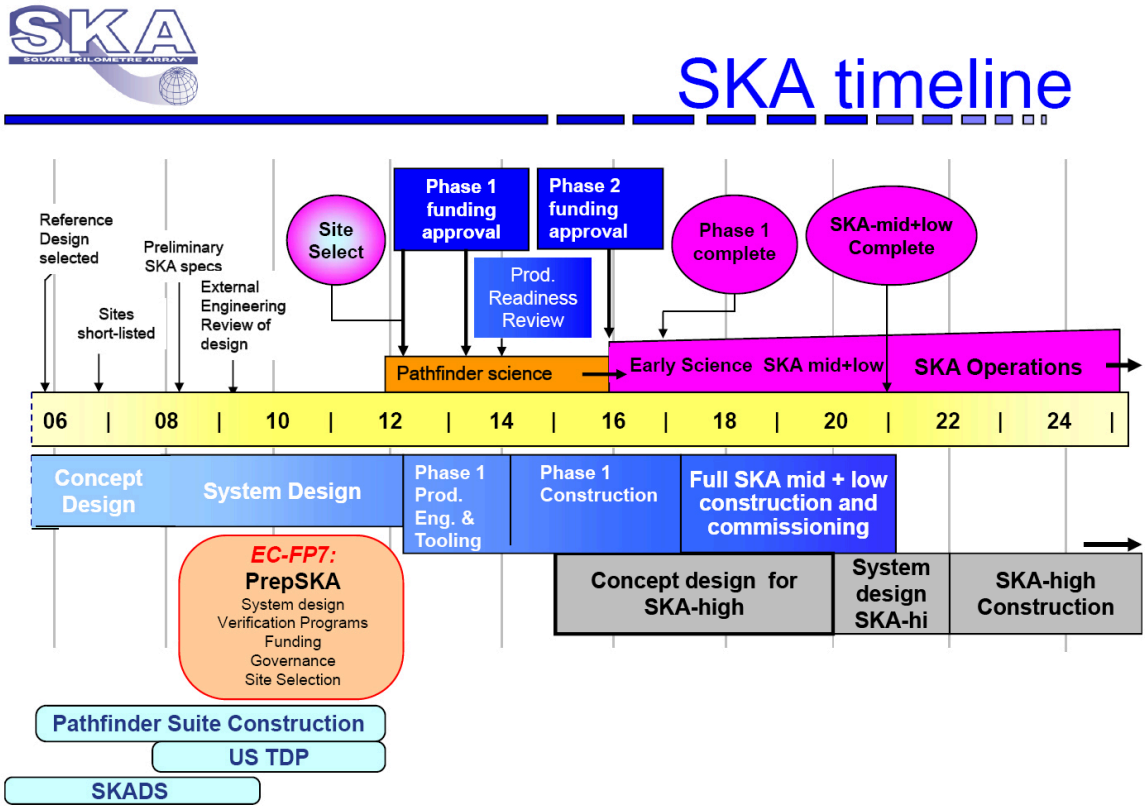

Figure 1.18: The timeline of SKA. From www.skatelescope.org

frequencies ($\nu = 30 - 80, 110 - 240$ MHz). The LOFAR has taken its first observation in July, 2009.

- The Allen Telescope Array (ATA) in northern California, a newly operational facility that holds a wide field of view (5 deg^2 at 1.4 GHz) and can carry out very large continuum surveys.

- The Square Kilometre Array Molonglo Prototype (SKAMP), a refurbishment of the Molonglo Observatory Synthesis Telescope in south-eastern Australia, which will provide 18,000 m^2 of collecting area for studying diffuse polarization at an observing frequency $\approx$ 1 GHz over the wide fields.

- The Murchison Widefield Array (MWA), an interferometer being built in Western Australia. This will study polarized emission over wide fields in the frequency range 80-300 MHz.

- The Expanded Very Large Array (EVLA), a substantial upgrade to the VLA

in New Mexico, providing greatly improved continuum sensitivity, frequency coverage and correlator capability.

- The Karoo Array Telescope (MeerKAT), an array of 80 12-metre dishes, each equipped with a wideband feed covering the frequency range 0.7-10 GHz.

- The Australian SKA Pathfinder (ASKAP), an array of 36 12-metre antennas to be built on the Western Australian SKA site. ASKAP will be a very wide-field survey instrument (30 $\deg^2$ at 1.4 GHz), and will be able to study polarization at a range of spatial scales in the frequency range 700-1800 MHz [Johnston et al., 2008]. The main goal of ASKAP is to detect one million galaxies in atomic hydrogen emission across 75% of the sky out to a redshift of 0.2 to understand galaxy formation and gas evolution in the nearby Universe.

The interesting details about the polarized sky are exposed by GALFACTS and the ATA, with even more powerful facilities such as the EVLA and ASKAP now under construction. In particular, the new wide-field sensitive surveys that will be carried out by ASKAP and the EVLA will allow us to derive catalogues of polarized extragalactic source counts down to fluxes of a microjansky or lower. These activities will culminate in the next decade with the arrival of the SKA, and a consequent exploration of the full magnetic Universe.

Figure 1.19: ASKAP antennas. www.ska.gov.au

1.13.8 Widefield ASKAP L-band Legacy All-sky Blind survey: WALLABY

WALLABY is one of the pathfinder of ASKAP. Some other HI surveys related to ASKAP are in operation, for example DINGO (Deep Investigation of Neutral Gas Origins, [Meyer, 2009]), GAMA survey (Galaxy And Mass Assembly, [Driver et al., 2009]). This thesis focuses on WALLABY survey. WALLABY is an extragalactic neutral hydrogen survey over 75% of the entire sky ($-90^\circ < \delta < +30^\circ$) and will detect up to 500,000 galaxies to a redshift of 0.26. This will produce the largest sample of galaxies that is possible to observe in a given observing time with ASKAP (Australian Square Kilometre Array Pathfinder). In addition, WALLABY is a very important survey because of its completeness and will provide the most homogeneous HI survey with multi- wavelength sample of galaxies yet made, and will be an important pathfinder for the key SKA HI science project.

The primary objectives of WALLABY are to examine the HI properties and large-scale distribution of these galaxies in order to study:

1. Galaxy information and the missing satellite problems in the Local Group. In a pair of orbiting galaxies, if one is considerable larger than the other, the larger one is called the *primary* and the smaller one is defined as the *satellite*.

2. Evolution and star-formation in galaxies.

3. Mergers and interactions in galaxies.

4. The HI mass function (HIMF) and its variation with galaxy density. The HIMF is the number of galaxies observed binned by particular hydrogen masses. HI mass is the mass of cold neutral hydrogen found abundant (rich) in close, non-metallic galaxies. The MF reveals that the gas mass in these galaxies is much greater than the stellar mass (i.e. $m_{gas} >> m_{star}$). The HIMF can be used to describe the formation and evolution of galaxies, and identifying the local counterparts of high-redshift Lyman-α absorption lines seen in quasar [energetic and distant galaxy with a high luminosity centre (AGN)] spectra.

5. Cosmological parameters related to the gas-rich galaxies.

6. The nature of the cosmic web.

To achieve the above goals , WALLABY has to observe each 30 deg^2 ASKAP field for a single period of 8 hrs in the frequency range 1.13 to 1.43 GHz (i.e. -2000 $< cz <$77,000 km/s). The WALLABY survey parameters are well-aligned with the other all-sky surveys such as SSP's (Survey Science Projects to be conducted by ASKAP), for example EMU (Evolutionary Map of the Universe). WALLABY will have a flux sensitivity some 20 times better than HIPASS, and will detect dwarf galaxies out to a distance of $\sim$60 Mpc, massive galaxies to $\sim$500 Mpc, and super-massive galaxies to the survey edge of 1 Gpc. HIPASS (HI Parkes All Sky Survey) is a survey for neutral atomic hydrogen (HI), which was in operation in 1997 to 2002 and used the radio telescope in Parkes Observatory, Australia. This is the first blind survey, which covered the entire southern sky with sky coverage of 71% and identified 5,317 sources emitting HI's signature wavelength.

WALLABY science includes :

- Continuum emission from gas-rich galaxies: a measure of the star-formation rate.

- Damped Lyman - α absorption analogs: a measure of disk cross-section and gas temperature.

- Use of gas dynamics to assist in the interpretation of the magnetic field properties of the nearby extended galaxy population.

For each detected galaxy, WALLABY will deliver the following data products:

1. 3D data cubelet.

2. Integrated HI spectrum.

3. HI column density image.

4. Velocity field.

5. Dispersion field.

6. Radio continuum image.

7. Full parametrization of galaxy properties.

Also WALLABY will search for faint HI emission in well-selected optical/IR galaxy sample by co-adding (*stacking*) the HI data at the position and redshift of the optical/IR galaxy. The redshift data will be taken from the 2MASS-selected galaxy surveys such as 6dFGS, and Deeper 2MASS, SkyMapper, VST and VISTA. WALLABY will play a key role as an accurate zero-redshift anchor for later SKA HI surveys of the Universe and will inform SKA HI survey designers to identify parameters which are presently poorly known.

Up to this point we have discussed about the important aspects in Cosmology. In the next section we discuss about the data analysis techniques we used throughout our work.

1.14 Data Analysis techniques

1.14.1 Smoothing and shot noise

Redshift surveys examine only a portion of the density field of the Universe. Generally, the galaxy surveys include the galaxies brighter than some flux limit in a specific region in the space (i.e. incomplete sky coverage and limited depth). With the approach of infrared-selected surveys, the problem of sky coverage has been solved to some extent (only >10% of sky unobserved). In addition, the redshift catalogues based on the IRAS database are flux limited, and consequently the number density of galaxies declines sharply with distance. Inevitably, the estimate of the density field becomes subject to large statistical uncertainties in large distances. The uncertainty raised by this fact in the density fields is known as the shot-noise or Poisson sampling noise. The obvious solution for this effect is filtering of the smoothed galaxy density field -for example using the Wiener filter, which minimises the variance between the reconstructed and true density fields (Weiner 1949).

1.14.2 Cumulative distribution function & the Probability Integral Transform

The cumulative distribution function (CDF) completely describes the probability distribution of a real-valued random variable X. CDF of a random variable X evaluated at a number x, is the probability of the event that X is less than or equal to x, and this is a monotonically increasing function from 0 to 1. These are also used to specify the distribution of multivariate random variables.

For every real number x, the CDF of a real-valued random variable X is defined by;

$$x \mapsto F_X(x) = P(X \leq x) \tag{1.62}$$

where the right-hand side represents the probability that the random variable X takes on a value less than or equal to x. Then the probability that X lies in the interval $(a, b]$ is therefore $\mathrm{F}_X(b) - F_X(\mathrm{a})$ if $a < b$.

It is conventional to use a *capital* F for a cumulative distribution function, in contrast to the *lower-case* f used for probability density functions and probability mass functions. The CDF of X can be defined in terms of the probability density function f,

$$F(x) = \int_{-\infty}^{x} f(t)dt \tag{1.63}$$

The CDF is very important when discussing the *probability integral transform* (PIT). If X is a continues random variable with a probability density $p(x)$ and CDF $P(x)$, then X can be transformed into a new random variable Y by applying the *probability integral transformation theorem*,

$$Y = P(x) \sim U[0, 1]. \tag{1.64}$$

This is a very useful application in statistical data analysis which can be used to test a set of observations, and see whether they are reasonable modelles arising from a specified distribution. The PIT can be used to construct an equivalent set of values

that mimic the distribution of the original data set. We used the PIT theorem to sample the distance distribution of the mock objects to mimic the PSCz velocity field published by Branchini et al. [1999].

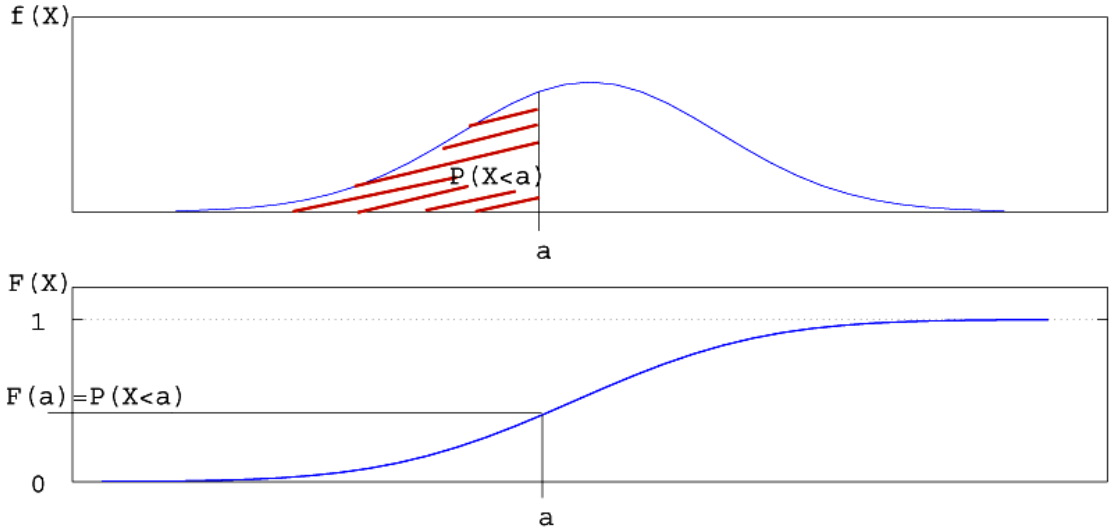

Figure 1.20: The relationship between the probability density and the CDF.

1.14.3 χ^2 hypothesis test

The χ^2 hypothesis test plays a major role in constraining the value of the distortion parameter β (e.g. Hudson [1994], Neill et al. [2007]). Hudson [1994] considered the D_n - σ and infrared Tully Fisher galaxies and used Uppsala General Catalogue of Galaxies (UGC) and the ESO-Uppsala Survey of the ESO(B) Atlas to predict the peculiar velocity fields. Further, he used an expression similar to the equation (1.65) with a velocity error of 150 km s^{-1} and obtained a best-fit value 0.5 ± 0.06 for β. Riess et al. [1997] considered the IRAS 1.2 Jy peculiar velocity and used SNIa to compare the observed and peculiar velocity field and obtained 0.40 ± 0.15 from χ^2 minimization. Using the IRAS PSCz peculiar velocity field with SNIa data, Radburn-Smith et al. [2004] obtained $\beta = 0.55 \pm 0.06$. There have been numerous studies carried out using the χ^2 hypothesis test. Table 1.3 summarizes the reported best-fit values for β from some of the studies, applying the minimum χ^2 statistic for different redshift survey data samples.

We also applied the χ^2 minimization to estimate the best-fit value of β for the mock

Table 1.3: β values obtained from χ^2 minimizing. SBF represent the surface brightness fluctuation and PS denotes the power spectrum.

β	Data	Reference
0.50 ± 0.06	D_n-σ, IRTF, ESO, UGC	Hudson [1994]
0.40 ± 0.15	SNIa, IRAS 1.2Jy	Riess et al. [1997]
0.30 ± 0.10	SNIa, ORS	Riess et al. [1997]
$0.42^{+0.10}_{-0.06}$	SBF, IRAS 1.2Jy	Blakeslee et al. [1999]
0.26 ± 0.08	SBF, ORS	Blakeslee et al. [1999]
0.39 ± 0.17	SMAC, IRAS 1.2Jy	Hudson et al. [2004]
0.55 ± 0.06	SNIa, IRAS PSCz	Radburn-Smith et al. [2004]
0.49 ± 0.04	SNIa, SBF, TF, 2MASS	Pike and Hudson [2005]
$0.49\ ^{+0.08}_{-0.05}\ 0.04$	PS,SFI	Park and Park [2006]
0.50	SNIa,IRAS PSCz	Neill et al. [2007]

peculiar velocity fields. These velocity fields were designed to mimic the next generation of galaxy redshift surveys. We have applied the following expression,

$$\chi^2 = \sum_{i=1}^{n} [\ \frac{(V_{i,obs} - V_{i,pred})^2}{\sigma_{i,cz}^2 + \sigma_{i,d}^2}\ ], \tag{1.65}$$

where $V_{i,obs}$ and $V_{i,pred}$ are the observed and the predicted radial peculiar velocities, respectively. These values depend on β. σ_{cz} represents the scatter in redshift determination as well as the errors in the PSCz predictions due to shot noise or non-linear peculiar-velocity contributions and σ_d is the scatter in the radial distance of the objects, (i.e. galaxies, distance indicators,etc.)

Chapter 2

The fate of the galaxy peculiar velocity field with the future redshift surveys

In this chapter we discuss our attempt to reconstruct the peculiar velocity field by smoothing the redshift distortion parameter β. The distance indicators have significant influence on reconstructing the density and velocity fields. The imprecise distance estimates to individual galaxies can make a huge impact when constrain the value of β. Therefore, we aim to analyze the impact on estimating the value of the *redshift distortion parameter* β with the development of the redshift surveys (e.g. SKA, ASKAP, WALLABY). We will also investigate what improvements need to be introduced in order to increase the accuracy of the current reconstruction methods of the peculiar velocity field.

The flow of the chapter is as follows: Section 2.1 is about the redshift distortion. We discuss about two types of redshift distortion, the Finger of God (§ 2.1.1) and Kaiser Effect (§ 2.1.2). And the third part, §2.1.3, defines the meaning of β. Section 2.2 contains the information about the methods used to reconstruct the peculiar velocity field, *via* the iterative method (§ 2.2.1) and the non-iterative method (§ 2.2.2). Then, following Section 2.2, Section 2.3 approaches to discuss the techniques used to constrain β, under the density-density (§ 2.3.1) and velocity-velocity (§ 2.3.2) compar-

isons. Section 2.4 describes the important information about the distance indicators we used in this study under the first three parts. The fourth part, § 2.4.4, gives an overview about the PSCz velocity field (§ 2.4.4). Section 2.5 introduces the method we used to constrain β. Section (2.6) presents details about the mock data files we generated to mimic the future redshift surveys. Finally, Section 2.7 and 2.8 compiles the results, discussion and the conclusions.

2.1 The redshift distortion

Galaxies, that trace the matter density in the universe have different motions depending on the cosmology. In a perfectly homogeneous Universe redshift surveys, in principle, can measure the radial distance from the observer precisely, and the mapping from real space (r-space) to redshift space (s-space) would be the identity mapping. However, this relationship will be more complex in an inhomogeneous Universe, because the existence of any inhomogeneous structure induces peculiar velocities that cause a distortion in the mapping between r-space and s-space. The peculiar velocities of galaxies cause the radial distance (i.e. true distance), r, to appear displaced along the line-of-sight in redshift space. Then, the redshift distance, s, of a galaxy differs from the true distance r along the line of sight. In the Local group frame, the redshift distance s_{LG} of a galaxy with true distance r (relative to the observer) can be expressed as (i.e. the mapping from r-space to s-space),

$$s_{LG} = r + \widehat{\mathbf{r}}.(\overrightarrow{\mathbf{v}} - \overrightarrow{\mathbf{v}}_{LG}) \tag{2.1}$$

where $\overrightarrow{\mathbf{v}}_{LG}$ denotes the peculiar velocity of the Local Group and $\widehat{\mathbf{r}}$ is the unit vector along the line of sight (i.e. the radial direction of the observer). $\overrightarrow{\mathbf{v}}$ is the measured peculiar velocity of the object. These displacements lead to redshift distortions (Figure 2.1) and they occur in a different manner on small and large scales due to the different characteristic behaviour of peculiar velocities on the above scales. These are known as *Finger of God* and *Kaiser Effect*, respectively.

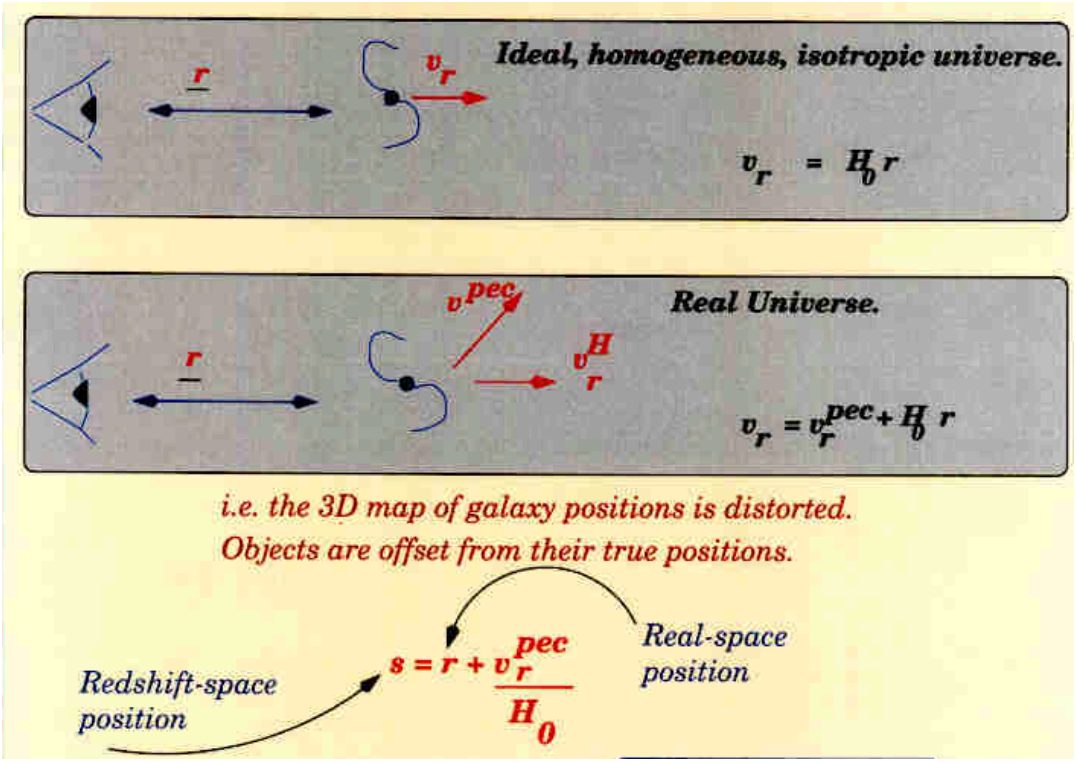

Figure 2.1: Redshift distortion. H_0 is the Hubble constant, v_r^{pec} is the radial peculiar velocity and v_r is the recession velocity. http://moriond.in2p3.fr/J00 /mercredi/Ballinger/02.html

2.1.1 The Fingers of God

On small scales, the effect of peculiar velocities on galaxies causes a considerable stretch of the redshift space distribution along the line of sight. This phenomenon is known as the Fingers of God (FoG), as long thin stripes in redshift space point directly back at the observer (Figure 2.2). This phenomena can mostly be seen in the cores of clusters.

2.1.2 The Kaiser effect

The redshift distortion occurs in a different way on large scale. Galaxies, in outside of the cluster, are moving towards the cluster due to their gravitational pull, with peculiar velocities bound to a central mass. A galaxy on the far side of a cluster may hold a negative peculiar velocity, and appear closer to us in redshift space than in real space. On the other hand, a galaxy in between the observer and the cluster has a positive peculiar velocity, and appears further away from its actual distance relative to the observer. This differs from the Fingers of God in a way that the peculiar velocities are coherent, not random, towards the central mass. The clustering of

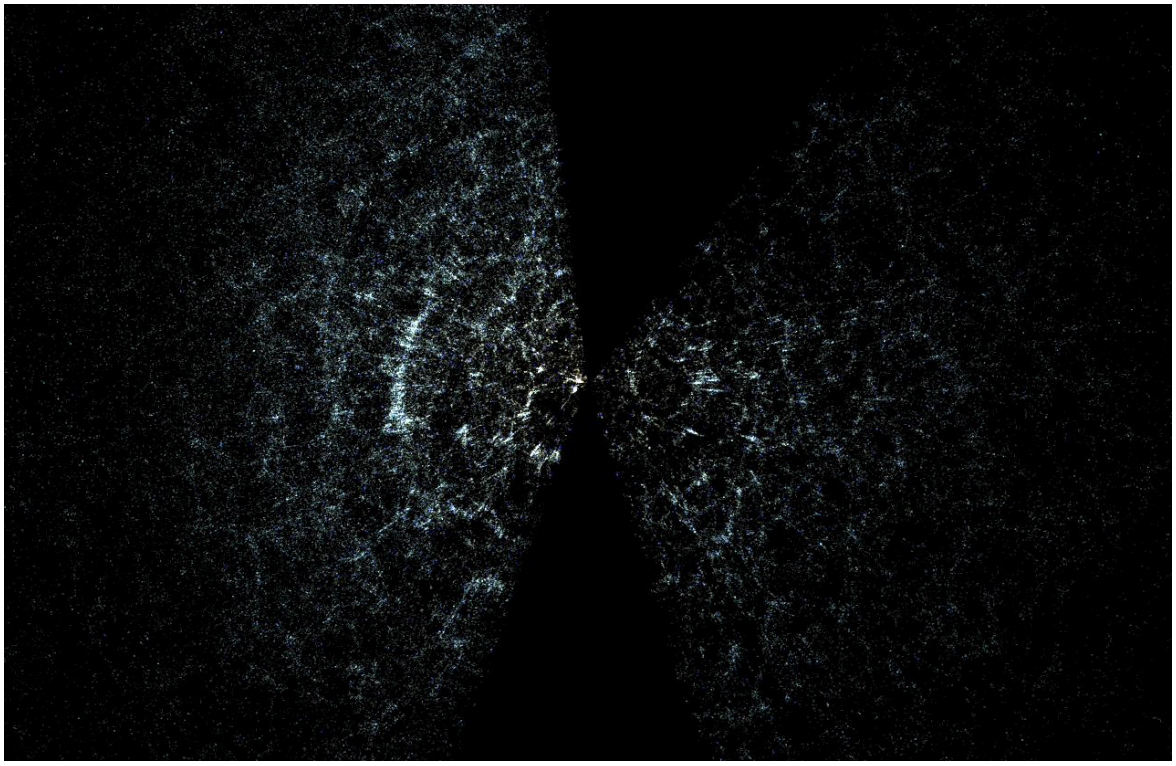

Figure 2.2: The Fingers of God: This figure is a slice through the SDSS 3-dimensional map of the distribution of galaxies. The little stripes heading towards the center are the Fingers of God effect. As shown in this figure, the Finger of God effect mostly occurs in the cores of clusters. [http://astro.uchicago.edu/cosmus/projects/fog/]

galaxies in the real-space and in the redshift space shows a significant difference because of this coherent peculiar velocity field which is associated with large scale structure [Kaiser, 1987] and this redshift distortion is known as the *Kaiser effect*. Because the separation between galaxies is much greater than the typical random velocities, the effect of peculiar velocities in clustering, and in particular on the galaxy two-point correlation function $\xi(r)$, can be neglected [Shanks et al., 1983]. Figure 2.3 illustrates the way of distortion of a spherical overdensity by peculiar velocities on large scales (left) and small scales (right).

2.1.3 Linear redshift distortion parameter β

The amplitude of the distortion on large, linear scales yields a measurement of the linear redshift distortion parameter, $\beta_g = \Omega_m^{0.6}/b_g$ where Ω_m is the cosmological density and b_g is the linear bias parameter, which is used to represent the linear bias between the galaxy density fluctuation (i.e. luminous matter) and the total density fluctuation. The subscript on β and b denotes the sample which is considered to map

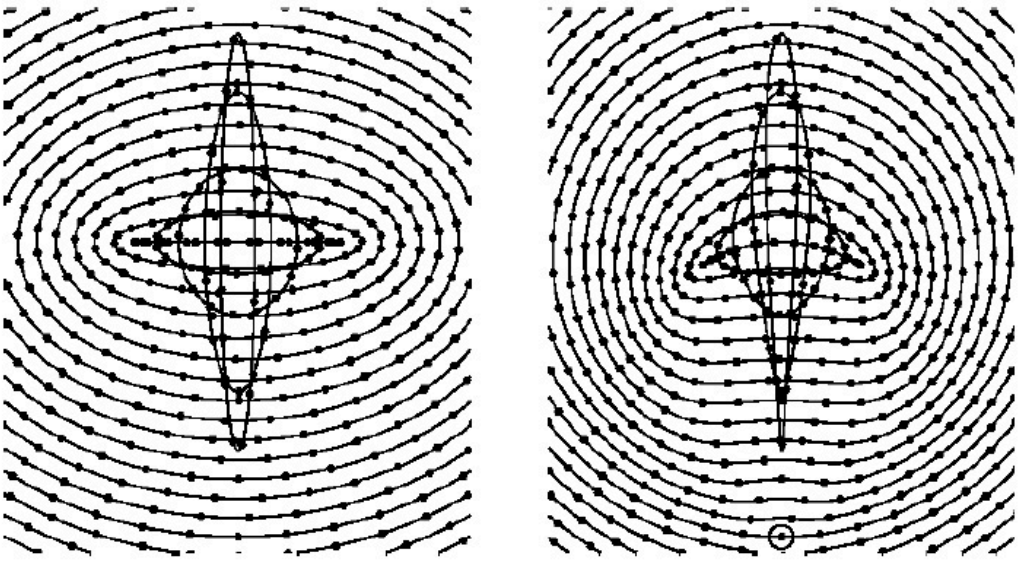

Figure 2.3: The distortion of a spherical overdensity due to peculiar velocities, in the redshift space. Left: *Kaiser effect*, the appearance of the overdensity on large scales. The overdensity is far from the observer (who is looking upward from somewhere way below the bottom of the diagram), and the distortions are effectively plane-parallel. Right: *Finger of God*, the distortion of the overdensity on small scale. The overdensity is closer to the observer (large dot), and the large scale distortions appear kidney-shaped, while the finger of god is sharpened on the end pointing at the observer. [Hamilton [1998], Figure (1).]

the density field. In general, the bias and hence β depend on the sample, due to the variation of clustering amplitudes.

2.2 Reconstructing the peculiar velocity field

Measurement of β is based on the relationships between the peculiar velocity and density fields predicted by Gravitational Instability for the linear regime [Peebles, 1980].

$$\nabla.V_p(r) = -H_0\beta\delta_g \tag{2.2}$$

$$V_p(r) = \frac{H_0\beta}{4\pi}\int d^3r' \frac{\delta_g(r'-r)}{|r'-r|} \tag{2.3}$$

The equation (2.2) is known as the *linear velocity-density relation.* In these equations, the galaxy number density fluctuation field δ_g is assumed to be related to

the underlying mass density fluctuation field (δ) by the simple linear biasing model $\delta_g = b\delta$. The accuracy of β is limited by the accuracy of the reconstruction method and the estimated radial peculiar velocity field $V_p(r)$. The peculiar velocity field can be estimated iteratively or non-iteratively.

2.2.1 Iterative method

The iterative method is based on solving the equation (2.3) in real space, iteratively. The initial data required for the calculation process are taken from the all-sky redshift surveys. First, a smooth δ_g is estimated from the observed distribution of galaxies in the redshift survey and without considering the redshift distortion of the galaxy peculiar motion. The peculiar velocity field $V_p(r)$ can be calculated from the equation (2.3) for an assumed value of δ_g. Then the observed values of smoothed density field at each position r, need to be corrected by using the predicted radial peculiar velocity field. This step is performed iteratively until the convergence occurs. This iterative method has become very popular and has been applied to varies types of surveys, such as IRAS 1.9Jy/1.2Jy (Strauss et al. [1992]; Fisher et al. [1995a]), the QDOT survey [Kaiser et al., 1991] IRAS PSCz survey [Branchini et al., 1999] and 2MASS [Pike and Hudson, 2005].

2.2.2 Non-iterative method

The iterative method described in the previous section is computationally expensive, which reveals the usefulness of identifying a direct, non-iterative relation between the dynamical fields in real space and redshift space. The most obvious fact of the direct approach is to establish a unique one-to-one mapping between the initial and final positions of galaxies, which is valid until shell crossing singularity occurs (i.e. all Jacobi fields have finite limits in an orthonormal parallel propagated frame, as they approach the singularity. A Jacobi field is a vector field along a geodesic (the shortest path between points in the space), which describes the difference between the geodesic and an infinitesimally close geodesic. This one-to-one mapping is known as the Zel'dovich approximation.

2.2.2.1 The Zel'dovich approximation

The evolution of cosmic structure in terms of a fluid description can be analyzed using a Lagrangian or an Eulerian formulation. If the coordinate system of the fluid elements defines to be attached to the fluid elements themselves, the Lagrangian coordinates of the elements remain fixed with the growth of the fluid. If the coordinate system is attached to points in space with respect to the fluid elements, this will move as the fluid evolves in the Eulerian point of view. The co-moving coordinates of the homogeneous background cosmology remain fixed as the Universe expands, and can be described as a combination of the both Lagrangian and Eulerian. However the fluid will grow with a perturbation on the background model causing changes in the position and velocity of the fluid elements. This complicated behaviour can be simplified by applying the linear theory with the assumption, that the changes in the co-moving positions are negligible as the Universe expands. Based on this fact, it is possible to consider that the structures grow simply according to the linear growth factor, f (Section 1.3, equation 1.29). The Zeldovich approximation extends the linear theory by assuming that the difference between the Lagrangian position ($\mathbf{q}$) and the Eulerian position ($\mathbf{x}$) of a fluid element may be written as the product of a time-dependent function and a purely spatially-dependent function;

$$\mathbf{x}(\mathbf{q}) = a(t)[\mathbf{q} + D_1(t)\psi(\mathbf{q})] \tag{2.4}$$

where $D_1(t)$ is the growing mode and $\psi(\mathbf{q})$ is the velocity component, which provides the particle displacement with respect to the initial position. This is related to the gradient of the gravitational potential $\Phi_o(\mathbf{q})$ originated by the initially linear fluctuations, according to

$$\psi(\mathbf{q}) = \nabla\Phi_o(\mathbf{q}). \tag{2.5}$$

Thus we see that the Eulerian position is simply the Hubble expansion with a separable perturbation. The Zel'dovich approximation gives an excellent approximation to the true evolution of the velocity and density field to the mildly non-linear regime, Hendry [2001] and references therein. This is very useful when providing the non-linear versions of equation (2.2) and equation (2.3), allowing the density and velocity

fields to be related on smaller scales. For an irrotational peculiar velocity field, the transformation of the galaxy distribution from the real space to redshift space can be described from its Jacobian. The gradient of a scalar velocity potential, Φ of an irrotational peculiar velocity field can be written as:

$$V(s) = -\nabla\Phi(s) \tag{2.6}$$

By expanding the density and velocity potential in terms of spherical harmonics (in redshift space), a differential equation can be obtained as [Nusser and Davis, 1994];

$$\frac{1}{s^2}\frac{d}{ds}(s^2\frac{d\Phi_{lm}}{ds}) - \frac{1}{1+\beta}\frac{l(l+1)}{s^2}\Phi_{lm} = \frac{\beta}{1+\beta}(\delta_{lm} - \frac{1}{s}\frac{d\log\phi}{d\log s}\frac{d\Phi_{lm}}{ds}), \tag{2.7}$$

where s is the redshift space radial coordinate and ϕ is the radial selection function of the sample. Solutions of the above equation give rise to the spherical harmonic coefficient, Φ_{lm}, on a given shell in redshift space. The differentiation of the velocity potential provides the peculiar velocity field which depends on β. This is the inverse Tully-Fisher method (ITF), which was originally introduced by Nusser and Davis [1994]. This method can be applied only for small scales.

With the assumption of linear theory, Fisher et al. [1995b] proposed an alternative non-iterative method. In this approach the density field is expanded in angular spherical harmonics and radial Bessel function. In the same way as ITF method, the expansion coefficients in real space and redshift space can be obtained as a function of β by considering the radial selection function and the angular mask of the redshift survey. In this method, the Wiener filter is used for the correction of shot noise. The accuracy of the reconstruction method was proved by using the mock redshift surveys generated from N-body simulations. The ITF method and Fisher et al. method have shown similar results [Hendry, 2001] and both were better than the iterative reconstruction method. Peebles [1990] proposed another direct method considering the real space density and velocity field, and this is based on the least action principle, which can be applied to a discrete N-body system. The least action approach has been developed further *via* the path Interchange Zeldovich Approximation (PIZA)

method by Croft and Gaztanaga [1997] and Valentine et al. [2000]. The peculiar velocity field can be obtained using the above methods. In the next section we discuss about the techniques that have been used to constrain the value of β by using the peculiar velocity fields predicted from these methods.

2.3 The methods of constraining β

There are two principle methods for the determination of β which is illustrated in Figure 2.4. As shown in the Figure 2.4, the two methods are known as the density-density comparison and the velocity-velocity comparison.

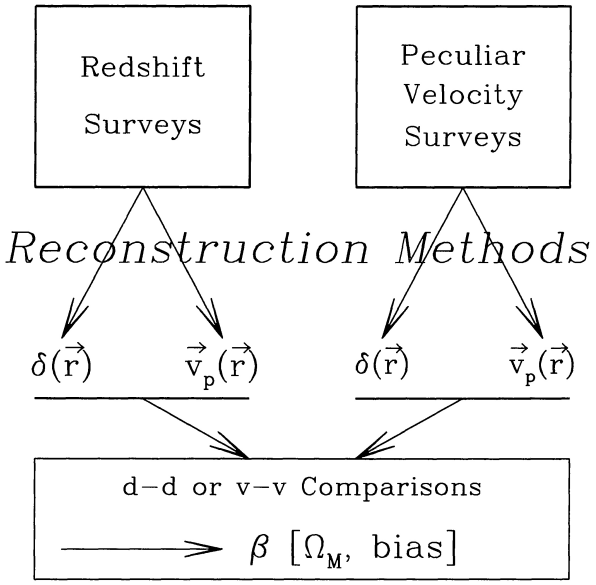

Figure 2.4: Reconstruction methods of β

2.3.1 Density-density comparison

The *density-density* comparison (δ-δ) is based on the velocity-density relation [i.e. Equation (2.2)]. In this case, $V_p(r)$ has to be reconstructed from the peculiar velocity data and its divergence is compared with the directly observed density δ_g (the velocity-density relation), which gives rise to β. However, the peculiar velocity data must be converted into a three dimensional (3-D) velocity field. Typically the POTENT method is applied to reconstruct these 3-D peculiar velocity fields [Masters, 2008].

2.3.1.1 The POTENT reconstruction procedure

The aim of the POTENT analysis is to recover the minimal systematic errors of velocity and density fields, where the true 3-D velocity field is sampled uniformly with infinite density, and smoothed with a spherical Gaussian window of a fixed radius [Bertschinger and Dekel, 1991]. The POTENT approach is applicable under the assumption of the irrotational behaviour of the peculiar velocity field. This was initially proposed by Bertschinger et al. [1990] where they recovered the 3-D velocity field using the expected irrotationality of gravitational instability (GI). The irrotational velocity $\mathbf{v}$ can be written as the gradient of a scalar velocity potential, (Φ), at any position r,

$$\Phi(r) = \int v.dl \tag{2.8}$$

where the line integral is path independent. In the case of considering only the radial path, we may write,

$$\Phi(r) = \int u(r')dr', \tag{2.9}$$

where $u(r')$ is the radial component of the peculiar velocity at distance, r', along the line of sight. Then $v(r)$ can be obtained by taking the differentiation of the above equation.

This whole procedure can be summarized for the following steps [Dekel et al., 1999] :

1. Prepare the radial velocities for POTENT analysis, in particular correcting for Malmquist bias in different ways, including grouping.

2. Smooth the peculiar velocities into a continuous, uniformly smoothed radial velocity field that has minimum bias.

3. Apply the Ansatz of gravitating potential flow to recover the potential and three-dimensional velocity field.

4. Derive the underlying mass density field by an approximation to GI in the mildly nonlinear regime.

5. Evaluate the remaining systematic and random errors using mock catalogs.

The advantage of POTENT is that the 3-D peculiar velocity field can be obtained directly from the radial components, which are directly obtained from the redshift-independent galaxy distance indicators. The MAXFLOW algorithm developed by Newsam et al. [1995] adapts the standard POTENT procedure to include non-radial paths, which avoids a region where galaxy sampling is particularly poor. Even though POTENT has some drawbacks, its measures the mass density field directly (without any assumption of galaxy biasing), and therefore POTENT becomes a very useful reconstruction method.

Measuring β by comparing peculiar velocity and redshift survey data became a realistic goal with the approach of full-sky redshift surveys Willick et al. [2000]. Particularly, the IRAS point source catalogue (IRAS PSCz) and large, homogeneous sets of Tully-Fisher (TF) data were the major developments for the reconstructing methods. The POTIRAS comparison, a $\delta - \delta$ comparison done by Dekel et al. [1993], has estimated $\beta_I = 1.29$, where subscript I is used when the galaxy density field is obtained by IRAS. In this procedure, the velocity field was reconstructed using the POTENT algorithm, and its divergence was compared with the galaxy density field from IRAS. This method has been widely used with much improved velocity data, obtaining a value $\beta_I = 0.89 \pm 0.1$ [Sigad et al., 1998].

2.3.2 Velocity-velocity comparison

The other method of estimating β is the *velocity - velocity* (v-v) comparison. One measures δ_g and *reconstructs* $\mathrm{V}_p(r)$ from redshift survey data for a sample of galaxies with *redshift-independent* distances. The expression used for this method is the integral form of linear-velocity density relation, [i.e. Equation (2.3)], with an assumed value of β. Then these model values are compare with the *observed* radial peculiar velocities to check the plausibility of the applied theoretical scenario and to obtain the *best-fit* value of β.

The studies based on the v-v comparison gave rise to lower values of β_I. One of the attempts was considered the *Least Action Principle* to predict peculiar velocities,

which gave $\beta_I = 0.35$ [Shaya et al., 1995]. Willick [1996] have applied a maximum likelihood method, the so-called VELMOD method, to 838 galaxy TF sample ($cz_{LG} \leq$ 3000 km s^{-1}) obtained from the Mark III catalogue and obtained $\beta_I = 0.49 \pm 0.07$. Increasing the redshift limit to $cz_{LG} = 7500$ km s^{-1}, they have expanded the sample to 1876 galaxies and considered the quadrupole velocity residuals with VELMOD, obtaining $\beta_I = 0.50 \pm 0.04$ [Willick and Strauss, 1998]. Riess et al. [1997] were compared the peculiar velocities of nearby SNIa with those predicted by the gravity fields of IRAS and Optical Redshift Survey (ORS). Their best-fit values of β are 0.40 for IRAS and 0.30 for ORS.

In 1999, Branchini and co-workers applied a likelihood analysis to estimate β using the PSCz galaxy survey. They obtained $\beta_I = 0.6^{+0.22}_{-0.15}$ using the information available on bulk velocities, cosmological dipoles and local shear [Branchini et al., 1999]. Radburn -Smith and co-workers used the PSCz density field and SNIa, which yield that the most consistent value for the linear redshift distortion parameter is $\beta_I = 0.5$ [Radburn-Smith et al., 2004]. The 2MASS catalogue and redshift data were used by Pike and Hudson [2005] to reconstruct the local density field. Further, they applied the VELMOD method with the assumption of gravitational instability obtaining a best-fit of $\beta_k = 0.49 \pm 0.04$ comparing the peculiar velocity field within 65 Mpc/h. Basilakos and Plionis [2006] have re-examined the PSCz dipole induced on the Local Group of galaxies by the (IRAS) galaxy distribution and found $\beta_I = 0.44$ and 0.49 in redshift and real space, respectively. In 2006, Park & co-workers have measured the momentum and density power spectrum from the peculiar velocities of galaxies in the SFI catalogue and obtained $\beta_S = 0.49^{+0.08}_{-0.05}$ [Park and Park, 2006]. A v-v comparison done by Neill et al. [2007] confirmed that the best model is $\beta_I = 0.5$.

2.3.3 The density-density versus the velocity-velocity comparison.

These results show that the δ-δ comparison produces β closer to unity; while the v-v comparisons, several based on the same redshift and velocity samples as PSCz,

yield $\beta = 0.5$. Neither the δ-δ nor the v-v comparison is essentially more valid as both are strongly based on the linear gravitational instability theory. The δ-δ comparisons are highly dependent on the distance indicator data to estimate the full 3-D velocity and its derivatives. These estimations are hugely dependent on the accuracy of the distance indicator data. However, in general, these distance data contain considerable uncertainties with the influence of the bias, Malmquist bias for example.

On the other hand, in the v-v comparison, the distance indicator data is used essentially in its raw form. In this case, only the redshift survey data, which is intrinsically more accurate, is subject to complex, model-dependent manipulation. Under these circumstances, the v-v analysis are more likely to be precise on constraining β and the best-fit is favoured for the low values, $\beta_I = 0.4$-0.5 [Willick et al., 2000]. The next section presents important details about the distance indicators that we used for our study.

2.4 The distance indicators and the future redshift surveys

For the analysis, most commonly used distance indicators have been considered: Type Ia supernovae and the Tully Fisher relation. We also consider the recently proposed *standard sirens*.

2.4.1 Type Ia supernovae $\leq$ 1000 Mpc/h

Type Ia supernovae (a detailed description of SNIa can be found in Section 1.11.1), the most popular distance indicators, provide an independent test of the gravitational instability paradigm and constrain the mass density. Figure 2.5 shows how bright and easily detectable a supernova is. With their high intrinsic luminosity and the presence of all kind of galaxies from ellipticals to irregulars, type Ia supernovae have demonstrated their enormous potential as distance indicators [Isern et al., 1989]. Light curves from the Calan/Tololo Survey [Maza et al., 1993] and the CfA survey

[Riess et al., 1997] yield distances with 5% - 10% uncertainty over the redshift range $0 < cz < 36\ 000$ km/s (i.e. $z < 0.12$). Although the sample of observed SNIa is relatively small, the depth and precision of SNIa distances provide some advantages for the reduction of random errors, one SNIa is worth 10 TF. Systematic bias, Malmquist bias for instance, which rises with the square of the distance uncertainty, is also 10 times smaller for SNIa distances. The future surveys are going to increase the observable number of SNIa and also the number of samples observed if needed. We simulate data for the future surveys as well as the current.

Figure 2.5: The type Ia supernovae have a enormous potential as distance indicators with their high intrinsic luminosity. The supernova in the bottom left of the above picture shows how bright and visible the SNIe are, even when the entire galaxy is in view. www.lancs.ac.uk/ug/hemmingl/

2.4.2 Tully Fisher relation $\leq$ 300 Mpc/h

Distance indicators based on empirical relationships between galaxy luminosity and internal velocity, known as the Tully Fisher relation, yield individual distance uncertainties of 20% - 25% [Riess et al., 1997]. We propose that, with datasets containing large numbers of sampled galaxies, the TF relation will give considerably good results despite the fact that there is a larger distance scatter for each galaxy. Therefore

we try to find the applicability of this concept for the future surveys, for example the WALLABY, which may observe about 500,000 objects up to a redshift of 0.26 (i.e. cz = 78,000 km s^{-1}). However, as the mock samples are needed to be consistent with the IRAS PSCz galaxy distribution, for the consistency of our analysis, we considered TF data for the 15,000 mock objects lying within $cz \leq$ 15,000 km s^{-1}. Apart from analyzing the traditional distance indicators, our study also focused on a newly defined distance indicator, the so-called *gravitational standard sirens*. Having previously discussed the role of a standard candle, the next section gives a brief introduction to the concept of a standard siren.

2.4.3 The next era of the distance scale: the standard sirens

A gravitational wave (GW) can be described as a fluctuation in space-time curvature, which propagates as a wave. According to the General Theory of Relativity this phenomenon can occur due to accelerations of the mass distribution of objects like neutron stars, white dwarfs or black holes (Figure 2.6).

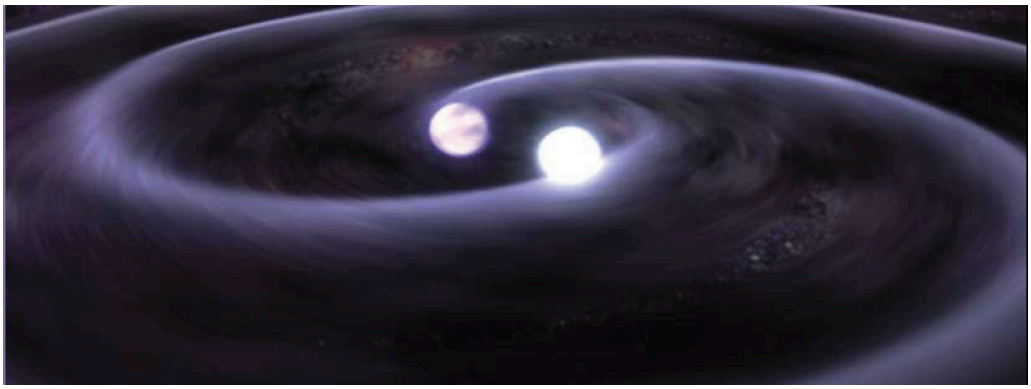

Figure 2.6: An artistic impression of a compact binary white dwarf system. Gravitational waves generated by the orbital motion, radiate energy out of the system. [NASA/Dana Berry, Sky Worlds Digital]

According to the standard concordance cosmology, galaxies form *via* a hierarchical series of mergers of cold dark matter halos. The high-resolution cosmological simulations suggest that the Milky Way resulted from the merger of more than 1000 *proto-galaxies*, which began forming at z > 20. Further, these proto-galaxies may contain black hole *seeds* that merged with each other at high redshift, around $z = 15$ [Koushiappas et al., 2004]. If these seeds hold a mass of about 10^4 solar masses or

more, they may produce gravitational waves during the merge that will be detected by LISA very easily, even at z $\sim$ 15 [Hendry and Woan, 2007]. Laser Interferometer Space Antenna (LISA) is the first step of the space-based gravitational astronomy, which is supposed to launch in 2020. LISA will operate in an environment with completely free low-frequency noise sources present on Earth and will be able to see the universe in a band (0.1 mHz to 1 Hz) corresponding to the orbital periods of several important classes of binary compact objects. A detailed description of LISA can be found in Hendry and Woan [2007], Tinto et al. [2002], Cutler [1998].

Highly sensitive detectors are crucial in terms of detecting the quadratically lower flux sensitivity of a strain. The proposed gravitational wave observatory LISA will have a strain (i.e. the geometrical measure of deformation, representing the relative displacement between particles in the material body) sensitivity of 10^{-23} in 1 year at a frequency of a few millihertz. This strain corresponds to a magnitude limit of +18, which is comparable to an observer using a 1m telescope at a dark site, i.e. the observable magnitude limit would be the same as above. LISA will give us a deep view of the sky expanding our opportunities to explore the Universe, as the current generation of ground-based observatories (LIGO, VIRGO) are limited to the brightest sources only. The expected total event rate and redshift distribution of massive black hole(MBH) mergers is uncertain and LISA will play a key role of taking measurements of these quantities. Further, the current knowledge of hierarchical galaxy formation imply that LISA have the ability to observe a merger rate in the range 1 to 1000 yr^{-1} [Haehnelt, 1994]. These observations can be used to calibrate the extragalactic scale, which is one of the most important applications of GW. LISA may improve the quality of the distance scale through the use of GW as high-precision distance indicators. These new distance indicators have recently introduced to the cosmological scales as *standard sirens*.

The reason why standard sirens can be used as cosmological distance indicators is given below. The gravitational waveform emitted by a MBH merger is robustly dependent on the chirp mass of the binary system (i.e. a quantity that is based on the

masses of both bodies in the system), where the amplitude of the waveform is inversely proportional to the distance. Under these conditions, the luminosity distance of the binary system can be measured accurately [Schutz, 1986]. However, the gravitational radiation from the MBH merger will be redshifted due to the expansion of the universe, similarly as in the electromagnetic radiation. This phenomenon is known as the mass-redshift degeneracy; analysis of the waveform in fact only constrains the product of the mass parameters and the factor $(1 + z)$, where z is the redshift of the source. The crucial point of using the standard sirens as the distance indicators is search for an electromagnetic counterpart of the MBH binary source in order to compare the redshift with the distance. Once this has been approached, the z can be revealed from the electromagnetic spectrum, and the mass-redshift degeneracy broken. A careful analysis carried out by Holz and Hughes [2005] yielded the cosmological potential of standard sirens. They suggested that the characteristic distance uncertainties would be about 1% for an MBH at $z \sim 1$, (which is the uncertainty we have used in our calculations). This is indeed an important fact as standard sirens will show a high accuracy compared to the SNIa. Lang and Hughes [2006] developed the Holz and Hughes analysis allowing to consider the precession of an MBH binary induced by the spins of the black holes. This approach reduces the measurement uncertainty on the luminosity distance by a factor of 2 or 3, to about 0.2 - 0.4 % at $z \sim 1$.

One of the drawbacks of the standard sirens is that the gravitational radiation is subjected to weak gravitational lensing by intervening matter. As a result the amplitude of a MBH binary waveform may be magnified or de-magnified by the presence of large scale structure along the line of sight towards the source. Therefore, corrections needed to be considered for the weak gravitational lensing for the each source in order to estimate the luminosity distance with high accuracy. If LISA can obtain number of sirens closer to the upper limit of the expected rate (i.e. 1000 yr^{-1}) then the influence of the lensing would be strongly reduced. On the other hand, weak lensing may be relatively negligible for standard siren observations at $z < 1$ [Dalal et al., 2006]. A single MBH standard siren observed at $z < 0.5$ could measure the Hubble parameter to better than 1%. We generated several mock data catalogues to

represent these distance indicators. The next section give an overview of the main real data catalogue we used in this study.

2.4.4 PSCz velocity field

The data catalogue used in this work is the smoothed PSCz density field published by Branchini et al. [1999]. They used the completed PSCz redshift survey introduced by Saunders et al. [1999] to predict the velocity field. The main PSCz catalogue contains 15,411 IRAS galaxies across 84% of the sky [Figure 2.7]. The large sky coverage is one of the most important properties of the catalogue and the only excluded regions are two thin strips in ecliptic longitude that were not observed by IRAS, the Magellanic Clouds, and the area in the Galactic plane where the B-band extinction, AB, exceeds 2 mag. Branchini and co-workers used two methods to obtain the velocity field in the local universe (i.e. 150 Mpc h^{-1}), the iterative method and the non-iterative method . They have applied the iterative technique (Section 2.2.1) introduced by Yahil et al. [1991] with the Equation (2.3), and the non-iterative technique (Section 2.2.2), the ITF method developed by Nusser and Davis [1994] as the second method [i.e. Equation (2.7)]. One of the drawbacks of the PSCz survey is that the lack of data in the zone of avoidance. This problem was solved by applying a similar filling method used by Yahil et al. [1991]. The region at galactic latitude, $|b| \leq 8°$, was filled by replacing the synthetic objects with real PSCz galaxies at $|b| \leq 8°$ which are in the same longitude-distance bin. Masked regions at larger galactic latitudes are filled in with a random distribution of synthetic galaxies having the observed mean number density. However, the PSCz velocity field is incomplete in larger distances ($>$ 150 Mpc h^{-1}) (Figure 2.8) and becomes complete beyond 300 Mpc h^{-1} [Branchini et al., 1999]. A Gaussian filter of 6 Mpc h^{-1} was used to smooth the velocity field.

With the assumption of a high normalization for the matter power spectrum ($\sigma_8 =$ 0.87, the dispersion of the mass field smoothed on a scale of 8 Mpc h^{-1}), the best-fit value obtained for β is $0.6^{+0.22}_{-0.15}$ (1 σ). This is consistent with the result obtained for β from several studies using the v-v comparison. Branchini et al. [1999] have generated peculiar velocity fields for $\beta = 0.1$ to 1.0. For our study, we have used the

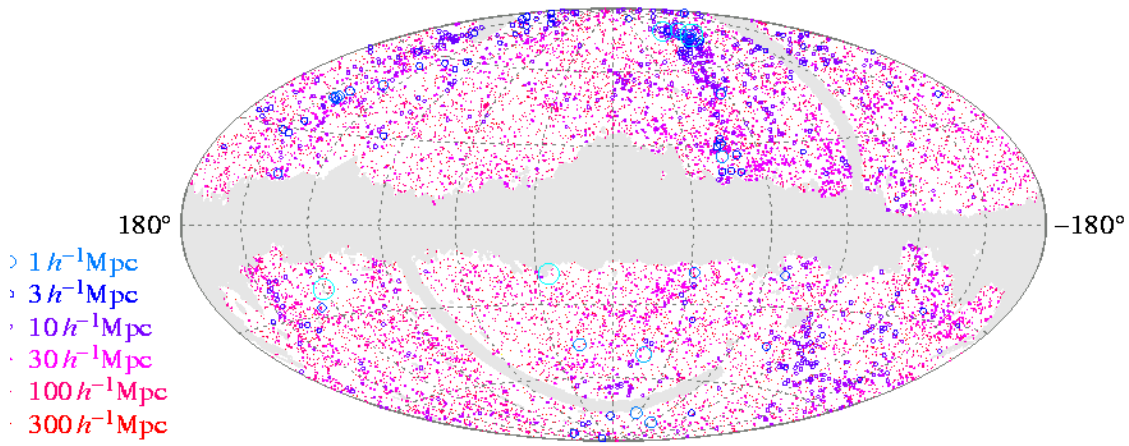

Figure 2.7: The Infrared Astronomical Satellite Point Source Catalog Redshift Survey (IRAS PSCz). A redshift survey of IRAS galaxies to 0.6 Jy and contains 15,411 galaxies over 84% of the sky. [www-ik.fzk.de]

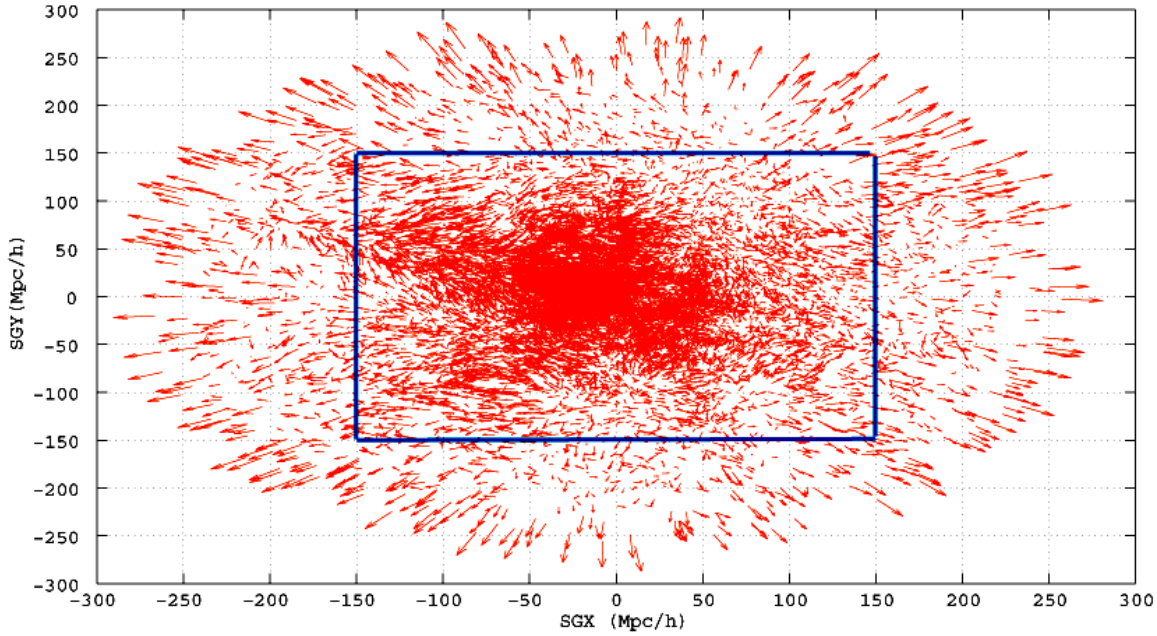

Figure 2.8: The PSCz velocity is incomplete in larger distances (> 150 Mpc/h).

sample for $\beta = 1.0$, a sample of 15,795 galaxies, which hold information about the recession velocity and redial peculiar velocity in the Local group frame and distance coordinates in the super galactic coordinates (in Mpc) (here after we represent this catalogue as B99). In the next section we discuss about the method we used to constrain the value of β, presenting our attempt to constrain β.

2.5 Constraining β using the χ^2 hypothesis test

The value of β was estimated by seeking to minimise the value of χ^2 in the equation;

$$\chi^2 = \frac{(V_{obs} - V_{pre})^2}{\sigma_{vpec}^2 + \sigma_d^2}, \tag{2.10}$$

where V_{obs} and V_{pre} are the observed and predicted peculiar velocities, respectively. The error in the peculiar velocities and the radial distance are denoted by σ_{vpec} and σ_d. The corresponding fractional distance scatter is fixed for each distance indicator [Table 2.1]. Predicted peculiar velocity fields were modelled for $\beta = 0.001$ to 1.0. The value of β, where the value of chi-square becomes a minimum, was taken to be the best-fit of β for the considered model.

The *estimated* velocity field was compared with the *observed* peculiar velocities from a range of mock catalogues designed to mimic (in size and distance indicator precision) the next generation of galaxy peculiar velocity surveys, SKA, ASKAP, WALLABY for examples. The corresponding details about the distance indicators, the number of objects and the fractional distance errors are summarized in Table 2.1. The calculations were carried out for 10,000 mock samples for each distance indicator. We discuss about the mock catalogues that designed to mimic the future redshift surveys using B99 in the following section, describing how we obtained corresponding data for V_{obs} and V_{pre}.

Table 2.1: Distance indicators

Distance indicator	Fractional distance scatter	Number of objects
Current SNIa	8%	100
Future SNIa	8%	1,000
Standard sirens	1%	100
Tully Fisher	25%	15,000

2.6 The mock data files

As we discussed in Section 2.4.4 we used the data sample for $\beta = 1.0$ produced by Branchini et al. [1999] to design the mock catalogues (i.e. B99). All of our mock survey data were restricted to lie within 150 Mpc h^{-1}, which is the distance within which the predicted PSCz velocity field is considered reliable [Branchini et al., 1999]. As we stated previously, the value of β obtained from the IRAS PSCz survey by several studies, with the v-v comparison, mostly favoured the value of $\beta_I = 0.5$ [Neill et al., 2007]. Based on this concept, we have considered our true value of β as 0.5, for all the calculations. Therefore, we obtained our true peculiar velocity field (i.e. $V_{pec,\beta=0.5}$(true)) by scaling the PSCz peculiar velocity field for $\beta = 0.5$

We assumed that each mock galaxy position was coincident with one of the PSCz galaxies for simplicity. The data to generate the observed and the predicted peculiar velocity field of the objects were taken from the smoothed PSCz density field published by Branchini et al. [1999] (i.e. B99). The mock objects are positioned randomly with the PSCz galaxies. Since the mock objects are coinciding with the PSCz galaxies, the value of the observed recession velocities cz and the true radial peculiar velocities of the PSCz galaxies are considered to be the corresponding cz_{obs} and $V_{pec,\beta=0.5}$(true) of the mock objects. Then we obtained the corresponding data as follows:

- The true radial distances (d_{true}) of the mock objects were obtained as,

$$d_{true} = cz_{obs} - V_{pec,\beta=0.5}(true). \tag{2.11}$$

- The observed radial distance (d_{obs}) and the radial peculiar velocities (V_{obs}) are estimated from these available data, where

$$d_{obs} = d_{true} + \sigma_d \tag{2.12}$$

$$V_{obs} = cz_{obs} - d_{obs}. \tag{2.13}$$

The errors in d_{obs},i.e. σ_d were modelled as Gaussian with a fixed-scatter.

- The data for predicted peculiar velocity (V_{pre}) were originally taken from B99 with $\beta = 1.0$. A fixed Gaussian scatter (σ_{vpec}) is added to V_{pre} to account for inaccuracies and model incompleteness in the PSCz reconstruction procedure.

$$V_{pre,\,\beta=1.0} = V_{pec,\beta=1.0}(PSCz) + \sigma_{vpec} \tag{2.14}$$

Then we used these data to constrain β by applying χ^2 hypothesis test and the next section focuses on the results we obtained from this method.

2.7 Results and discussion

Figures 2.9 and 2.10 illustrate the variation of the best-fit value of β with respect to the error in the peculiar velocity field (σ_{vpec}, i.e. denoted by V_s in figures) obtained for the distance indicators SNIa (current, future), TF and standard sirens (SS), respectively. Each histogram contains data for 10,000 samples with 100 bins, where the distributions are expected to be Gaussian. σ_{vpec} was varied from 50 km s^{-1} to 300 km s^{-1}, depending on the practical issues. For the smaller values of σ_{vpec}, the distribution of β-estimates centred around the value of true-β, (i.e. 0.5). This behaviour can be seen for both the distance indicators with smaller scatter (SS, SNIa) as well as with larger scatter (TF). These results confirms the high capability of B99 giving a better constraint for β even with the future surveys with the χ^2 hypothesis testing. With the increment of σ_{vpec}, the distribution of β-estimates deviate gradually from true-β, which implies that the value of β biased according to the value of σ_{vpec}. The distributions are biased for the lower values of β-estimates as σ_{vpec} is increasing.

Tabel 2.2 contains the data for the variation of the mean value of β-estimates with σ_{vpec}, of each distance indicators, where the gravitational wave standard sirens (GSS), TF, current SNIa (CSN) and future SNIa(FSN). Figure 2.11 illustrates their behaviour. The mean value corresponding to the smaller σ_{vpec} having a value closer to true β, where mean of the β-estimation showed a relatively good range in between 0.45-0.5, for the scatter range of σ_{vpec} = 0 - 150. Beyond this range the β-estimates

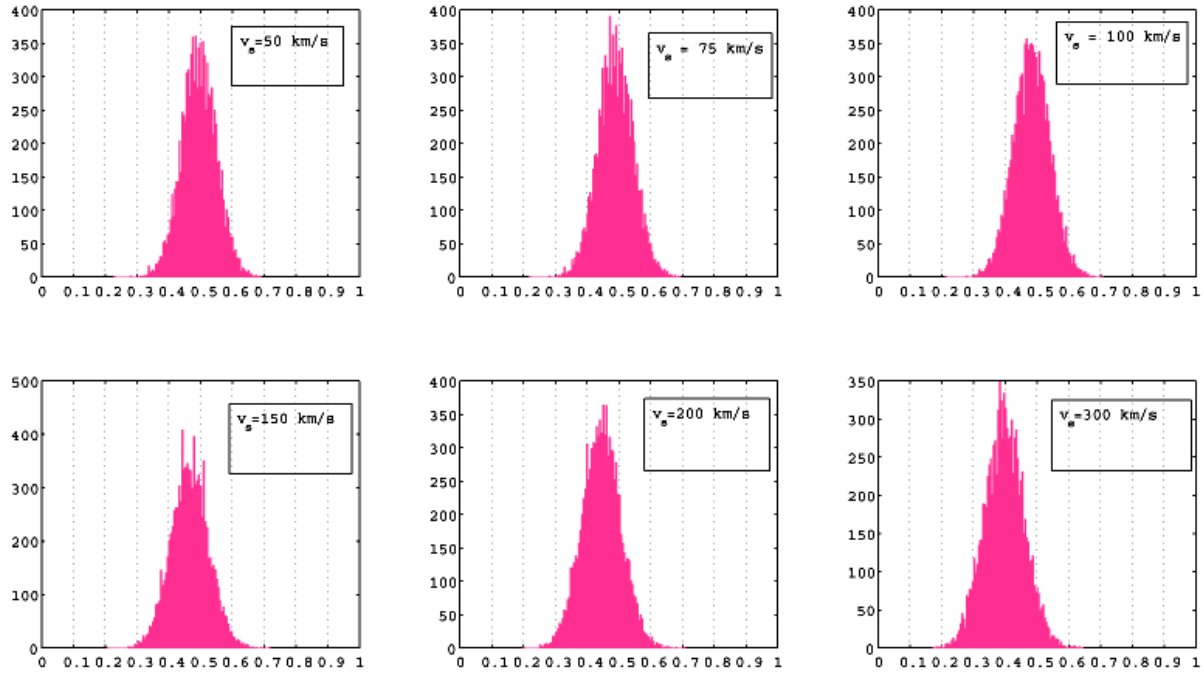

(a) Current SNIa surveys

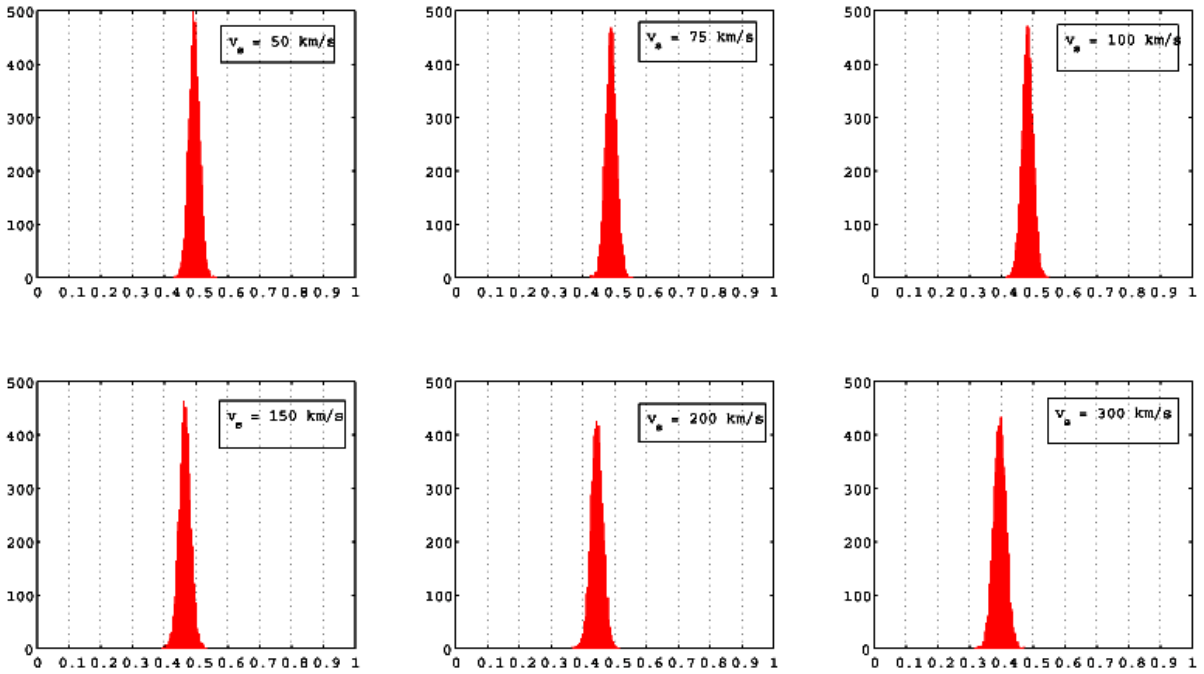

(b) Future SNIa surveys

Figure 2.9: The behaviour of β-estimates with the increment of the scatter of peculiar velocity V_s. The distance indicators are coincide with the PSCz galaxies. The simulation has carried out for 10,000 mock samples. (a) Current SNIa surveys: 100 objects with fractional distance scatter of 0.08. (b) Future SNIa surveys: The fractional distance scatter is the same (i.e. 0.08) for 1000 objects.

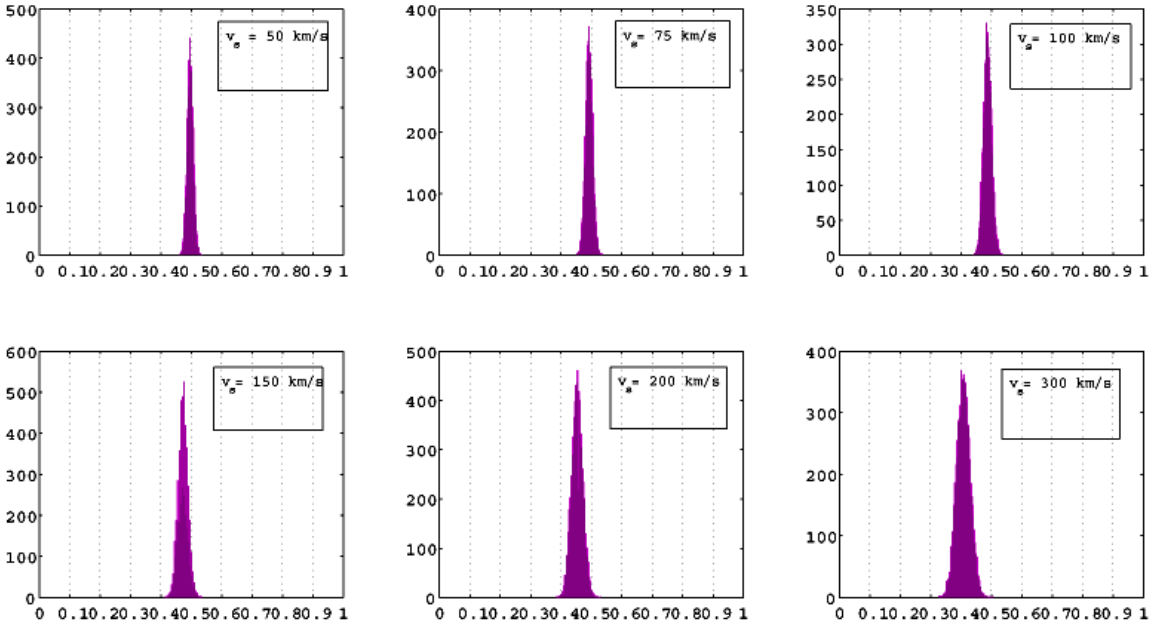

(a) Standard sirens

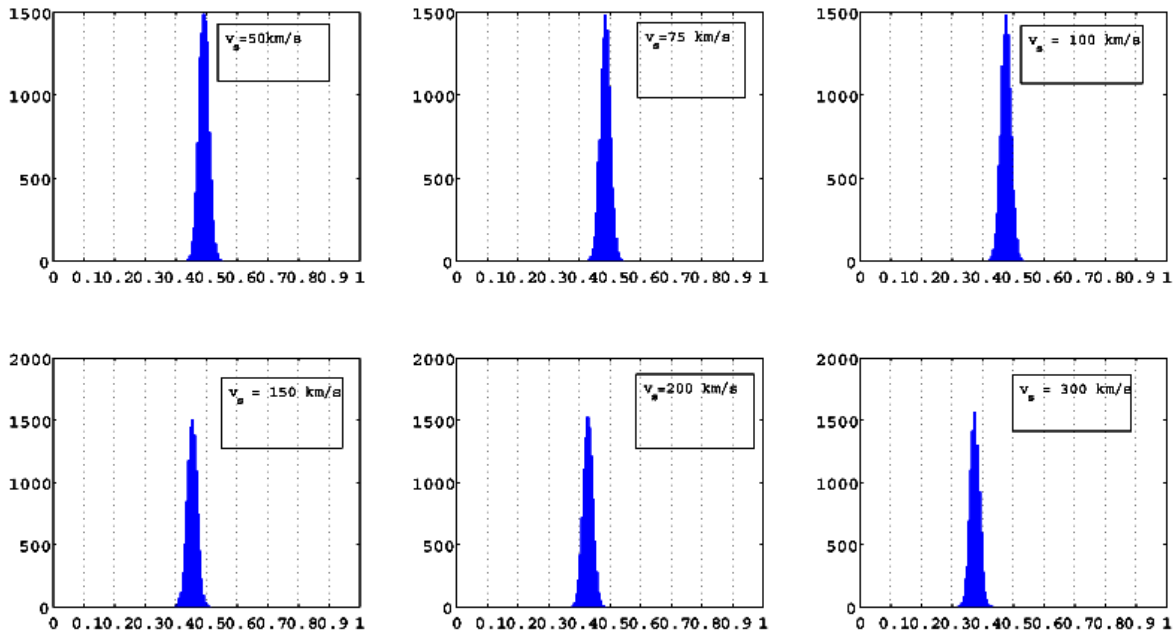

(b) Tully Fisher relation

Figure 2.10: The behaviour of β-estimates with the increment of the scatter of peculiar velocity V_s for the standard sirens and TF. The distance indicators are having the same position as the PSCz galaxies. (a) Standard sirens: The results are obtained for 100 objects with fractional distance scatter of 0.01. (b) Tully fisher relation: The fractional distance scatter is 0.25 and 10,000 objects are taking into account.

are significantly deviate from true β. Especially, the deviation occurred after of σ_{vpec} = 150 km/s. This is a good agreement with the uncertainties used in peculiar velocity fields in the current studies. From a careful analysis of predicted and observed peculiar velocities, Willick and Strauss [1998] estimated these uncertainties to be 100 km s^{-1}. Radburn-Smith et al. [2004] found reasonable χ^2 value if 150 km s^{-1} was assumed for the distance scatter. Neill et al. [2007] have considered 150 km s^{-1} uncertainty to quantify the effect of SNIa peculiar velocities on the derivation of cosmological parameters.

Table 2.2: The mean value of β-estimates with σ_{vpec}.

σ_{vpec}	GSS	TF	CSN	FSN
0	0.50±0.01	0.50±0.01	0.50±0.02	0.50±0.03
50	0.49±0.01	0.49±0.02	0.49±0.02	0.49±0.05
100	0.49±0.01	0.48±0.02	0.48±0.02	0.49±0.05
150	0.47±0.02	0.45±0.03	0.46±0.02	0.46±0.02
200	0.45±0.03	0.43±0.03	0.44±0.02	0.44±0.06
300	0.41±0.01	0.38±0.03	0.39±0.02	0.40±0.06
400	0.36±0.02	0.32±0.02	0.34±0.02	0.34±0.06
500	0.31±0.01	0.30±0.03	0.29±0.02	0.30±0.06

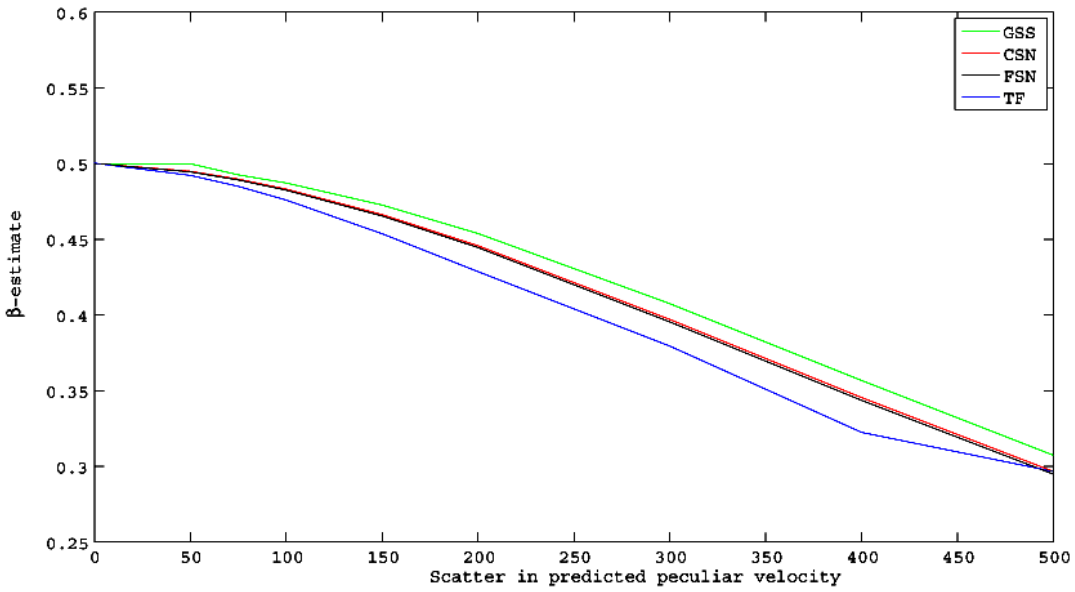

Figure 2.11: Mean of the β-estimates. The mean value of β for each distance indicators show a good agreement with the considered true β (i.e. $\beta = 0.5$) for the lower scatter in the predicted peculiar velocity.

2.8 Conclusions

Future peculiar velocity surveys should offer considerable improvement in the accuracy of β determinations - with a similar error on β of less than 1% achievable from both smaller surveys of highly accurate distance indicators (e.g. future SNIa and GW sirens) and larger surveys of less accurate distance indicators (e.g. 6dF, ASKAP, WALLABY). Estimates of β are biased by errors in the predicted peculiar velocity field reconstruction; this bias is approximately the same for all our mock data sets, but - as expected - becomes more obvious when the standard deviation of β estimates is smaller. In order to reduce this bias, improvements will be required in the predicted velocity field reconstructions as well as the observed peculiar velocities. This study implies that to improve the accuracy of β, it is not enough of having data samples with large number of objects, as β value also biased according to the velocity scatter. Hence, in order to smooth the value of β, accurate velocity reconstructions are also crucial. If we manage to minimize the error in the peculiar velocity fields $\leq$ 150 km/s, the best-fit value would be occurred between 0.45 - 0.55.

Chapter 3

The ROBUST method and next generation of redshift surveys

This chapter focuses on the ROBUST method for fitting peculiar velocity field models originally introduced by Rauzy and Hendry [2000] (hereafter RH00). We have applied this method to a range of mock catalogues designed to mimic the next generation of redshift surveys. Our aim is to analyze the robustness of the luminosity function as a distance indicator in reconstructing the peculiar velocity fields.

As we discussed in previous chapters, distance indicators have a significant influence on methods for reconstructing the peculiar velocity field. The scatter in the distance and velocity estimation is highly influential for the efficacy of velocity-velocity comparisons. We discussed this issue in Chapter 2 by applying χ^2 hypothesis testing to different types of distance indicators, with different intrinsic scatters. As we pointed out, the Malmquist bias can have a major influence on distance measurement and clear knowledge about statistical methods, which are used to correct the Malmquist bias, become very important (Hendry and Simmons [1995], Willick [1994]). The necessity of applying an appropriate statistical method for the error correction is very obvious in constraining β. Moreover we note that different values of β appear to be favoured by different reconstruction methods. The density - density comparison (i.e. POTENT) lead to a value of $\beta \simeq 1.0$, while velocity-velocity comparisons (e.g. VELMOD) appear to favour a value of $\beta \simeq 0.5$. [Willick et al., 2000]. The

exact reason for this difference still remains a mystery. The prior assumptions of the different statistical analyses may not all be represent faithfully the actual features of the spatial and velocity distributions. The main concept of RH00 is to provide a method that reduces as far as the possible number of a priori hypotheses concerning the distance indicator sample, which led to the development of the ROBUST method.

The ROBUST method uses the luminosity function of the sources as a distance indicator and this method is applicable for fitting peculiar velocity models to complete flux limited catalogues. The characteristic of the ROBUST method is that no assumptions need to be considered for the spatial distribution of sources and also about their luminosity function, apart from the assumption that the luminosity function does not depend on position. Another important feature is the applicability of the method even when there are selection effects in redshift. Explicit corrections for Malmquist bias are unnecessary with the robustness of the method. Further, the inclusion of additional observables correlated with the absolute magnitude - such as for example rotation velocity information described by the Tully-Fisher relation, as would be accessible e.g. to the proposed WALLABY surveys (see Section (1.13.8) - is straightforward.

The layout of the present chapter is as follows: in sections 3.1 and 3.2 we present the ROBUST method introduced by Rauzy and Hendry [2000], which we followed for this study. Section 3.3 describes the techniques we used to model the peculiar velocity field. Then we discuss about generating the mock catalogues by applying the ROBUST method in section 3.4. The details of the techniques we used to constrain β are included in section 3.5. In the following section, § 3.6, we present our results, where we analyse the potential of the ROBUST method in constraining β for the future redshift surveys. In Section 3.7.1 we compare the χ^2 test with the ROBUST method. Finally, the last section 3.8 gives the conclusions.

3.1 Assumptions and statistical model

The fundamental assumption made in RH00 is that the luminosity function $f(M)$, i.e. the distribution function of the absolute magnitudes M of the population, does not depend on the spatial position $\mathbf{r} = (r,l,b)$ of the galaxies, where l and b are the object's longitude and latitude. Under this assumption, the probability density of the sample can be given as;

$$dP \propto dP_r dP_M = \rho(r,l,b)\ r^2\ cosb\ dl\ db\ dr \times f(M)dM, \tag{3.1}$$

where $\rho(r,l,b)$ is the spatial distribution function of the sources.

The samples which are considered to apply the ROBUST method, have a selection function in apparent magnitude with a sharp cut-off, where $\psi(m) = \theta(m_{lim} - m)$, $\theta(x)$ the Heaviside function, i.e. the samples are complete up to a given apparent magnitude m_{lim}. With this condition for the selection effects, the probability density of the sample may be written as;

$$dP = \frac{1}{A}\ h(\mu,l,b)\ cosb\ dl\ db\ d\mu\ f(M)\ dM\ \theta(m_{lim} - m), \tag{3.2}$$

where μ is the distance modulus;

$$\mu = m - M = 5\log_{10} r + 25, \tag{3.3}$$

and A is the normalization factor which satisfies $\int dP = 1$. For convenience in notation, the angular dependence in l and b is considered to be implicit. Under these conditions the observational selection effects in apparent magnitude introduce a correlation between M and μ. The key point of the method is based on the definition given to the random variable ζ;

$$\zeta = \frac{F(M)}{F(M_{lim})}, \tag{3.4}$$

where $F(M) = \int_{-\infty}^{M} f(x)\, dx$ represents the cumulative distribution function in M and $M_{lim} = M_{lim}(\mu) = m_{lim} - \mu$ is the maximum absolute magnitude for which a galaxy at distance μ would be visible in the sample. By definition, the random variable ζ for a sampled galaxy is uniformly distributed on the interval [0,1]. The expression shown below is the volume element of the sample

$$d\mu d\zeta = \frac{f(M)}{F[M_{lim}\,(\mu)]} d\mu\ dM. \tag{3.5}$$

Hence,

$$d\mu f(M)\ dM = F[M_{lim}(\mu)]\, d\mu\, d\zeta. \tag{3.6}$$

Replacing equation (3.6) with the equation (3.2), the probability density dP can be related to ζ as follows;

$$dP = \frac{1}{A}\ h(\mu)\ F[M_{lim}(\mu)]\ d\mu \times \theta(\zeta)\ \theta(1-\zeta)\ d\zeta, \tag{3.7}$$

$$A = \int h(\mu)\ F[M_{lim}\ (\mu)] d\mu, \tag{3.8}$$

where, $dP_\mu = (1/A) \times h(\mu)\ F[M_{lim}(\mu)]\ d\mu$ describes the observed spatial distribution function of the sources. The equation (3.7) implies two important properties about ζ;

1. P1 : ζ is uniformly distributed between 0 and 1.
2. P2 : ζ and μ are statistically independent, i.e. the distribution of ζ does not depend on the spatial position of the galaxies.

Hendry et al. [2001] construct a test to calculate the completeness of the sample in apparent magnitude by using the property P1. This test is also presented in Rauzy et al. [2001]. The method introduced for fitting peculiar velocity field models (i.e. RH00) is based on the property P2, which we are using in this chapter for our analysis.

3.2 Estimate of the random variable ζ

The random variable ζ can be estimated without any prior knowledge of the cumulative luminosity function $F(M)$. With each data point with coordinates (M_i, μ_i) is associated the region $S_i = S_1 \bigcup S_2$, defined as;

$$S_1 = M \leq M_i \text{ and } \mu \leq \mu_i, \tag{3.9}$$

$$S_2 = M_i < M \leq M^i_{lim} \text{ and } \mu \leq \mu_i. \tag{3.10}$$

A survey limited by a sharp *apparent magnitude* limit will result in a diagonal truncation boundary. This kind of truncation causes problems to the standard statistical methods and a survey with a truncation of *absolute magnitude* (Figure 3.1) , rather than apparent magnitude, would remove these statistical difficulties by defining a sample that is *volume limited* [Efron and Petrosian, 1992]. Further, these influences would be negligible if the luminosity distribution is independent of redshift [Efron and Petrosian, 1992]. In this study, for each galaxy labelled i, RH00 applied a restriction $M \leq M^i_{lim}$ and $\mu \leq \mu_i$ to the samples in order to overcome the difficulties occurred due to the truncation of apparent magnitude limit. Therefore, the random variable M and μ become independent in each subsample S_i. Figure 3.1 illustrates the distribution of galaxies with the cut-off.

Hence, the number of points r_i belonging to S_1 and the number of points n_i in $S_i = S_1 \bigcup S_2$ (Figure 3.1) can be related to the cumulative luminosity function $F(M)$ as;

$$r_i \propto \int_{-\infty}^{M_i} f(M)dM = F(M_i), \tag{3.11}$$

$$S_i \propto F(M^i_{lim}). \tag{3.12}$$

Then an unbiased estimate of the random variable ζ may be written as,

$$\widehat{\zeta_i} = \frac{r_i}{n_i + 1}. \tag{3.13}$$

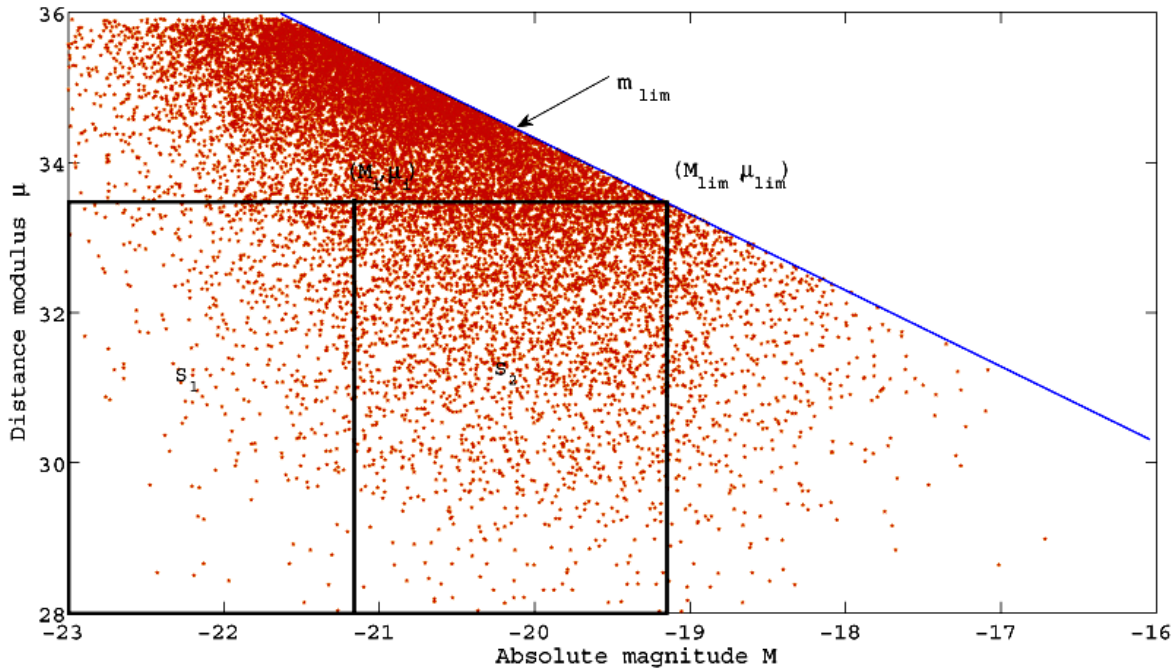

Figure 3.1: The $M - \mu$ diagram of a sample with 15,795 objects which are having the apparent magnitudes $\leq m_{lim} = 14.3187$ (see Section 3.4 for further discussion). A survey with a truncation of absolute magnitude would remove the statistical difficulties occurred due to the truncation of apparent magnitude limit. The data are generated from the method given in Section 3.4.1. Each mock object is coincident with the position of a PSCz galaxy.

The estimator $\widehat{\zeta_i}$ may be defined as the normalized rank of the point M_i, when the absolute magnitudes (M) are sorted by increasing order within the subsample S_i [Efron and Petrosian, 1992].

3.3 Radial peculiar velocity field models

Rauzy & Hendry assumed that the radial peculiar velocity field $v(r)$ can be described by an one-parameter velocity model $v_\beta(\mathrm{r})$, which means that there exists a specific value of β^* satisfying $v^*_\beta(r) = v(r)$. For a given value of the parameter β, the model-dependent variables μ_β and M_β can be computed (modulo the value of the Hubble constant H_0) from the observed redshift z and apparent magnitude m, following

$$\mu_\beta = 5 \log_{10} \frac{cz}{H_0} + 25 - u_\beta, \tag{3.14}$$

$$M_\beta = m - \mu_\beta, \tag{3.15}$$

where the quantity u_β is defined as

$$u_\beta = -5\log_{10}(1 - \frac{v_\beta}{cz}). \tag{3.16}$$

The quantities μ_β and M_β are related to the true absolute magnitude M and distance modulus μ *via*

$$\mu_\beta = \mu + u_{\beta^*} - u_\beta, \tag{3.17}$$

$$M_\beta = M - u_{\beta^*} + u_\beta. \tag{3.18}$$

The quantity ζ_β can be estimated from μ_β and M_β using equation (3.4). This may give the corresponding probability density of equation (3.7)

$$dP = \frac{1}{A}\ h(\mu)\ F[M_{lim}(\mu_\beta)]\ d\mu\ C_\beta\ \theta(\zeta_\beta)\ \theta(1-\zeta_\beta)\ d\zeta_\beta, \tag{3.19}$$

where C_β takes the following form when $(u_{\beta^*} - u_\beta) \ll 1$ [or equivalently $(v_{\beta^*} - v_\beta) \ll cz$]:

$$C_\beta = \frac{f(M)}{f(M_\beta)}\ \simeq 1 + (u_\beta - u_{\beta^*})(\ln\ f)'(M_\beta). \tag{3.20}$$

The absolute magnitude M_β has a correlation with the random variable ζ_β. Hence, $(lnf)'(M_\beta)$, a function of M_β, has a correlation with ζ_β. Under these circumstances, C_β can be represented as the correlation coefficient between ζ_β and the proposed velocity field model u_β when $\beta \neq \beta^*$. This fact implies that these quantities become statistically independent when $\beta = \beta^*$, which follows from the property P2, that $\zeta_\beta \equiv \zeta$ does not depend on the spatial position of galaxies and therefore on any function $u_\beta(\mathbf{r})$. An important conclusion can be obtained from this relation, that any statistical test of independence between ζ_β and u_β provides an unbiased estimate of the value of β^*, i.e.

$$\beta = \beta^* \Leftrightarrow \rho(\zeta_\beta, u_\beta) = 0. \tag{3.21}$$

Equation (3.20) indicates that the accuracy of this estimator is related to the amplitude of the correlation between $(\ln f)'(M_\beta)$ and ζ_β. If the dispersion of the luminosity function $f(M)$ is very small (i.e. steeper $(\ln f)'$), the estimation of the redshift param-

eter β may be more accurate. The Monte Carlo simulations can be used to analyze the influence of sampling fluctuations on the coefficient of correlation $\rho(\zeta_\beta, u_\beta)$. If the fluctuation of $\rho(\zeta_\beta, u_\beta)$ shows a linear dependence on β over a small interval, then the exact value of β which satisfies the condition (3.21), given two trial values of β that display small negative and positive correlation respectively, as follows;

$$\beta = x^i_\beta + \frac{1}{m_{grad}} \, (0 - y^i_{\rho(\zeta_\beta, u_\beta)}), \tag{3.22}$$

where $y^i_{\rho(\zeta_\beta, u_\beta)}$ should be *negative* and $y^{(i+1)}_{\rho(\zeta_\beta, u_\beta)}$ should be *positive*. x^i_β is the corresponding β value of the coordinate $(x^i_\beta, y^i_{\rho(\zeta_\beta, u_\beta)})$ and m_{grad} is the gradient of the linear curve.

A small-scale velocity dispersion (say amplitude σ_v) may cause a spurious correlation between μ_β and M_β as shown in equations (3.17) and (3.18). Hence, a correlation may occur between the variables μ_β and ζ_β. However, RH00 is only focused on the correlation between the velocity model u_β and ζ_β. Further, a correlation should not exist between the random velocity noise and u_β. Therefore, the presence of a small-scale velocity dispersion is not expected to bias the estimator proposed in equation (3.21) considerably, at least as long as the variations of the quantity u_β (r) are smooth at the scale σ_v.

The approach of the random variable ζ implies that an unbiased estimate of the parameter β has indeed been obtained using a null-correlation technique. Null-correlation approaches are characterized, in general, by their robustness, i.e. some of the functions entering the statistical model are not required to be fully specified (Bigot et al. [1991]; Triay et al. [1994]; Rauzy [1997]). The method described in RH00 does not require any priori assumptions about a specific shape of the luminosity function and the spatial distribution of the sources like the maximum likelihood methods. Also, homogeneous as well as inhomogeneous Malmquist biases are automatically accounted for applying the method. In addition, according to the equation (3.19) the selection effects in distance or redshift are allowed, in any extra terms

of the form $\psi(\mu, u_\beta)$. The next section presents the details about generating mock catalogues using the method we discussed above.

3.4 The mock data catalogues

We have applied this method to a range of mock catalogues designed to mimic the next generation of redshift surveys. The mock data sets were generated using the spatial distribution and the peculiar velocity field model defined by the IRAS PSCz velocity field data published by Branchini et al. [1999] (i.e. B99). B99 is based on the 0.6 Jy redshift survey of IRAS galaxies [Saunders et al., 1999] with a flux limit of $f_{60} = 60\,\mu$ m. Following RH00, we adopt a sharp, faint apparent magnitude limit of $m_{lim} = 14.3187$, which those authors identified as the magnitude limit corresponding to the flux limit at $60\,\mu$ m of the IRAS 1.2 Jy redshift survey. One might argue that a different limit would be more appropriate for the PSCz survey, given the larger number of galaxies in the PSCz survey compared with the 1.2 Jy redshift survey from which it was developed. However, for simplicity we do not compute an explicit new apparent magnitude limit here since the choice of apparent magnitude limit has no direct impact on our results (See Figure 3.2 for an example). The calculations are carried out considering the value of the Hubble constant $H_0 = 100$ Mpc h^{-1}, and the true value of β assumed to be 0.5. In the next section we present the details of constructing the mock data catalogues that mimic the future redshift surveys.

3.4.1 Constructing the mock data catalogue

For simplicity, we assumed that each mock galaxy position was coincident with one of the PSCz galaxies. The mock objects are randomly selected from B99. The observed recession velocity, cz, and the radial peculiar velocity, $V(r)$, which are required to find the distance modulus of the mock objects (see Section 3.3 for the corresponding equations), were taken directly from B99. The original data of the radial peculiar velocities were scaled to $V(r) = V(r)_{\beta=0.5}$, where the true value of β was considered to be 0.5 (i.e. $\beta_{true} = 0.5$). The coefficient of correlation between the random variable ζ_β and the velocity modulus u_β for $\beta_{true} = 1.0$ is illustrated in figure 3.3.

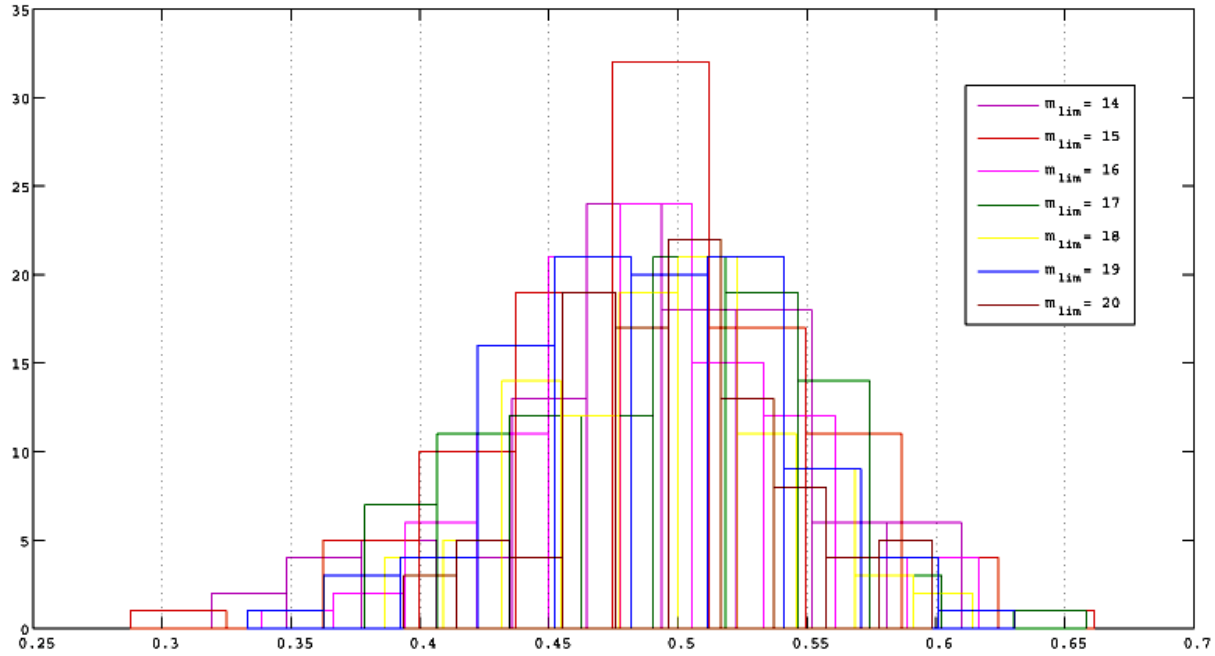

Figure 3.2: This is an example to show that the choice of the apparent magnitude limit (m_{lim}) has no direct impact for the results. We generated 1000 mock data catalogues with 5000 objects, varying the m_{lim} from 14.0 up to 20.0. An error of $\sigma = 1$ has been considered for the luminosity function. All the distributions are centered around β_{true} well, confirming our argument.

The absolute magnitude was found by considering the luminosity function to be a Gaussian distribution of mean, $\overline{M}$ = -20.0 and σ_M = 1.0 (We have used $\overline{M}$ as the mean, because μ denotes the distance modulus).

With the corresponding data in hand, we have generated the apparent magnitude of the mock objects to be lie within the m_{lim} (i.e. 14.3187). Figure 3.4 is an comparison of the distributions of the apparent magnitude of the mock objects before (blue) and after (red) the cut-off and Figure 3.1 is the $M - \mu$ diagram of the mock objects which lie within the cut-off. The mock objects are generated as satisfying the condition $cz \leq$ 15,000 km s^{-1}, where the PSCz velocity field is incomplete beyond this boundary [Branchini et al., 1999]. The method was applied to sub samples selected from the PSCz catalogue containing 5,000, 6,000 to 15,000 objects, representing the luminosity function of the mock objects as distance indicators, with an error of $\sigma = 1.0$.

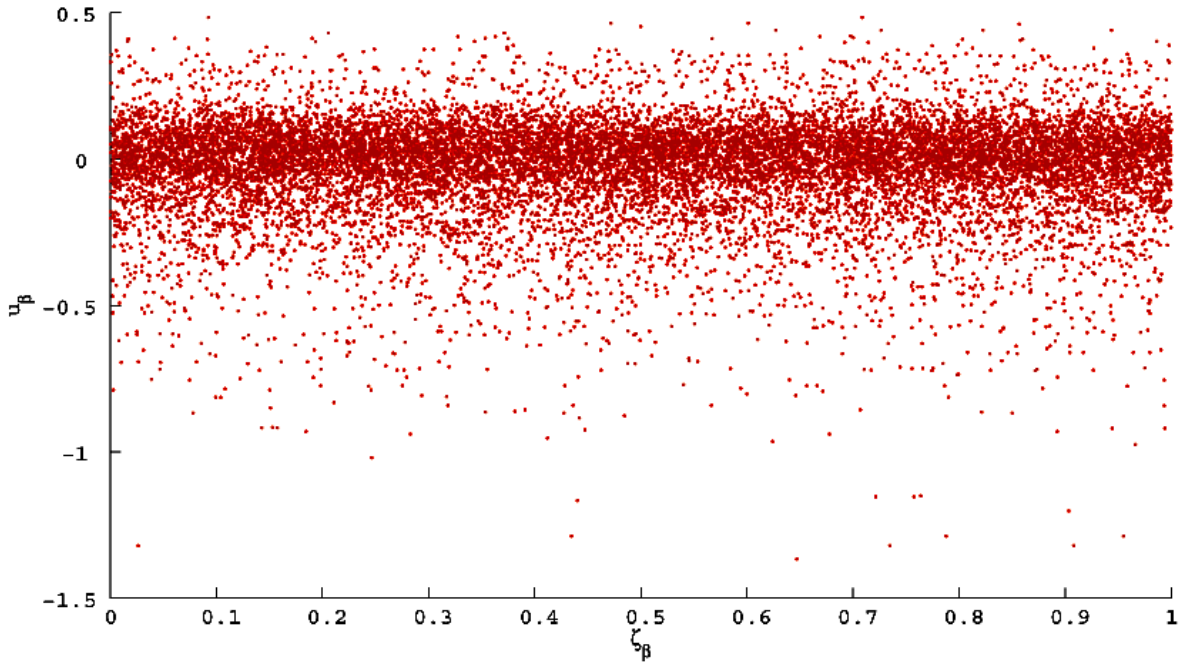

Figure 3.3: The correlation between ζ_β and $u_\beta = -5\log_{10}(1 - \frac{v_\beta}{cz})$ for $\beta_{true} = 1.0$. The coefficient of correlation is $\rho(\zeta_\beta, u_\beta) = -0.0005$ in this case. The mock sample contains 15,000 objects.

3.5 Reconstructing β with ROBUST method

After generating the mock data samples for M, m and μ we have applied the equation (3.13) to calculate the value of ζ_β for each galaxy in the mock sample. The values of u_β, μ_β and M_β are modelled from the equations (3.14), (3.15) and (3.16) for the trial values of β from 0 to 1.0 with a increment of 0.1 in each step. Then, the corresponding values of ζ_β are calculated for the each mock object. The coefficient of correlation, $\rho(\zeta_\beta, u_\beta)$ was found from the equation given below.

$$\rho(\zeta_\beta, u_\beta) = \frac{n\sum_{i=1}^{n}\zeta_i u_i - \sum_{i=1}^{n}\zeta_i \sum_{i=1}^{n} u_i}{\sqrt{n\sum_{i=1}^{n}\zeta_i^2 - (\sum_{i=1}^{n}\zeta_i)^2}\sqrt{n\sum_{i=1}^{n}u_i^2 - (\sum_{i=1}^{n}u_i)^2}}. \tag{3.23}$$

The crucial point is the determination of the corresponding β value, where ζ_β and u_β become independent each other. We have applied the linear interpolation method with the Monte Carlo simulations to determine the exact value of β which satisfies the condition in the equation (3.21). In order to apply the linear interpolation method, the linearity of the graph of $\rho(\zeta_\beta, u_\beta)$ versus β - trial is crucial, especially in small intervals of β. We have analyzed the linearity property for each and every sample and the condition is satisfied for all the mock samples. Figure 3.5 illustrates the

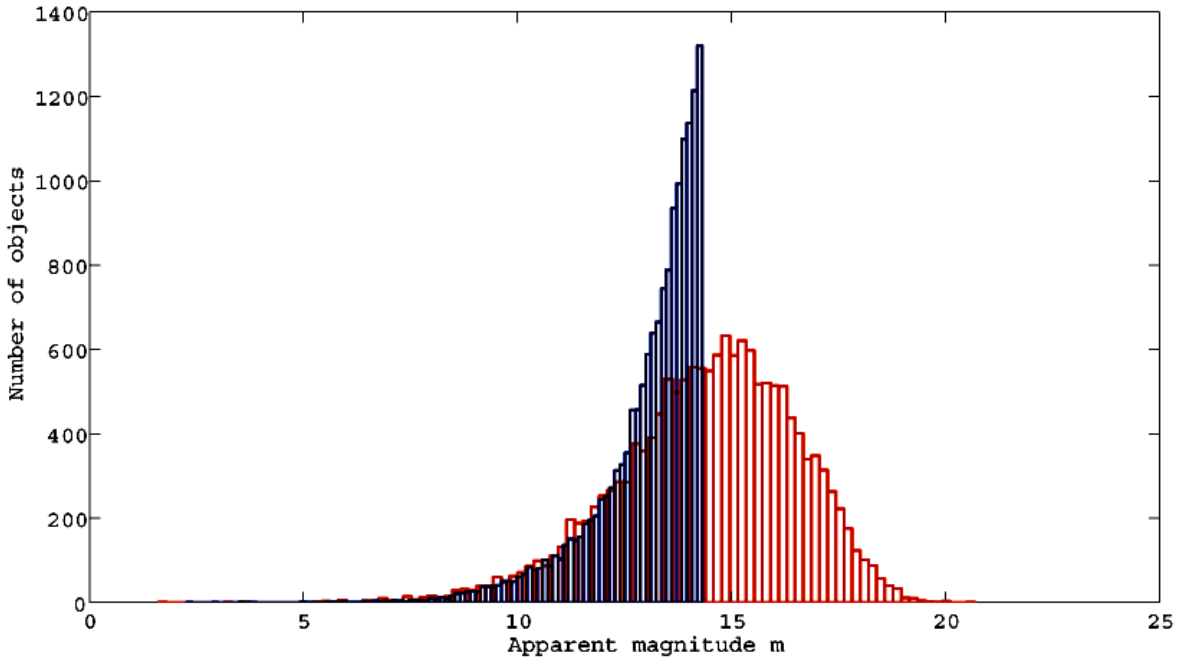

Figure 3.4: Comparison of the distribution of the apparent magnitude (m) before (blue) and after (red) applying the cut-off. The distribution without considering the m_{lim} having a gaussian distribution, while the distribution which represents the mock objects having apparent magnitude (m) $\leq m_{lim}$ displays a completely different statistical distribution. The values of the apparent magnitude with the Gaussian distribution were generated by considering a luminosity function with a Gaussian distribution of mean, $\overline{M}$ = -20.0 and σ_M = 1.0.

behaviour of $\rho(\zeta_\beta, u_\beta)$ versus β - trial for one example of each size of mock sample.

3.6 Results and discussion

3.6.1 Linear interpolation with ROBUST method

We have identified an important issue when applying the linear interpolation to determine best-fit values of β. Whether the $\rho(\zeta_\beta, u_\beta)$ versus β - trial curve is linear in the small intervals of β-trials, we have to be more careful when considering the grid point of β. For the very small fluctuations in β, ζ fluctuates very rapidly. Figure 3.6 shows the fluctuation of $\rho(\zeta_\beta, u_\beta)$ corresponding to small changes in β parameter. $\rho(\zeta_\beta, u_\beta)$ shows a considerably high fluctuation as a result of the variations in ζ - as very small numbers of galaxies move in and out of the S1 and S2 regions, while changing β very slightly. The size of the variations in $\rho(\zeta_\beta, u_\beta)$ are very small; particularly when $\rho(\zeta_\beta, u_\beta)$ is very close to zero then even a tiny variation in $\rho(\zeta_\beta, u_\beta)$ can change it from being positive to negative. This suggested to us that using linear

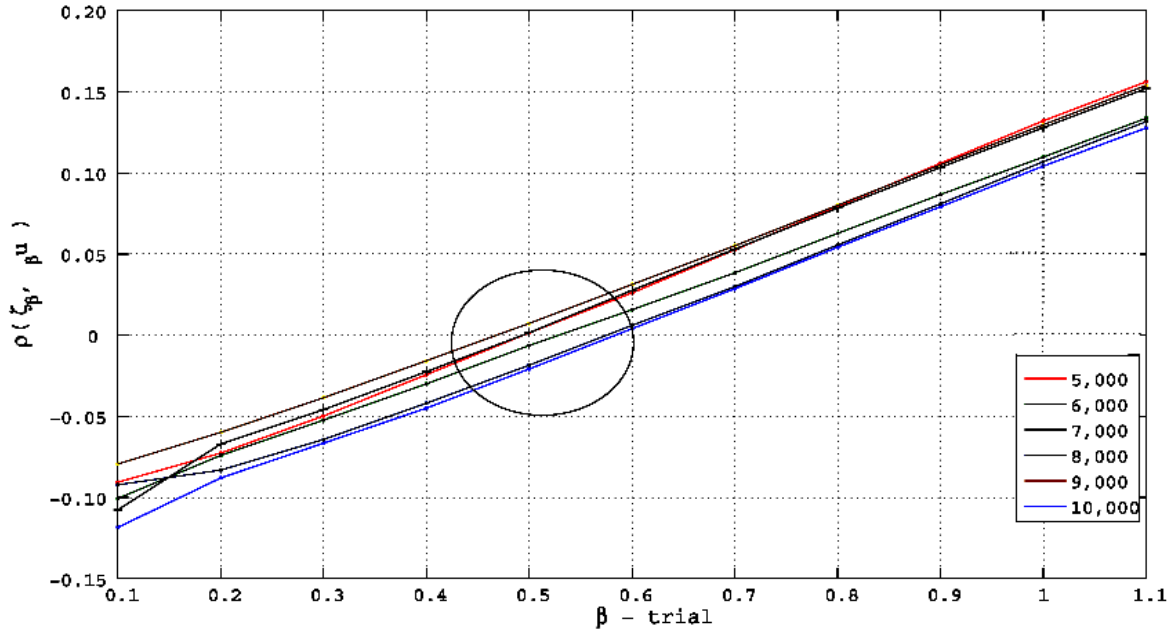

(a)

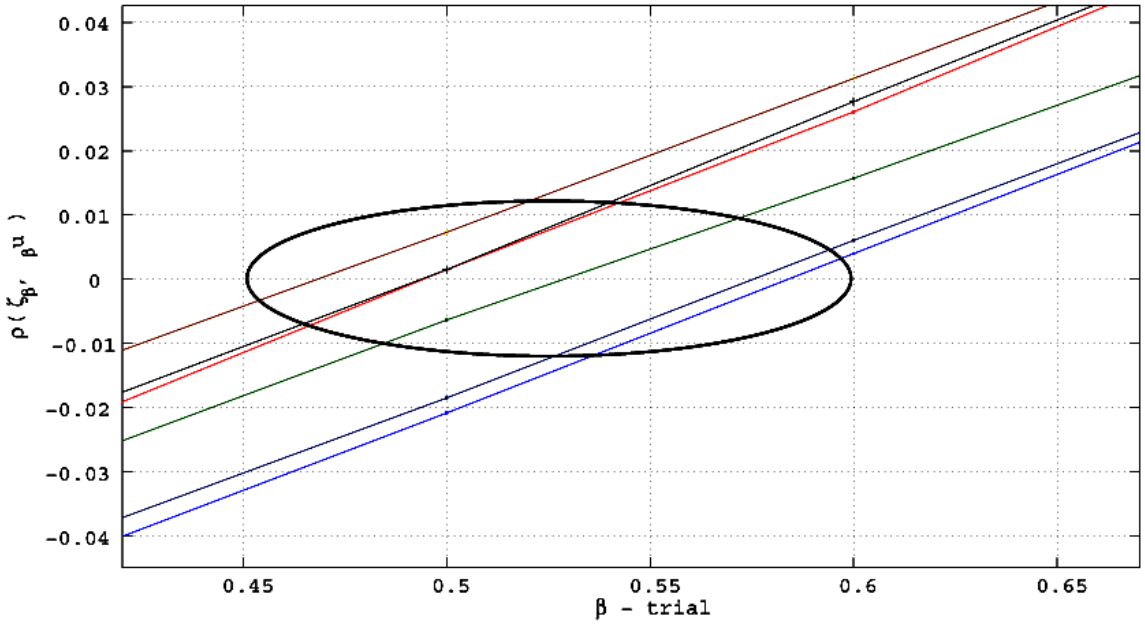

(b)

Figure 3.5: Coefficient of correlation as a function of β. The data are sampled assuming β_{true}= 0.5. (a) An illustration of all the mock samples. The best-fit value can be determined considering the interchange of the curve with $\rho(\zeta_\beta, u_\beta) = 0$. (b) The zoomed image of (a), which shows the linearity of the curve in small intervals of β.

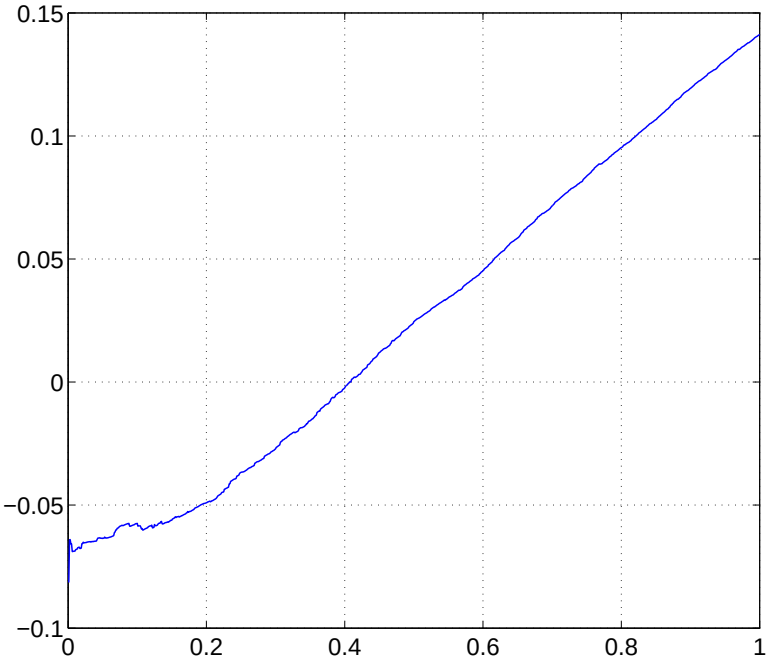

(a)

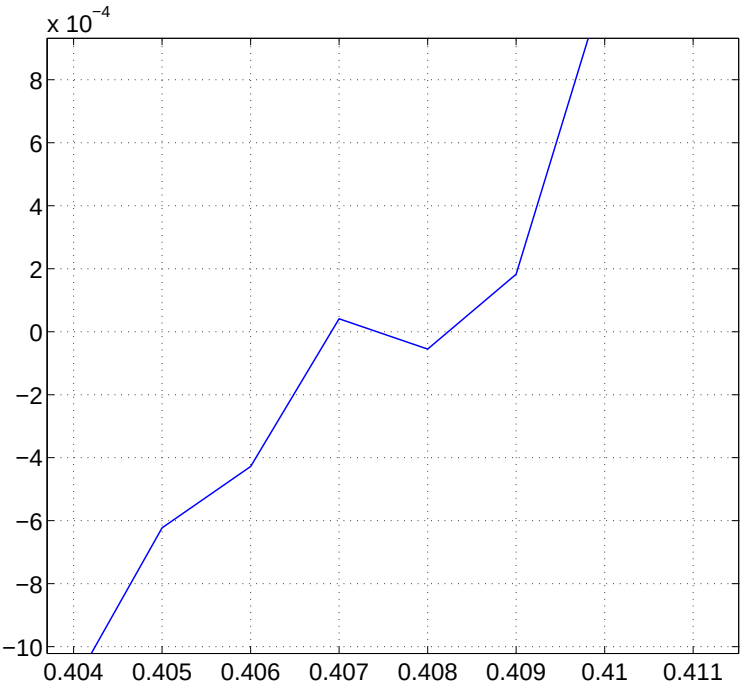

(b)

Figure 3.6: The fluctuation of $\rho(\zeta_\beta, u_\beta)$ corresponding to small changes in β parameter. The size of the variations in $\rho(\zeta_\beta, u_\beta)$ are very small; particularly when $\rho(\zeta_\beta, u_\beta)$ is very close to zero then even a tiny variation in $\rho(\zeta_\beta, u_\beta)$ can change it from being positive to negative.(a) An illustration of the fluctuation of $\rho(\zeta_\beta, u_\beta)$ for a sample with 5000 objects. The value of β is in the range 0 to 1 with 1000 grid points (i.e. $\delta\beta = 0.001$). The influence for the sign of $\rho(\zeta_\beta, u_\beta)$ due to tiny variation can be seen clearly in (b), the zoomed figure of (a).

interpolation to find where $\rho(\zeta_\beta, u_\beta)$ equals zero is not only justified, and actually better than using a very fine grid of β values. What one wants to do is to fit the $\rho(\zeta_\beta, u_\beta) = 0$ value of β from the underlying smooth trend, not the $\rho(\zeta_\beta, u_\beta)$ values with the additional random noise added due to the impact of small fluctuations in ζ and u_β. So by linearly interpolating between β values that give $\rho(\zeta_\beta, u_\beta)$ *not* too close to zero (and so less severely affected by the noise) we can get a more reliable answer for the $\rho(\zeta_\beta, u_\beta) = 0$ value for the underlying trend curve. Therefore, we have to restrict our analysis with small number of grid for β values in order to get the accurate results. Based on this issue, we considered only 10 grid point for β - parameters with $\delta\beta = 0.1$.

3.6.2 Constraining β

As we discussed earlier, our aim is to identify the corresponding value of β - trial, where ζ_β and u_β become independent from each other (i.e. $\rho(\zeta_\beta, u_\beta) = 0$). This value would be the best-fit for the peculiar velocity model. The best-fit values for each sample, which are obtained from the linear interpolation, have a considerable agreement with the true value of β (i.e. 0.5). Figure 3.7 illustrates the results of β estimates for a luminosity function with $\sigma = 1.0$. The distribution of the best-fit values of β are centered around 0.5, giving a good agreement with the true value of $\beta = 0.5$. Further, the distribution become narrower with increasing of the number of objects. From left to right, in each raw, number of objects are increasing from 5,000 to 15,000. These results confirm the potential of the ROBUST method as a method of modeling peculiar velocity fields. More importantly, whether the luminosity function of the objects have a considerably high scatter, ROBUST may provide more accurate values in β determination.

3.6.3 Scatter in the luminosity function and the ROBUST method

We have varied the scatter in the luminosity function from $\sigma = 1.0$, 1.5 and 2.0, when generating the absolute magnitude of the mock objects. The distributions of

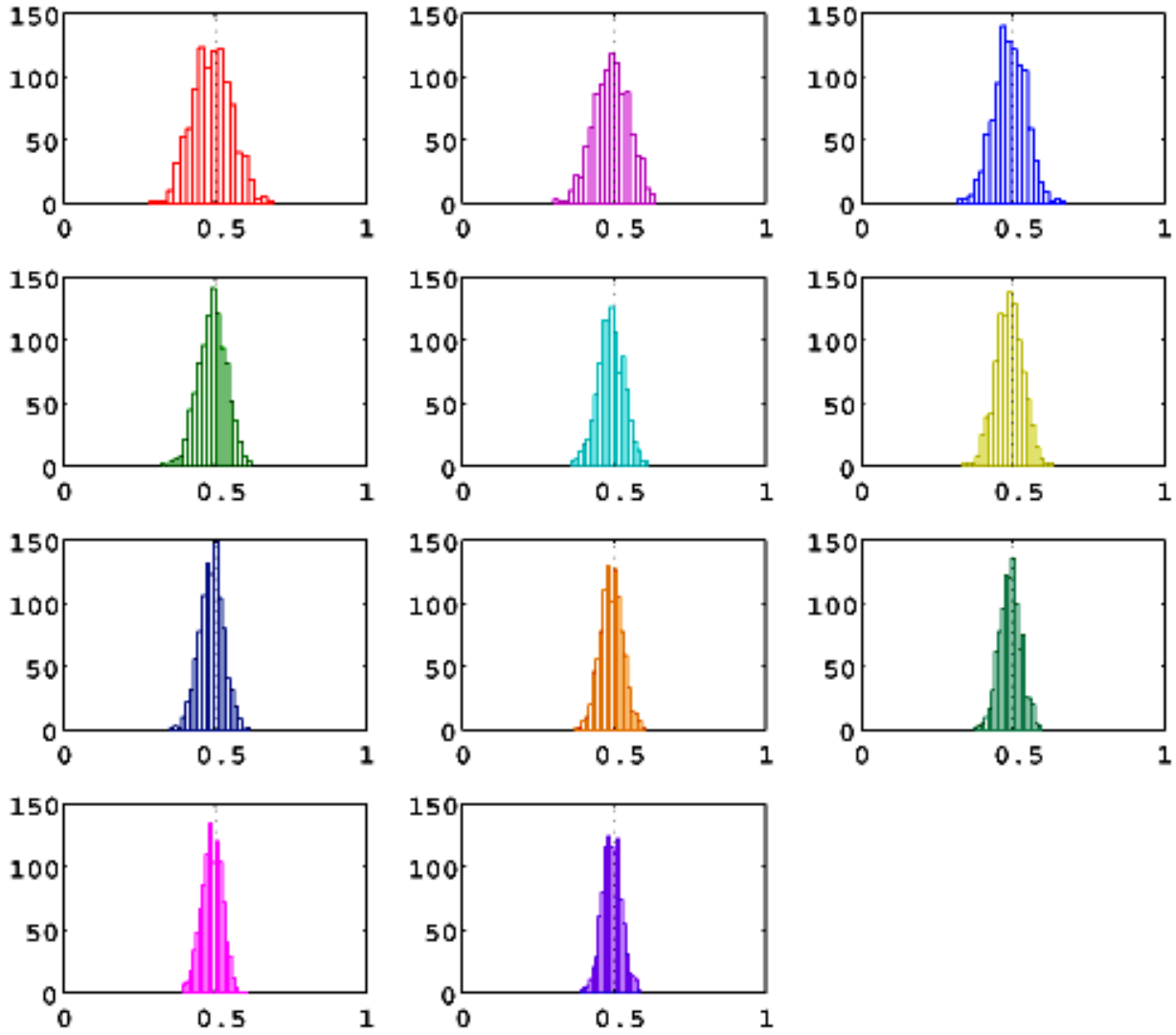

Figure 3.7: The distribution of the best-fit value of β - trial. The ROBUST method was applied for 1000 mock samples with 5,000, 6,000 to 15,000 mock objects, respectively. The distributions are centered around 0.5 for the best estimates. The error in the luminosity function considered to be $\sigma = 1.0$.

the best-fit of β are shown in figures 3.8 and 3.9. The distribution of beta estimates become wider with the increase of the luminosity function scatter. Note, however, that all of the distributions are centred around the true value of $\beta = 0.5$.

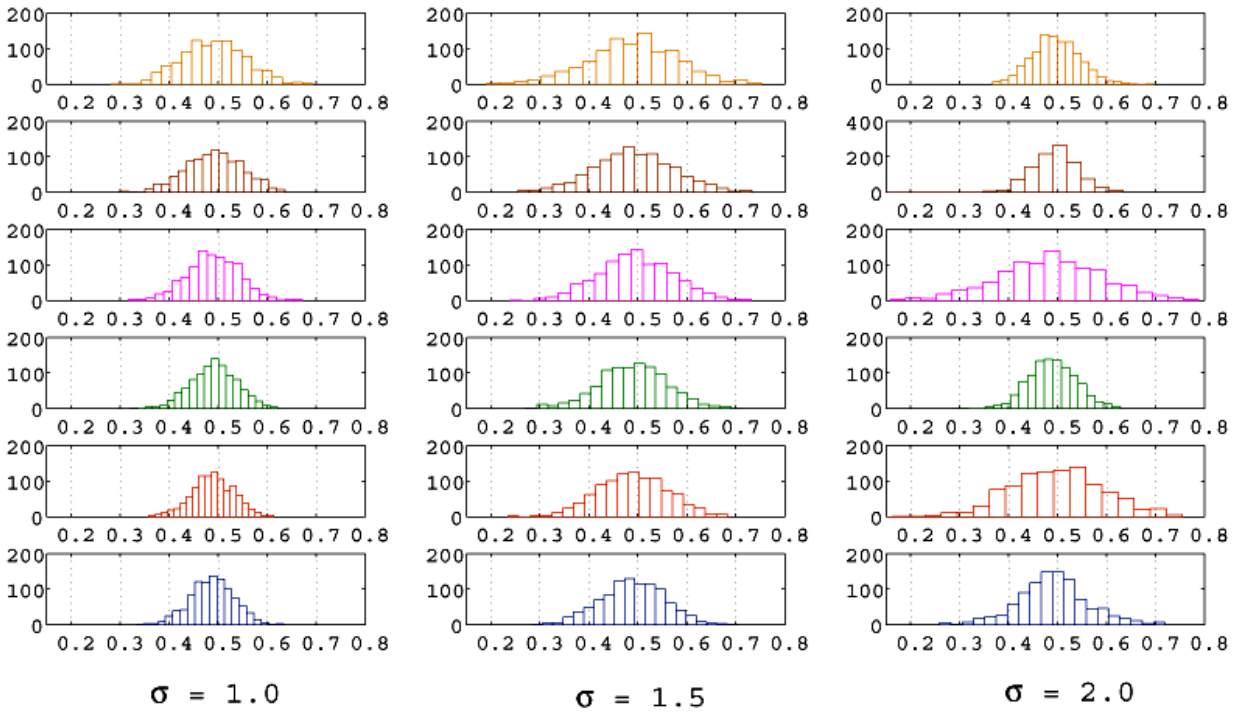

Figure 3.8: The influence of the scatter in luminosity function in constraining β, using the ROBUST method. The rows from top to bottom represent the samples with number of objects 5,000, 6,000 to 10,000. The columns from right left denote the considered error (σ) in the luminosity function.

3.7 A comparison of the χ^2 techniques with the ROBUST method

In this section we discuss about the potential of the above two methods in constraining β under different circumstances given below;

- The usefulness of the χ^2 hypothesis test with the ROBUST method, to TF-like distance indicators.
- Type Ia supernovae versus the galaxy luminosity function.
- A luminosity function with a Uniform distribution.

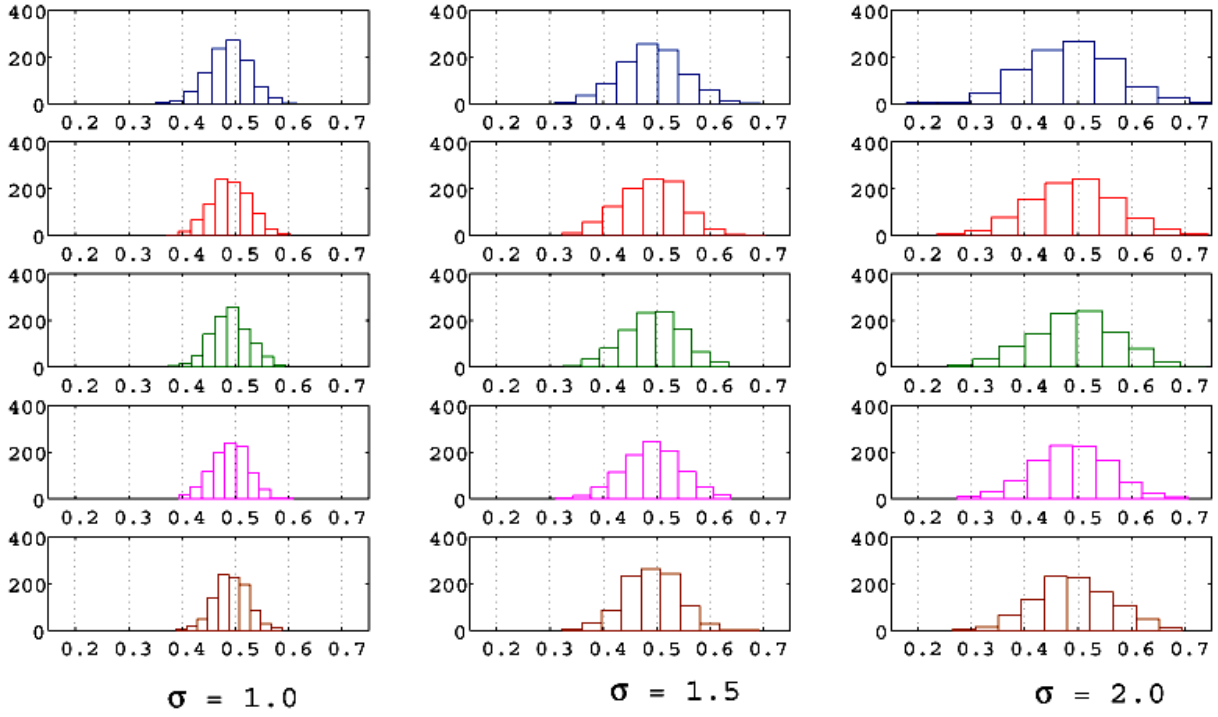

Figure 3.9: The influence of the scatter in luminosity function in constraining β, using the ROBUST method, continued. The rows from top to bottom represent the samples with number of objects 11,000, 12,000 to 15,000. The columns from right left denote the considered error (σ) in the luminosity function.

3.7.1 The usefulness of the χ^2 hypothesis test with the ROBUST method, to TF-like distance indicators

For this analysis we considered the TF-like distance indicators. Our aim was to compare the usefulness of the χ^2 hypothesis test with the TF-like distance indicators and the ROBUST method with a LF of $\sigma = 1.0$, to analyse a sample with large number of galaxies. The corresponding data for the χ^2 test were obtained from the method described in Section 2.6. The fixed fractional distance scatter of TF was taken to be 0.25, same as before. We considered only the samples with 50 km s^{-1} (the smallest scatter considered for this study) and 150 km s^{-1} (a commonly used velocity scatter in present day studies) as the velocity scatters with a gaussian distribution. The data for the ROBUST method were obtained by using the method explained in sections 3.4 and 3.5. The error in the LF was considered to be 1.0. Figure 3.10 is an illustration of the results we obtained.

The top row (green, $\sigma = 1.0$) contains results obtained from the ROBUST method, while the middle row (red, $\sigma_V = 50$ km s^{-1}) and the bottom row (violet, $\sigma_V = 150$ km

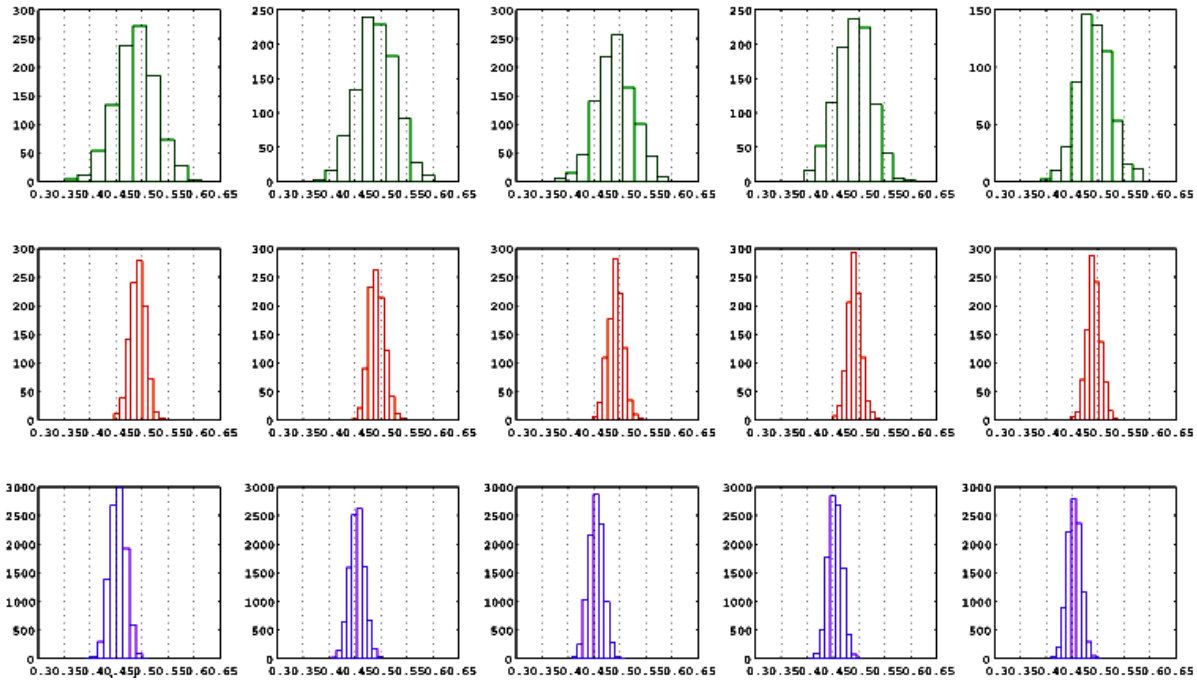

Figure 3.10: The β estimates obtained for TF-like indicators with the χ^2 techniques and for the ROBUST method are shown in this figure. The number of objects was varied from 11000, 12000 to 15000 and 1000 mock samples were considered. The error in the luminosity function is 1.0. For the comparison, we considered the results obtained for the samples with $\sigma_V = 50$ km s^{-1} (the smallest scatter considered for this study) and $\sigma_V = 150$ km s^{-1} (the commonly used peculiar velocity scatter in present studies), using χ^2 hypothesis test. The fractional distance scatter of TF is $\sigma = 0.25$. Gaussian errors are added to the distances and the peculiar velocities to represent the uncertainties.

s^{-1}) represent the results obtained from χ^2 test for the TF. As shown in Figure 3.10, for the results obtained from χ^2 technique, the distributions of the β-estimates are centered around $\beta_{true} = 0.5$. Also, it can be seen that the β-estimates mostly occurred in a range of about $0.4 - 0.55$. On the other, the distribution of the β-estimates obtained from the ROBUST method are in a range of about 0.35 - 0.6, a considerably wider range compared to the above range. Depending on these results we can say that the χ^2 results, with $\sigma_d = 0.25$, are better than using the ROBUST method (with an error of LF $\sigma = 1.0$). This can be explained as follows.

One of the reasons is that the χ^2 distribution describes the sum of the squares of Gaussian distributed random variables, and if the peculiar velocity errors are Gaussian then the χ^2 value that construct for each mock data set is the sum of squared Gaussians. The second reason is that the same number of galaxies and the same spatial distribution have been considered for the ROBUST method and the χ^2 test for the calculations. This means that the question of whether the TF or galaxy LF data give the more accurate β estimate will just depend on whether the LF data (with σ = 1.0) effectively give distance errors with a smaller or larger scatter than the TF data. We know that the error in the natural logarithm of distance is approximately equal to the fractional error in the distance, i.e.

$$\sigma(\ln D_{est}) = \sigma(D_{est})/D_{est} \tag{3.24}$$

Also,

$$\ln(D_{est}) = \ln(10) \times \log_{10}(D_{est}) = \ln(10) \times 0.2 \times (m_{obs} - M_{est} - 25) \tag{3.25}$$

it follows that $\sigma(\ln D_{est}) = 0.2 \times \ln(10) \times \sigma(M)$. Therefore, for the TF data $\sigma(D_{est})/D_{est} = 0.25$, while for the ROBUST data using the LF, the equivalent value is $\sigma(D_{est}/D_{est}) = 0.46$. Hence, the TF data, using χ^2 test, should provide a more accurate estimate of β anyway because they are using a smaller effective value of σ for the distance estimates by about a factor of two.

3.7.2 Type Ia supernovae versus the galaxy luminosity function.

In this section we compare the β-estimates of SNIa obtained from χ^2 test with that of obtained from ROBUST method. We assigned a fractional distance scatter of 0.08 for SNIa and the luminosity function (LF) considered to be having $\sigma = 1.0$. The same methods given in the above section were used to obtain the required data. For the comparison, 1000 mock samples with 100 SNIa were considered. The Gaussian errors were applied for the peculiar velocities with the scatter varied form 50 km s^{-1} up to 300 km s^{-1}. The 1000 mock samples with 5,000 to 15,000 objects were considered for the ROBUST method. The results can be seen in Figure 3.11.

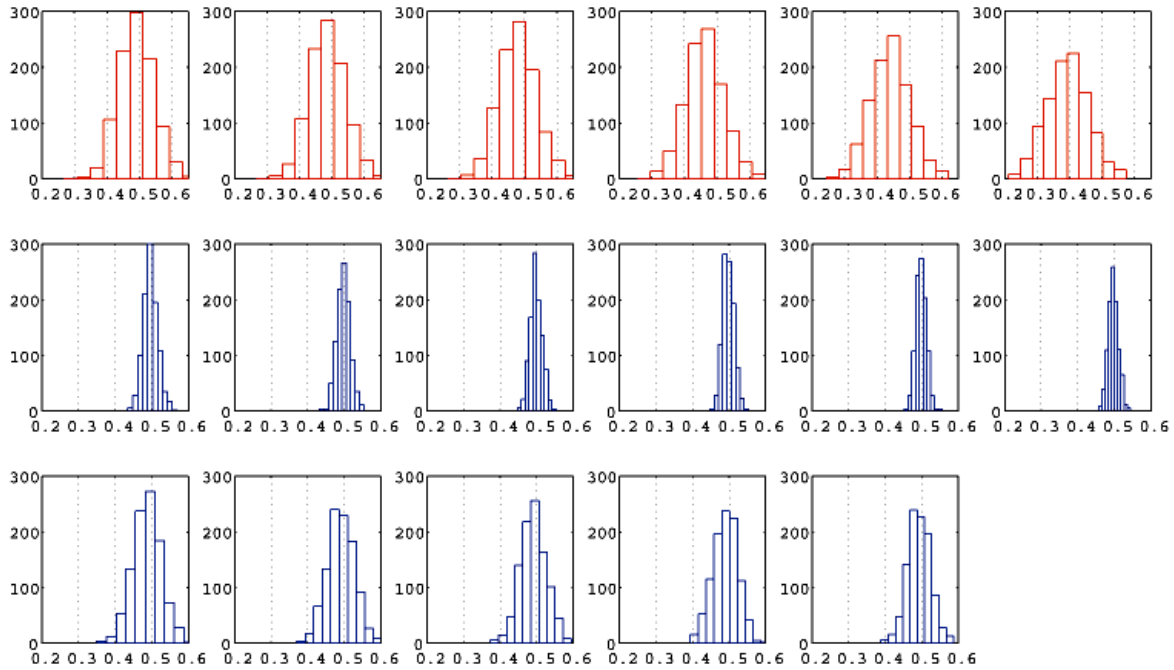

Figure 3.11: The comparison of SNIa with the galaxy luminosity function. The top row (red) denotes the results for SNIa obtained from χ^2 test. The results obtained from the ROBUST method are given in the bottom two rows with 5000, 6000 to 15000 objects. We considered 1000 mock samples for each case. For 100 SNIa, the fractional distance scatter considered to be 0.08. From left to right in the top row, the scatter in the peculiar velocity is varied from 50 km s^{-1} to 300 km s^{-1}. Gaussian errors are added to the distances and the peculiar velocities to represent the uncertainties.

The top raw represents the results obtained for SNIa (red) with 100 objects in each sample. The bottom two rows contain the results obtained form the ROBUST method. The β-estimations are in a range of 0.20 - 0.65 for SNIa while the range for

ROBUST method is 0.35 - 0.60, which is a good range compared to SNIa. Moreover, the distriutions are gradually deviates from true β (i.e. 0.5) with the increment of σ_V for SNIa. These results imply that even though the Supernovae are more accurate - one can get equally good or even better estimates of β using the galaxy LF provided one has enough galaxies. Further, we do not need to assume a specific parametric form for the galaxy LF, whereas to apply the χ^2 test with the larger data set we need to assume a Gaussian distribution.

3.7.3 A luminosity function with a Uniform distribution

For this comparison we have taken a different statistical distribution for the galaxy luminosity function, the Uniform distribution. To generate the absolute magnitude we adopted a uniform distribution where, $M = U(-23.0, -17.0)$, assuming that galaxies have a mean absolute magnitude , $M_o = -20.0$. The true value of the β was considered to be 0.5.

The procedure of generating mock catalogues for the ROBUST method is the same, as explained in Section 3.4. The only difference is that the LF has a Uniform distribution instead of a Gaussian. The number of objects was varied from 5000, 6000 to 10000 and we considered 1000 mock samples for each case. The procedure of generating mock data catalogues for the calculations of χ^2 test is some what different, as described below. We considered 1000 samples of 100 SNIa, with a fractional distance scatter of 0.08. Similar to the method explained in Section 2.6, we have taken the data for the observed cz and the true peculiar velocity field (scaled to $\beta = 0.5$), directly from B99 and the true distances were found from these data. However, we need to follow a different method to find the observed peculiar velocity as explained below. The absolute magnitude (M) of each galaxy was generated from a Uniform distribution as given below;

$$M = \text{Uniform}(M_o - 3, M_o + 3), \tag{3.26}$$

Where M_o is the mean absolute magnitude of the galaxy, which is assumed to be -20.0 same as for the ROBUST method. Then the observed apparent magnitude (m_{obs}) of a galaxy can be given as;

$$m_{obs} = M + 5\log(d_{true}) + 25. \tag{3.27}$$

Now, we can obtain an estimate of the distance (which we denote d_{obs}) of the galaxy by considering the standard candle assumption as follows;

$$d_{obs} = 10^{[0.2(m_{obs}-M_o-25)]}. \tag{3.28}$$

In other words, we assume that the absolute magnitude of the galaxy is equal to the mean absolute magnitude of the LF. Then the observed peculiar velocity ($vpec_{obs}$) is appeared to be;

$$vpec_{obs} = cz_{obs} - d_{obs}. \tag{3.29}$$

The predicted peculiar velocity can be found as;

$$vpec_{pred}(beta = 1.0) = vpec(PSCZ, beta = 1.0) + \sigma_V, \tag{3.30}$$

where σ_V is a Gaussian error and representing the velocity scatter introduce by uncertainties in the reconstructing procedure. The scatter in velocity was varied from 50 km s^{-1} to 300 km s^{-1}. Then we applied the χ^2 test to constrain β as explained in Section (2.5). The results obtained from the ROBUST method as well as the χ^2 test is given in Figure 3.12.

The top panel of Figure 3.12 shows that the distributions of β-estimates(SNIa) are all deviate from $\beta_{true} = 0.5$ for all the velocity scatters, and centred around a value in between 0.4-0.5. Note that as might expect, the deviation increases as the velocity scatter increase (similar to the behaviour seen in Chapter 2). On the other hand all the distributions of β-estimates(ROBUST) centred around 0.5. These results imply that the χ^2 test wouldn't work for distance and peculiar velocity estimates derived from the galaxy LF since it is no longer Gaussian. Also, we can say that even if the

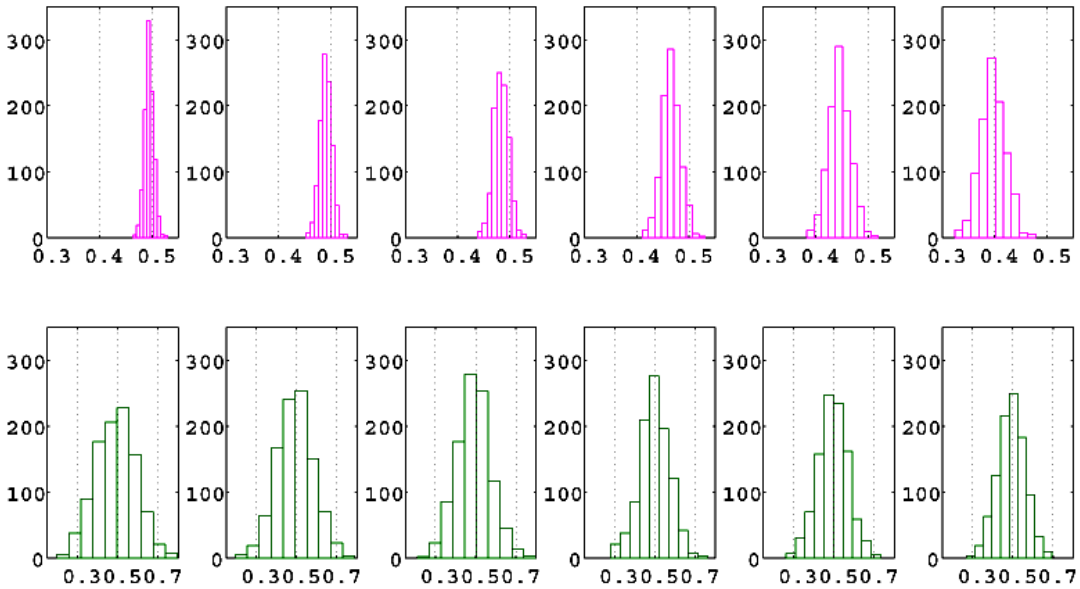

Figure 3.12: β - estimates of objects obtained for a galaxy luminosity function with a Uniform distribution. The top panel denotes the results for SNIa, while the lower panel contains results obtained from the ROBUST method. There are 100 SNIa with a fixed fractional distance scatter of 0.08. The scatter in velocity is varied by 50 km s^{-1} up to 300 km s^{-1} from left to right in the top panel. The number of objects is varied from 5000 to 10000 from left to right in the lower panel, i.e. the number of objects considered for the ROBUST method. The distributions of β-estimates(ROBUST) are centred around $\beta_{true} = 0.5$. However, the distributions of SNIa are deviate from 0.5 and mostly centred around a value in between 0.4-0.5.

LF is very different from a Gaussian the ROBUST method have the ability to give correct β-estimates.

3.8 Conclusion

In this chapter we have reviewed the ROBUST method for fitting peculiar velocity models, originally proposed by Rauzy and Hendry [2000] to analyze the potential of the method with the approach of the next generation of redshift surveys. Also, we did a comparison of χ^2 test with the ROBUST method considering different circumstances. We carried out our analysis considering the IRAS - PSCz catalogue published by Branchini et al. [1999]. The position of each mock object considered to be coincided with one of the PSCz galaxies. The radial distance was considered to be lie within cz $<$ 15,000 km s^{-1}

The determination of the best-fit value of β depends on the null-correlation of ζ_β and u_β (i.e. $\rho(\zeta_\beta, u_\beta) = 0$). A monotonically increasing function from negative to positive, of $\rho(\zeta_\beta, u_\beta)$ vs β, is crucial in determining the best-fit value. ζ_β varies rapidly with the small changes in β causing a considerable fluctuation in $\rho(\zeta_\beta, u_\beta)$. Under this circumstance, a tiny variation in $\rho(\zeta_\beta, u_\beta)$ can change it from being positive to negative or vice versa, when the correlation coefficient is very small. Therefore, it is important *not* to consider a fine grid points for β, and by *linearly interpolating* between values that give $\rho(\zeta_\beta, u_\beta)$ *not* too close to zero, and so less severely affected by the noise, we can get a more reliable answer for the $\rho(\zeta_\beta, u_\beta) = 0$ value for the underlying trend curve.

We have assumed the true value of β to be 0.5 in modelling the mock samples. The best-fit values of β obtained for each sample show a good agreement with the assumed true value. These results suggested the robustness of the ROBUST method for fitting the peculiar velocity models of the next generation of redshift surveys. Specifically, if the luminosity function of the objects considered as a distance indicator, whether there is a large scatter, ROBUST method have the ability to remove the statistical bias and to give promising results in constraining β.

The comparison between χ^2 test and the ROBUST method revealed us important aspects where in some cases χ^2 test shows a good potential in constraining β while ROBUST method become strong in other cases. When constraining β with TF-like distance indicators, χ^2 test become strong than ROBUST. However, when considering SNIa, ROBUST method has shown a relatively good potential compared to χ^2 test. The results obtained from a galaxy luminosity function with a Uniform distribution revealed that the ROBUST method is able to provide correct β-estimates independent of the parametric form of the LF, exactly as the method should do. However, we found that the χ^2 test was less successful when the LF is non-Gaussian.

Chapter 4

Future work

This chapter describes the possible avenues for future development of the research carried out in this thesis. We propose a method that can be applied to constrain β, using χ^2 hypothesis test or ROBUST method, that can be applied to much larger samples of galaxies than the number of PSCz galaxies. If one needs a larger sample of galaxies than the PSCz galaxies, but nonetheless have the mocks mimicking the PSCz spatial distribution, we can use the Probability Integral Transform (PIT) (Section 1.14.2) to generate the above sample as follows.

We used PIT to sample the distance of the mock objects that mimics the PSCz redshift distance distribution in the Local Group frame. As we discussed in Section 1.14.2, the cumulative distribution function of the redshift distance, $P(d) = \int_{-\infty}^{d} p(x)d(x)$ of PSCz galaxies (cdf_{PSCz}) (Figure 4.1), was found from B99. The mock objects are randomly positioned in a 3-D map of the entirely smoothed velocity field of the PSCz galaxies (Figure 4.2). The 3-D map is a box of comoving size of 360.0 Mpc h^{-1}. Again, the larger cube was divided to small cubes, where the dimension of each side is 2.8125 Mpc h^{-1} making 128^3 grid points. Each grid point represents the 3-D distance components in super galactic coordinates and radial peculiar velocity components in $\mathrm{km}s^{-1}$, in the LG frame. The peculiar velocities are scaled for $\beta = 0.5$ on this grid.

The unit vector for the random direction of a galaxy was defined by generating the

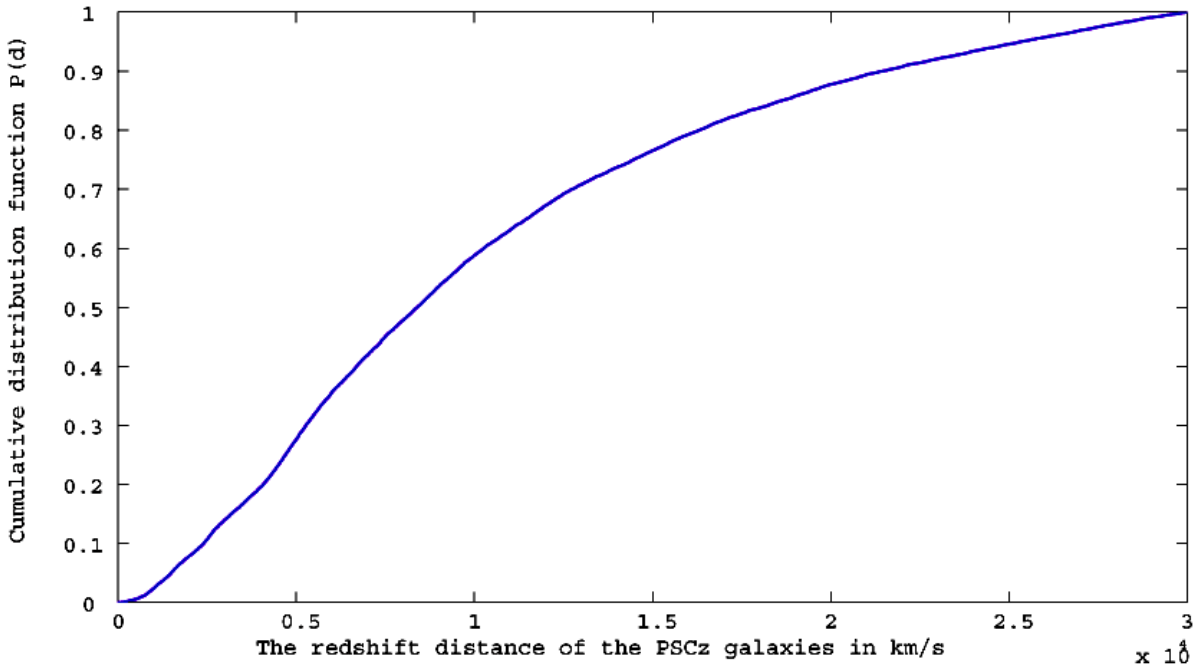

Figure 4.1: The cumulative distribution function of the redshift distance of the PSCz galaxies.

distance coordinates from a uniform distribution, i.e. (x, y, z) = Uniform(-150,150) in Mpc. Then the true radial distance (d_{true}) of the sampled galaxies was obtained by multiplying the corresponding unit vector with the required value obtained from the PIT method (the value taken from the cdf $_{PSCz}$). The distribution of the simulated radial distances (km s^{-1}) is shown in Figure 4.3 as a comparison of the distribution of the redshift distance of the PSCz galaxies. It is important to notice that the distribution of the simulated radial distances (km s^{-1}), mimic the distributions of redshift distances of PSCz galaxies with a considerably good agreement up to 15,000 km s^{-1}. As we stated earlier, for the calculations we truncated the distance up to 15,000 km s^{-1}, depending on the completeness of the PSCz peculiar velocity field. Therefore, whether the mock distance distribution dosen't mimic the PSCz distance distribution beyond 15,000 km s$^{(}-1$) that wouldn't cause any influence on our results.

4.1 Generating data for χ^2 hypothesis test

The true peculiar velocities of the objects (vpec$_{\beta=0.5}$) were predicted by applying a linear interpolation for the peculiar velocity components of the PSCz galaxies, given in the 3-D map. Then the observational data for the recession velocity (cz_{obs}), radial

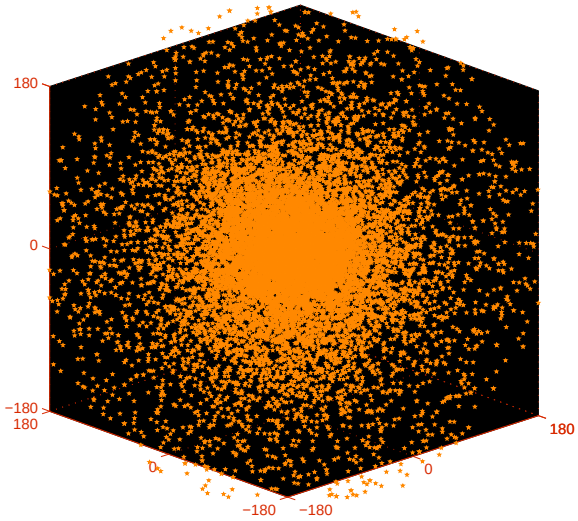

(a)

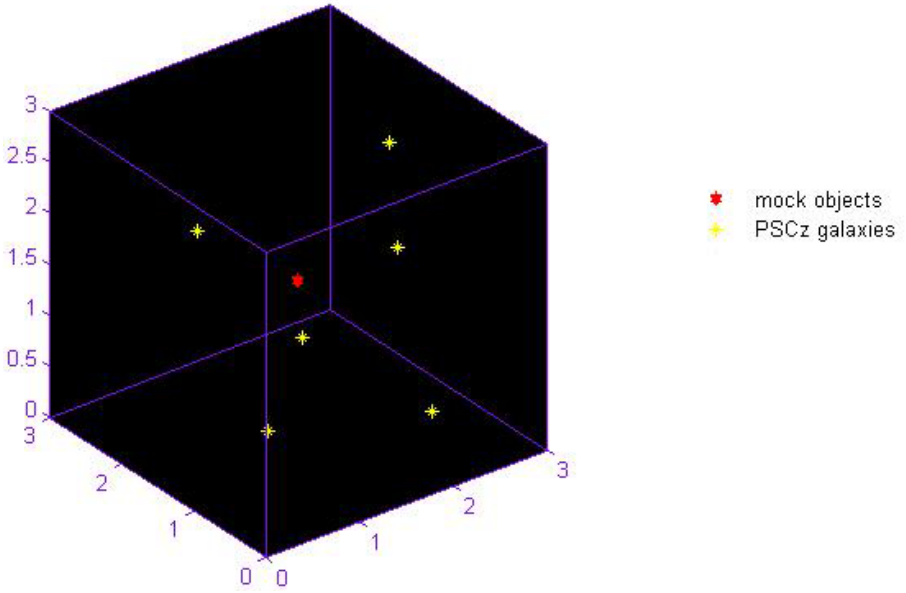

(b)

Figure 4.2: (a) An example of a 3-D map of the galaxies.(b) An illustration of a mock object (red) positioned in a small cube with galaxies (yellow).

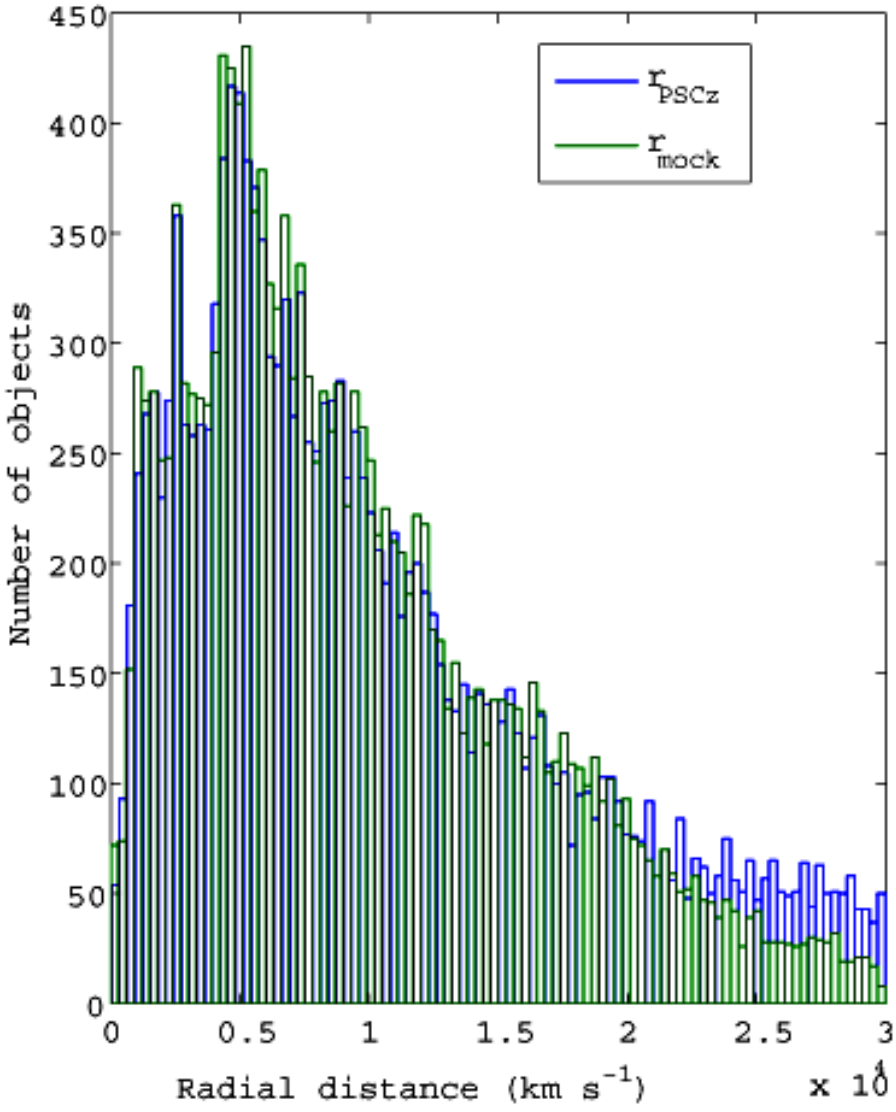

Figure 4.3: Comparison of the PSCz galaxies and mock objects. The diagram shows the distance distribution of both the PSCz galaxies and the mock objects. 15,795 mock objects lie within cz $<$ 15,000 km s^{-1} were considered for the comparison of the distance distribution, as B99 also having the same number of PSCz galaxies. The distance distribution mimic that of PSCz galaxies with a reasonable level of accuracy.

distance (d_{obsII}) and the peculiar velocities ($vpec_{obsII}$) and the predicted peculiar velocities are taken from the simulated data as follows:

- The true recession velocity cz_{II} ($< 15{,}000$ km s^{-1}) was found by adding the true peculiar velocity vpec$_{\beta=0.5}$ and the true radial distance d_{true} obtained from PIT method.

$$cz_{II} = vpec_{\beta=0.5} + H_o\, d_{true} \tag{4.1}$$

- Then the observed recession velocity cz_{obs} was found by adding a Gaussian errors (σ_v, σ_d) to $vpec_{\beta=0.5}$ along with $H_o d_{true}$.

$$cz_{obs} = vpec_{\beta=0.5} + \sigma_v + H_o\, d_{true} + \sigma_d \tag{4.2}$$

- The observed radial distance (d_{obsII}) was found by adding a Gaussian error with a fixed fractional distance scatter σ_d (as given in Chapter 2, Tabel 2.1) to the true radial distance d_{true}.

$$d_{obsII} = d_{true} + \sigma_d \tag{4.3}$$

- The observed peculiar velocity vpec$_{obsII}$ was obtained from cz_{obs} and d_{obsII}.

$$vpec_{obsII} = cz_{obs} - d_{obsII} \tag{4.4}$$

- To obtain the predicted peculiar velocity, $vpec_{\beta=0.5}$ was scaled to $\beta = 1.0$, i.e. $vpec_{\beta=1.0}$. Here a Gaussian error (i.e. σ_v) was added to $vpec_{\beta=1.0}$. Then the predicted peculiar velocity was calculated for each β value, correspondingly.

4.2 Generating data for ROBUST method

In order to apply the ROBUST method the observed recession velocity (cz_{obs}) and the true radial peculiar velocity (vpec$_{\beta=1.0}$) of the mock objects are required. The method we followed to generate cz_{obs} and vpec$_{\beta=1.0}$ is broadly discussed in the above section (i.e.§ 4.1). Further, we need to know the distance modulus (μ) and the absolute magnitudes (M) of the mock objects and these values have been found as

follows. The radial distances of the mock objects are taken from the simulated data, in megaparsec (i.e (i.e. d_{true}), which mimic the redshift distance distribution of the PSCz galaxies. We didn't apply a correction for the radial distance in this case as we are trying to specify the luminosity function as a distance indicator. Then, the true value of the distance modulus μ can be found by;

$$\mu = 5\log_{10}(d) + 25. \tag{4.5}$$

With these data in hand, we can generate M by considering a luminosity function, which does not depend on the spatial distribution of the galaxies, as describe in Chapter 3. Then, following the same procedure in Chapter 3, we can constrain β for a sample with number of galaxies larger than PSCz velocity field, which mimics the PSCz spatial distribution. The advantage of this method is that we are not restricted in determining the number of objects. Therefore this method can be applied for the analysis of the samples with large number of objects to represents the next generation galaxy surveys with huge number of objects -for example, WALLABY. As we discussed in Chapter 1, WALLABY may detect up to 500,000 galaxies to a redshift of 0.26 (i.e. cz = 78,000 km s^{-1}).

Suggestions for further analysis of the ROBUST method:

- To consider other LF models (e.g. Schechter function LF) and so demonstrating that the estimates of β are indeed robust to the choice of LF provided it is independent of position.

- To explore generalised models for galaxy biasing, i.e. to investigate whether -with a sufficiently large survey - one might be able to extend biasing models beyond simple linear biasing and constrain models in which the bias parameter also depends on scale.

- To explore how robust methods are affected by evolutionary and environmental effects - i.e. when the LF does depend (slightly) on distance and redshift. Would the robust method still provide a reliable estimate of beta in these cases?

Bibliography

Aaronson, M., Huchra, J., and Mould, J.: 1979, *ApJ* **229**, 1

Abazajian, K., Adelman-McCarthy, J. K., Agüeros, M. A., Allam, S. S., Anderson, S. F., Annis, J., Bahcall, N. A., Baldry, I. K., Bastian, S., Berlind, A., Bernardi, M., Blanton, M. R., Blythe, N., Bochanski, Jr., J. J., Boroski, W. N., Brewington, H., Briggs, J. W., Brinkmann, J., Brunner, R. J., Budavári, T., Carey, L. N., Carr, M. A., Castander, F. J., Chiu, K., Collinge, M. J., Connolly, A. J., Covey, K. R., Csabai, I., Dalcanton, J. J., Dodelson, S., Doi, M., Dong, F., Eisenstein, D. J., Evans, M. L., Fan, X., Feldman, P. D., Finkbeiner, D. P., Friedman, S. D., Frieman, J. A., Fukugita, M., Gal, R. R., Gillespie, B., Glazebrook, K., Gonzalez, C. F., Gray, J., Grebel, E. K., Grodnicki, L., Gunn, J. E., Gurbani, V. K., Hall, P. B., Hao, L., Harbeck, D., Harris, F. H., Harris, H. C., Harvanek, M., Hawley, S. L., Heckman, T. M., Helmboldt, J. F., Hendry, J. S., Hennessy, G. S., Hindsley, R. B., Hogg, D. W., Holmgren, D. J., Holtzman, J. A., Homer, L., Hui, L., Ichikawa, S., Ichikawa, T., Inkmann, J. P., Ivezić, Ž., Jester, S., Johnston, D. E., Jordan, B., Jordan, W. P., Jorgensen, A. M., Jurić, M., Kauffmann, G., Kent, S. M., Kleinman, S. J., Knapp, G. R., Kniazev, A. Y., Kron, R. G., Krzesiński, J., Kunszt, P. Z., Kuropatkin, N., Lamb, D. Q., Lampeitl, H., Laubscher, B. E., Lee, B. C., Leger, R. F., Li, N., Lidz, A., Lin, H., Loh, Y., Long, D. C., Loveday, J., Lupton, R. H., Malik, T., Margon, B., McGehee, P. M., McKay, T. A., Meiksin, A., Miknaitis, G. A., Moorthy, B. K., Munn, J. A., Murphy, T., Nakajima, R., Narayanan, V. K., Nash, T., Neilsen, Jr., E. H., Newberg, H. J., Newman, P. R., Nichol, R. C., Nicinski, T., Nieto-Santisteban, M., Nitta, A., Odenkirchen, M., Okamura, S., Ostriker, J. P., Owen, R., Padmanabhan, N., Peoples, J., Pier, J. R., Pindor, B., Pope, A. C., Quinn, T. R., Rafikov, R. R., Raymond, S. N., Richards, G. T.,

Richmond, M. W., Rix, H., Rockosi, C. M., Schaye, J., Schlegel, D. J., Schneider, D. P., Schroeder, J., Scranton, R., Sekiguchi, M., Seljak, U., Sergey, G., Sesar, B., Sheldon, E., Shimasaku, K., Siegmund, W. A., Silvestri, N. M., Sinisgalli, A. J., Sirko, E., Smith, J. A., Smolčić, V., Snedden, S. A., Stebbins, A., Steinhardt, C., Stinson, G., Stoughton, C., Strateva, I. V., Strauss, M. A., SubbaRao, M., Szalay, A. S., Szapudi, I., Szkody, P., Tasca, L., Tegmark, M., Thakar, A. R., Tremonti, C., Tucker, D. L., Uomoto, A., Vanden Berk, D. E., Vandenberg, J., Vogeley, M. S., Voges, W., Vogt, N. P., Walkowicz, L. M., Weinberg, D. H., West, A. A., White, S. D. M., Wilhite, B. C., Willman, B., Xu, Y., Yanny, B., Yarger, J., Yasuda, N., Yip, C., Yocum, D. R., York, D. G., Zakamska, N. L., Zehavi, I., Zheng, W., Zibetti, S., and Zucker, D. B.: 2003, *AJ* **126**, 2081

Abazajian, K. N., Adelman-McCarthy, J. K., Agüeros, M. A., Allam, S. S., Allende Prieto, C., An, D., Anderson, K. S. J., Anderson, S. F., Annis, J., Bahcall, N. A., Bailer-Jones, C. A. L., Barentine, J. C., Bassett, B. A., Becker, A. C., Beers, T. C., Bell, E. F., Belokurov, V., Berlind, A. A., Berman, E. F., Bernardi, M., Bickerton, S. J., Bizyaev, D., Blakeslee, J. P., Blanton, M. R., Bochanski, J. J., Boroski, W. N., Brewington, H. J., Brinchmann, J., Brinkmann, J., Brunner, R. J., Budavári, T., Carey, L. N., Carliles, S., Carr, M. A., Castander, F. J., Cinabro, D., Connolly, A. J., Csabai, I., Cunha, C. E., Czarapata, P. C., Davenport, J. R. A., de Haas, E., Dilday, B., Doi, M., Eisenstein, D. J., Evans, M. L., Evans, N. W., Fan, X., Friedman, S. D., Frieman, J. A., Fukugita, M., Gänsicke, B. T., Gates, E., Gillespie, B., Gilmore, G., Gonzalez, B., Gonzalez, C. F., Grebel, E. K., Gunn, J. E., Györy, Z., Hall, P. B., Harding, P., Harris, F. H., Harvanek, M., Hawley, S. L., Hayes, J. J. E., Heckman, T. M., Hendry, J. S., Hennessy, G. S., Hindsley, R. B., Hoblitt, J., Hogan, C. J., Hogg, D. W., Holtzman, J. A., Hyde, J. B., Ichikawa, S., Ichikawa, T., Im, M., Ivezić, Ž., Jester, S., Jiang, L., Johnson, J. A., Jorgensen, A. M., Jurić, M., Kent, S. M., Kessler, R., Kleinman, S. J., Knapp, G. R., Konishi, K., Kron, R. G., Krzesinski, J., Kuropatkin, N., Lampeitl, H., Lebedeva, S., Lee, M. G., Lee, Y. S., Leger, R. F., Lépine, S., Li, N., Lima, M., Lin, H., Long, D. C., Loomis, C. P., Loveday, J., Lupton, R. H., Magnier, E., Malanushenko, O., Malanushenko, V., Mandelbaum, R., Margon, B., Marriner,

J. P., Martínez-Delgado, D., Matsubara, T., McGehee, P. M., McKay, T. A., Meiksin, A., Morrison, H. L., Mullally, F., Munn, J. A., Murphy, T., Nash, T., Nebot, A., Neilsen, E. H., Newberg, H. J., Newman, P. R., Nichol, R. C., Nicinski, T., Nieto-Santisteban, M., Nitta, A., Okamura, S., Oravetz, D. J., Ostriker, J. P., Owen, R., Padmanabhan, N., Pan, K., Park, C., Pauls, G., Peoples, J., Percival, W. J., Pier, J. R., Pope, A. C., Pourbaix, D., Price, P. A., Purger, N., Quinn, T., Raddick, M. J., Fiorentin, P. R., Richards, G. T., Richmond, M. W., Riess, A. G., Rix, H., Rockosi, C. M., Sako, M., Schlegel, D. J., Schneider, D. P., Scholz, R., Schreiber, M. R., Schwope, A. D., Seljak, U., Sesar, B., Sheldon, E., Shimasaku, K., Sibley, V. C., Simmons, A. E., Sivarani, T., Smith, J. A., Smith, M. C., Smolčić, V., Snedden, S. A., Stebbins, A., Steinmetz, M., Stoughton, C., Strauss, M. A., Subba Rao, M., Suto, Y., Szalay, A. S., Szapudi, I., Szkody, P., Tanaka, M., Tegmark, M., Teodoro, L. F. A., Thakar, A. R., Tremonti, C. A., Tucker, D. L., Uomoto, A., Vanden Berk, D. E., Vandenberg, J., Vidrih, S., Vogeley, M. S., Voges, W., Vogt, N. P., Wadadekar, Y., Watters, S., Weinberg, D. H., West, A. A., White, S. D. M., Wilhite, B. C., Wonders, A. C., Yanny, B., Yocum, D. R., York, D. G., Zehavi, I., Zibetti, S., and Zucker, D. B.: 2009, *APJS* **182**, 543

Adler, R., Bazin, M., and Schiffer, M.: 1965, *Introduction to general relativity*, International Series in pure and applied physics, New York: McGraw-Hill,1965

An, D., Terndrup, D. M., and Pinsonneault, M. H.: 2007, *ApJ* **671**, 1640

Babul, A. and White, S. D. M.: 1991, *MNRAS* **253**, 31P

Bardeen, J. M., Bond, J. R., Kaiser, N., and Szalay, A. S.: 1986, *ApJ* **304**, 15

Basilakos, S. and Plionis, M.: 2006, *MNRAS* **373**, 1112

Benedict, G. F., McArthur, B. E., Feast, M. W., Barnes, T. G., Harrison, T. E., Patterson, R. J., Menzies, J. W., Bean, J. L., and Freedman, W. L.: 2007, *AJ* **133**, 1810

Bennett, C. L., Hill, R. S., Hinshaw, G., Nolta, M. R., Odegard, N., Page, L., Spergel, D. N., Weiland, J. L., Wright, E. L., Halpern, M., Jarosik, N., Kogut, A., Limon, M., Meyer, S. S., Tucker, G. S., and Wollack, E.: 2003, *ApJS* **148**, 97

Bennett, C. L., Smoot, G. F., Hinshaw, G., Wright, E. L., Kogut, A., de Amici, G., Meyer, S. S., Weiss, R., Wilkinson, D. T., Gulkis, S., Janssen, M., Boggess, N. W., Cheng, E. S., Hauser, M. G., Kelsall, T., Mather, J. C., Moseley, Jr., S. H., Murdock, T. L., and Silverberg, R. F.: 1992, *ApJl* **396**, L7

Bertschinger, E. and Dekel, A.: 1991, in D. W. Latham & L. A. N. da Costa (ed.), *Large-scale Structures and Peculiar Motions in the Universe*, Vol. 15 of *Astronomical Society of the Pacific Conference Series*, pp 67–+

Bertschinger, E., Dekel, A., Faber, S. M., Dressler, A., and Burstein, D.: 1990, *ApJ* **364**, 370

Bigot, G., Rauzy, S., and Triay, R.: 1991, *Physics Letters A* **158**, 282

Blakeslee, J. P., Davis, M., Tonry, J. L., Dressler, A., and Ajhar, E. A.: 1999, *ApJl* **527**, L73

Bono, G.: 2003, in D. Alloin and W. Gieren (eds.), *Stellar Candles for the Extragalactic Distance Scale*, Vol. 635 of *Lecture Notes in Physics, Berlin Springer Verlag*, pp 85–104

Bono, G., Caputo, F., Castellani, V., Marconi, M., and Storm, J.: 2001, *MNRAS* **326**, 1183

Bono, G., Caputo, F., Castellani, V., Marconi, M., Storm, J., and Degl'Innocenti, S.: 2003, *MNRAS* **344**, 1097

Bothun, G. (ed.): 1998, *Modern cosmological observations and problems*

Bower, R. G., Coles, P., Frenk, C. S., and White, S. D. M.: 1993, *ApJ* **405**, 403

Branch, D. and Miller, D. L.: 1993, *ApJl* **405**, L5

Branchini, E., Teodoro, L., Frenk, C. S., Schmoldt, I., Efstathiou, G., White, S. D. M., Saunders, W., Sutherland, W., Rowan-Robinson, M., Keeble, O., Tadros, H., Maddox, S., and Oliver, S.: 1999, *MNRAS* **308**, 1

Burkey, D. and Taylor, A. N.: 2004, *MNRAS* **347**, 255

Butkevich, A. G., Berdyugin, A. V., and Teerikorpi, P.: 2005, *MNRAS* **362**, 321

Caldwell, J. A. R.: 1983, *The Observatory* **103**, 244

Colless, M., Dalton, G., Maddox, S., Sutherland, W., Norberg, P., Cole, S., Bland-Hawthorn, J., Bridges, T., Cannon, R., Collins, C., Couch, W., Cross, N., Deeley, K., De Propris, R., Driver, S. P., Efstathiou, G., Ellis, R. S., Frenk, C. S., Glazebrook, K., Jackson, C., Lahav, O., Lewis, I., Lumsden, S., Madgwick, D., Peacock, J. A., Peterson, B. A., Price, I., Seaborne, M., and Taylor, K.: 2001, *MNRAS* **328**, 1039

Conley, A., Sullivan, M., Hsiao, E. Y., Guy, J., Astier, P., Balam, D., Balland, C., Basa, S., Carlberg, R. G., Fouchez, D., Hardin, D., Howell, D. A., Hook, I. M., Pain, R., Perrett, K., Pritchet, C. J., and Regnault, N.: 2008, *ApJ* **681**, 482

Corey, B. E. and Wilkinson, D. T.: 1976, in *Bulletin of the American Astronomical Society*, Vol. 8 of *Bulletin of the American Astronomical Society*, pp 351–+

Croft, R. A. C. and Gaztanaga, E.: 1997, *MNRAS* **285**, 793

Cutler, C.: 1998, *PhRvD* **57**, 7089

da Costa, L. N., Freudling, W., Wegner, G., Giovanelli, R., Haynes, M. P., and Salzer, J. J.: 1996, *ApJl* **468**, L5+

Dalal, N., Holz, D. E., Hughes, S. A., and Jain, B.: 2006, *Phys.Rev.D.* **74(6)**, 063006

Davis, M. and Djorgovski, S.: 1985, *ApJ* **299**, 15

Dekel, A., Bertschinger, E., Yahil, A., Strauss, M. A., Davis, M., and Huchra, J. P.: 1993, *ApJ* **412**, 1

Dekel, A., Eldar, A., Kolatt, T., Yahil, A., Willick, J. A., Faber, S. M., Courteau, S., and Burstein, D.: 1999, *ApJ* **522**, 1

Driver, S. P., the GAMA Team, Baldry, I. K., Bamford, S., Bland-Hawthorn, J., Bridges, T., Cameron, E., Conselice, C., Couch, W. J., Croom, S., Cross, N. J. G., Driver, S. P., Dunne, L., Eales, S., Edmondson, E., Ellis, S. C., Frenk, C. S.,

Graham, A. W., Jones, H., Hill, D., Hopkins, A., van Kampen, E., Kuijken, K., Lahav, O., Liske, J., Loveday, J., Nichol, B., Norberg, P., Oliver, S., Parkinson, H., Peacock, J. A., Phillipps, S., Popescu, C. C., Prescott, M., Proctor, R., Sharp, R., Staveley-Smith, L., Sutherland, W., Tuffs, R. J., and Warren, S.: 2009, in J. Andersen, J. Bland-Hawthorn, & B. Nordström (ed.), *IAU Symposium*, Vol. 254 of *IAU Symposium*, pp 469–474

Efron, B. and Petrosian, V.: 1992, *ApJ* **399**, 345

Erdoğdu, P., Huchra, J. P., Lahav, O., Colless, M., Cutri, R. M., Falco, E., George, T., Jarrett, T., Jones, D. H., Kochanek, C. S., Macri, L., Mader, J., Martimbeau, N., Pahre, M., Parker, Q., Rassat, A., and Saunders, W.: 2006, *MNRAS* **368**, 1515

Fabbri, R., Guidi, I., Melchiorri, F., and Natale, V.: 1980, *Physical Review Letters* **44**, 1563

Federspiel, M., Sandage, A., and Tammann, G. A.: 1994, *ApJ* **430**, 29

Filippenko, A. V.: 2005, in E. M. Sion, S. Vennes, and H. L. Shipman (eds.), *White dwarfs: cosmological and galactic probes*, Vol. 332 of *Astrophysics and Space Science Library*, pp 97–133

Fisher, K. B., Huchra, J. P., Strauss, M. A., Davis, M., Yahil, A., and Schlegel, D.: 1995a, *ApJS* **100**, 69

Fisher, K. B., Lahav, O., Hoffman, Y., Lynden-Bell, D., and Zaroubi, S.: 1995b, *MNRAS* **272**, 885

Freedman, W. L., Madore, B. F., Gibson, B. K., Ferrarese, L., Kelson, D. D., Sakai, S., Mould, J. R., Kennicutt, Jr., R. C., Ford, H. C., Graham, J. A., Huchra, J. P., Hughes, S. M. G., Illingworth, G. D., Macri, L. M., and Stetson, P. B.: 2001, *ApJ* **553**, 47

Freudling, W., Zehavi, I., da Costa, L. N., Dekel, A., Eldar, A., Giovanelli, R., Haynes, M. P., Salzer, J. J., Wegner, G., and Zaroubi, S.: 1999, *ApJ* **523**, 1

Gaensler, B. M.: 2009, in *IAU Symposium*, Vol. 259 of *IAU Symposium*, pp 645–652

Geller, M. J. and Huchra, J. P.: 1983, *ApJS* **52**, 61

Giovanelli, R., Haynes, M. P., Salzer, J. J., Wegner, G., da Costa, L. N., and Freudling, W.: 1998, *AJ* **116**, 2632

Goldhaber, G., Groom, D. E., Kim, A., Aldering, G., Astier, P., Conley, A., Deustua, S. E., Ellis, R., Fabbro, S., Fruchter, A. S., Goobar, A., Hook, I., Irwin, M., Kim, M., Knop, R. A., Lidman, C., McMahon, R., Nugent, P. E., Pain, R., Panagia, N., Pennypacker, C. R., Perlmutter, S., Ruiz-Lapuente, P., Schaefer, B., Walton, N. A., and York, T.: 2001, *ApJ* **558**, 359

Gonzalez, A. H. and Faber, S. M.: 1997, *ApJ* **485**, 80

Guy, J., Astier, P., Nobili, S., Regnault, N., and Pain, R.: 2005, *A&A* **443**, 781

Haehnelt, M. G.: 1994, *MNRAS* **269**, 199

Hamilton, A. J. S.: 1998, in D. Hamilton (ed.), *The Evolving Universe*, Vol. 231 of *Astrophysics and Space Science Library*, pp 185–+

Hamuy, M., Phillips, M. M., Maza, J., Suntzeff, N. B., Schommer, R. A., and Aviles, R.: 1995, *AJ* **109**, 1

Han, M.: 1992, *ApJ* **395**, 75

Hendry, M.: 2001, in B. A. Steves & A. J. Maciejewski (ed.), *The Restless Universe*, p. 191

Hendry, M. and Woan, G.: 2007, *Astronomy and Geophysics* **48(1)**, 010000

Hendry, M. A., Rauzy, S., Goodwin, S. P., and Gribbin, J.: 2001, *MNRAS* **324**, 717

Hendry, M. A. and Simmons, J. F. L.: 1995, *Vistas in Astronomy* **39**, 297

Hicken, M., Wood-Vasey, W. M., Blondin, S., Challis, P., Jha, S., Kelly, P. L., Rest, A., and Kirshner, R. P.: 2009, *ApJ* **700**, 1097

Hinshaw, G., Weiland, J. L., Hill, R. S., Odegard, N., Larson, D., Bennett, C. L., Dunkley, J., Gold, B., Greason, M. R., Jarosik, N., Komatsu, E., Nolta, M. R.,

Page, L., Spergel, D. N., Wollack, E., Halpern, M., Kogut, A., Limon, M., Meyer, S. S., Tucker, G. S., and Wright, E. L.: 2009, *ApJS* **180**, 225

Hogg, D. W.: 1999, *ArXiv Astrophysics e-prints*

Holz, D. E. and Hughes, S. A.: 2005, *ApJ* **629**, 15

Hu, W., Eisenstein, D. J., Tegmark, M., and White, M.: 1999, *PhRvD* **59(2)**, 023512

Hubble, E.: 1929, *Proceedings of the National Academy of Science* **15**, 168

Hudson, M. J.: 1994, *MNRAS* **266**, 475

Hudson, M. J., Smith, R. J., Lucey, J. R., and Branchini, E.: 2004, *MNRAS* **352**, 61

Isern, J., Lopez, R., and Simonneau, E.: 1989, *ApSS* **157**, 315

Jarosik, N., Barnes, C., Greason, M. R., Hill, R. S., Nolta, M. R., Odegard, N., Weiland, J. L., Bean, R., Bennett, C. L., Doré, O., Halpern, M., Hinshaw, G., Kogut, A., Komatsu, E., Limon, M., Meyer, S. S., Page, L., Spergel, D. N., Tucker, G. S., Wollack, E., and Wright, E. L.: 2007, *ApJS* **170**, 263

Jarosik, N., Bennett, C. L., Dunkley, J., Gold, B., Greason, M. R., Halpern, M., Hill, R. S., Hinshaw, G., Kogut, A., Komatsu, E., Larson, D., Limon, M., Meyer, S. S., Nolta, M. R., Odegard, N., Page, L., Smith, K. M., Spergel, D. N., Tucker, G. S., Weiland, J. L., Wollack, E., and Wright, E. L.: 2010, *ArXiv e-prints*

Jarrett, T., Chester, T., Cutri, R., Schneider, S., Rosenberg, J., Huchra, J. P., and Mader, J.: 2000, *AJ* **120**, 298

Jennings, M., Pereztomas, A., Davies, M., Walker, D., Zhu, L., Losee, P., Huang, W., Balachandran, S., Guy, O., and Covington, J.: 2007, *Solid State Electronics* **51**, 797

Jha, S., Riess, A. G., and Kirshner, R. P.: 2007, *ApJ* **659**, 122

Johnston, S., Taylor, R., Bailes, M., Bartel, N., Baugh, C., Bietenholz, M., Blake, C., Braun, R., Brown, J., Chatterjee, S., Darling, J., Deller, A., Dodson, R., Edwards,

P., Ekers, R., Ellingsen, S., Feain, I., Gaensler, B., Haverkorn, M., Hobbs, G., Hopkins, A., Jackson, C., James, C., Joncas, G., Kaspi, V., Kilborn, V., Koribalski, B., Kothes, R., Landecker, T., Lenc, A., Lovell, J., Macquart, J.-P., Manchester, R., Matthews, D., McClure-Griffiths, N., Norris, R., Pen, U.-L., Phillips, C., Power, C., Protheroe, R., Sadler, E., Schmidt, B., Stairs, I., Staveley-Smith, L., Stil, J., Tingay, S., Tzioumis, A., Walker, M., Wall, J., and Wolleben, M.: 2008, *Experimental Astronomy* **22**, 151

Jones, D. H., Read, M. A., Saunders, W., Colless, M., Jarrett, T., Parker, Q., Fairall, A., Mauch, T., Sadler, E., Watson, F., Burton, D., Campbell, L., Cass, P., Croom, S., Dawe, J., Fiegert, K., Frankcombe, L., Hartley, M., Huchra, J., James, D., Kirby, E., Lahav, O., Lucey, J., Mamon, G., Moore, L., Peterson, B., Prior, S., Proust, D., Russell, K., Safouris, V., ichi Wakamatsu, K., Westra, E., and Williams, M.: 2009, *The 6dF Galaxy Survey: Final Redshift Release (DR3) and Southern Large-Scale Structures*

Jones, D. H., Read, M. A., Saunders, W., Colless, M., Jarrett, T., Parker, Q. A., Fairall, A. P., Mauch, T., Sadler, E. M., Watson, F. G., Burton, D., Campbell, L. A., Cass, P., Croom, S. M., Dawe, J., Fiegert, K., Frankcombe, L., Hartley, M., Huchra, J., James, D., Kirby, E., Lahav, O., Lucey, J., Mamon, G. A., Moore, L., Peterson, B. A., Prior, S., Proust, D., Russell, K., Safouris, V., Wakamatsu, K.-I., Westra, E., and Williams, M.: 2009, *MNRAS* pp 1206–+

Jones, D. H., Saunders, W., Colless, M., Read, M. A., Parker, Q. A., Watson, F. G., Campbell, L. A., Burkey, D., Mauch, T., Moore, L., Hartley, M., Cass, P., James, D., Russell, K., Fiegert, K., Dawe, J., Huchra, J., Jarrett, T., Lahav, O., Lucey, J., Mamon, G. A., Proust, D., Sadler, E. M., and Wakamatsu, K.: 2004, *MNRAS* **355**, 747

Jones, D. H., Saunders, W., Read, M., and Colless, M.: 2005, *Publications of the Astronomical Society of Australia* **22**, 277

Jones, R. V., Carney, B. W., and Fulbright, J. P.: 1996, *PASP* **108**, 877

Kaiser, N.: 1984, *ApJl* **284**, L9

Kaiser, N.: 1987, *MNRAS* **227**, 1

Kaiser, N., Efstathiou, G., Saunders, W., Ellis, R., Frenk, C., Lawrence, A., and Rowan-Robinson, M.: 1991, *MNRAS* **252**, 1

Komatsu, E., Smith, K. M., Dunkley, J., Bennett, C. L., Gold, B., Hinshaw, G., Jarosik, N., Larson, D., Nolta, M. R., Page, L., Spergel, D. N., Halpern, M., Hill, R. S., Kogut, A., Limon, M., Meyer, S. S., Odegard, N., Tucker, G. S., Weiland, J. L., Wollack, E., and Wright, E. L.: 2010, *ArXiv e-prints*

Koushiappas, S. M., Bullock, J. S., and Dekel, A.: 2004, *MNRAS* **354**, 292

Kovač, K., Lilly, S. J., Cucciati, O., Porciani, C., Iovino, A., Zamorani, G., Oesch, P., Bolzonella, M., Knobel, C., Finoguenov, A., Peng, Y., Carollo, C. M., Pozzetti, L., Caputi, K., Silverman, J. D., Tasca, L. A. M., Scodeggio, M., Vergani, D., Scoville, N. Z., Capak, P., Contini, T., Kneib, J., Le Fèvre, O., Mainieri, V., Renzini, A., Bardelli, S., Bongiorno, A., Coppa, G., de la Torre, S., de Ravel, L., Franzetti, P., Garilli, B., Guzzo, L., Kampczyk, P., Lamareille, F., Le Borgne, J., Le Brun, V., Maier, C., Mignoli, M., Pello, R., Perez Montero, E., Ricciardelli, E., Tanaka, M., Tresse, L., Zucca, E., Abbas, U., Bottini, D., Cappi, A., Cassata, P., Cimatti, A., Fumana, M., Koekemoer, A. M., Maccagni, D., Marinoni, C., McCracken, H. J., Memeo, P., Meneux, B., and Scaramella, R.: 2010, *ApJ* **708**, 505

Kowalski, M., Rubin, D., Aldering, G., Agostinho, R. J., Amadon, A., Amanullah, R., Balland, C., Barbary, K., Blanc, G., Challis, P. J., Conley, A., Connolly, N. V., Covarrubias, R., Dawson, K. S., Deustua, S. E., Ellis, R., Fabbro, S., Fadeyev, V., Fan, X., Farris, B., Folatelli, G., Frye, B. L., Garavini, G., Gates, E. L., Germany, L., Goldhaber, G., Goldman, B., Goobar, A., Groom, D. E., Haissinski, J., Hardin, D., Hook, I., Kent, S., Kim, A. G., Knop, R. A., Lidman, C., Linder, E. V., Mendez, J., Meyers, J., Miller, G. J., Moniez, M., Mourão, A. M., Newberg, H., Nobili, S., Nugent, P. E., Pain, R., Perdereau, O., Perlmutter, S., Phillips, M. M., Prasad, V., Quimby, R., Regnault, N., Rich, J., Rubenstein, E. P., Ruiz-Lapuente, P., Santos, F. D., Schaefer, B. E., Schommer, R. A., Smith, R. C., Soderberg, A. M., Spadafora, A. L., Strolger, L.-G., Strovink, M., Suntzeff, N. B., Suzuki, N., Thomas, R. C.,

Walton, N. A., Wang, L., Wood-Vasey, W. M., and Yun, J. L.: 2008, *APJ* **686**, 749

Krisciunas, K., Phillips, M. M., and Suntzeff, N. B.: 2004, *ApJl* **602**, L81

Krisciunas, K., Suntzeff, N. B., Candia, P., Arenas, J., Espinoza, J., Gonzalez, D., Gonzalez, S., Höflich, P. A., Landolt, A. U., Phillips, M. M., and Pizarro, S.: 2003, *AJ* **125**, 166

Lahav, O., Lilje, P. B., Primack, J. R., and Rees, M. J.: 1991, *MNRAS* **251**, 128

Landy, S. D. and Szalay, A. S.: 1992, *ApJ* **391**, 494

Lang, R. N. and Hughes, S. A.: 2006, *Phys.Rev.D.* **74(12)**, 122001

Liddle, A.: 2003, *An Introduction to Modern Cosmology, Second Edition*, WILEY

Liu, T. and Janes, K. A.: 1990, *ApJ* **354**, 273

Longmore, A. J., Fernley, J. A., and Jameson, R. F.: 1986, *MNRAS* **220**, 279

Lupton, R., Gunn, J. E., Ivezić, Z., Knapp, G. R., and Kent, S.: 2001, in F. R. Harnden Jr., F. A. Primini, & H. E. Payne (ed.), *Astronomical Data Analysis Software and Systems X*, Vol. 238 of *Astronomical Society of the Pacific Conference Series*, pp 269–+

Madore, B. F. and Freedman, W. L.: 1991, *PASP* **103**, 933

Maller, A. H., McIntosh, D. H., Katz, N., and Weinberg, M. D.: 2003, *ApJl* **598**, L1

Masters, K. L.: 2008, in A. H. Bridle, J. J. Condon, & G. C. Hunt (ed.), *Frontiers of Astrophysics: A Celebration of NRAO's 50th Anniversary*, Vol. 395 of *Astronomical Society of the Pacific Conference Series*, pp 137–+

Mathewson, D. S., Ford, V. L., and Buchhorn, M.: 1992, *ApJl* **389**, L5

Mauskopf, P. D., Ade, P. A. R., de Bernardis, P., Bock, J. J., Borrill, J., Boscaleri, A., Crill, B. P., DeGasperis, G., De Troia, G., Farese, P., Ferreira, P. G., Ganga, K., Giacometti, M., Hanany, S., Hristov, V. V., Iacoangeli, A., Jaffe, A. H., Lange,

A. E., Lee, A. T., Masi, S., Melchiorri, A., Melchiorri, F., Miglio, L., Montroy, T., Netterfield, C. B., Pascale, E., Piacentini, F., Richards, P. L., Romeo, G., Ruhl, J. E., Scannapieco, E., Scaramuzzi, F., Stompor, R., and Vittorio, N.: 2000, *ApJ* **536**, L59

Maza, J., Hamuy, M., Suntzeff, N. B., Phillips, M. M., and Aviles, R.: 1993, in *Bulletin of the American Astronomical Society*, Vol. 25 of *Bulletin of the American Astronomical Society*, pp 1340–+

Meyer, M.: 2009, *ArXiv e-prints*

Meyer, M. J., Zwaan, M. A., Webster, R. L., Schneider, S., and Staveley-Smith, L.: 2008, *MNRAS* **391**, 1712

Miller, A. D., Caldwell, R., Devlin, M. J., Dorwart, W. B., Herbig, T., Nolta, M. R., Page, L. A., Puchalla, J., Torbet, E., and Tran, H. T.: 1999, *ApJ* **524**, L1

Mo, H. J., Mao, S., and White, S. D. M.: 1998, *MNRAS* **295**, 319

Neill, J. D., Hudson, M. J., and Conley, A.: 2007, *ApJl* **661**, L123

Neugebauer, G., Habing, H. J., van Duinen, R., Aumann, H. H., Baud, B., Beichman, C. A., Beintema, D. A., Boggess, N., Clegg, P. E., de Jong, T., Emerson, J. P., Gautier, T. N., Gillett, F. C., Harris, S., Hauser, M. G., Houck, J. R., Jennings, R. E., Low, F. J., Marsden, P. L., Miley, G., Olnon, F. M., Pottasch, S. R., Raimond, E., Rowan-Robinson, M., Soifer, B. T., Walker, R. G., Wesselius, P. R., and Young, E.: 1984, *ApJl* **278**, L1

Newsam, A., Simmons, J. F. L., and Hendry, M. A.: 1995, *A&A* **294**, 627

Nusser, A. and Davis, M.: 1994, *ApJl* **421**, L1

Obrić, M., Ivezić, Ž., Best, P. N., Lupton, R. H., Tremonti, C., Brinchmann, J., Agüeros, M. A., Knapp, G. R., Gunn, J. E., Rockosi, C. M., Schlegel, D., Finkbeiner, D., Gaćeša, M., Smolčić, V., Anderson, S. F., Voges, W., Jurić, M., Siverd, R. J., Steinhardt, W., Jagoda, A. S., Blanton, M. R., and Schneider, D. P.: 2006, *MNRAS* **370**, 1677

Paczynski, B.: 1985, in D. Q. Lamb & J. Patterson (ed.), *Cataclysmic Variables and Low-Mass X-ray Binaries*, Vol. 113 of *Astrophysics and Space Science Library*, pp 1–12

Park, C.-G. and Park, C.: 2006, *ApJ* **637**, 1

Peacock, J. A. and Heavens, A. F.: 1985, *MNRAS* **217**, 805

Peebles, P. J. E.: 1980, *The large-scale structure of the universe*

Peebles, P. J. E.: 1990, *ApJ* **362**, 1

Penzias, A. A. and Wilson, R. W.: 1965, *ApJ* **142**, 419

Perlmutter, S., Aldering, G., Goldhaber, G., Knop, R. A., Nugent, P., Castro, P. G., Deustua, S., Fabbro, S., Goobar, A., Groom, D. E., Hook, I. M., Kim, A. G., Kim, M. Y., Lee, J. C., Nunes, N. J., Pain, R., Pennypacker, C. R., Quimby, R., Lidman, C., Ellis, R. S., Irwin, M., McMahon, R. G., Ruiz-Lapuente, P., Walton, N., Schaefer, B., Boyle, B. J., Filippenko, A. V., Matheson, T., Fruchter, A. S., Panagia, N., Newberg, H. J. M., Couch, W. J., and The Supernova Cosmology Project: 1999, *ApJ* **517**, 565

Perlmutter, S., Gabi, S., Goldhaber, G., Goobar, A., Groom, D. E., Hook, I. M., Kim, A. G., Kim, M. Y., Lee, J. C., Pain, R., Pennypacker, C. R., Small, I. A., Ellis, R. S., McMahon, R. G., Boyle, B. J., Bunclark, P. S., Carter, D., Irwin, M. J., Glazebrook, K., Newberg, H. J. M., Filippenko, A. V., Matheson, T., Dopita, M., Couch, W. J., and The Supernova Cosmology Project: 1997, *ApJ* **483**, 565

Phillips, M. M.: 1993, *ApJl* **413**, L105

Pike, R. W. and Hudson, M. J.: 2005, *ApJ* **635**, 11

Prieto, J. L., Rest, A., and Suntzeff, N. B.: 2006, *ApJ* **647**, 501

Radburn-Smith, D. J., Lucey, J. R., and Hudson, M. J.: 2004, *MNRAS* **355**, 1378

Rauzy, S.: 1997, *A&AS* **125**, 255

Rauzy, S. and Hendry, M. A.: 2000, *MNRAS* **316**, 621

Rauzy, S., Hendry, M. A., and D'Mellow, K.: 2001, *MNRAS* **328**, 1016

Reid, B. A., Verde, L., Jimenez, R., and Mena, O.: 2010, *Journal of Cosmology and Astro-Particle Physics* **1**, 3

Riess, A. G., Davis, M., Baker, J., and Kirshner, R. P.: 1997, *ApJl* **488**, L1+

Riess, A. G., Macri, L., Casertano, S., Sosey, M., Lampeitl, H., Ferguson, H. C., Filippenko, A. V., Jha, S. W., Li, W., Chornock, R., and Sarkar, D.: 2009, *ApJ* **699**, 539

Riess, A. G., Press, W. H., and Kirshner, R. P.: 1996, *ApJ* **473**, 88

Robertson, H. P.: 1935, *ApJ* **82**, 284

Rowan-Robinson, M.: 1985, *The cosmological distance ladder: Distance and time in the universe*, STI

Rowan-Robinson, M., Clegg, P. E., Beichman, C. A., Neugebauer, G., Soifer, B. T., Aumann, H. H., Beintema, D. A., Boggess, N., Emerson, J. P., Gautier, T. N., Gillett, F. C., Hauser, M. G., Houck, J. R., Low, F. J., and Walker, R. G.: 1984, *ApJl* **278**, L7

Sandage, A.: 1958, *ApJ* **127**, 513

Sandage, A.: 1988, *ARA&A* **26**, 561

Sandage, A. and Tammann, G. A.: 1976, *ApJ* **210**, 7

Sanders, D. B., Egami, E., Lipari, S., Mirabel, I. F., and Soifer, B. T.: 1995, *AJ* **110**, 1993

Sanders, D. B., Mazzarella, J. M., Kim, D.-C., Surace, J. A., and Soifer, B. T.: 2003, *AJ* **126**, 1607

Saunders, W., Oliver, S., Keeble, O., Rowan-Robinson, M., Maddox, S., McMahon, R., Efstathiou, G., Sutherland, W., Tadros, H., White, S., and Frenk, C.: 1999, *ArXiv Astrophysics e-prints*

Saunders, W., Sutherland, W. J., Maddox, S. J., Keeble, O., Oliver, S. J., Rowan-Robinson, M., McMahon, R. G., Efstathiou, G. P., Tadros, H., White, S. D. M., Frenk, C. S., Carramiñana, A., and Hawkins, M. R. S.: 2000, *MNRAS* **317**, 55

Schilizzi, R. T., Dewdney, P. E. F., and Lazio, T. J. W.: 2008, in *Society of Photo-Optical Instrumentation Engineers (SPIE) Conference Series*, Vol. 7012 of *Presented at the Society of Photo-Optical Instrumentation Engineers (SPIE) Conference*

Schombert, J. M., Pildis, R. A., and Eder, J. A.: 1997, *ApJS* **111**, 233

Schommer, R. A., Olszewski, E. W., and Aaronson, M.: 1984, *ApJl* **285**, L53

Schutz, B. F.: 1986, *Nature* **323**, 310

Sekiguchi, T., Ichikawa, K., Takahashi, T., and Greenhill, L.: 2009, *ArXiv e-prints*

Shanks, T., Bean, A. J., Ellis, R. S., Fong, R., Efstathiou, G., and Peterson, B. A.: 1983, *ApJ* **274**, 529

Shaya, E. J., Peebles, P. J. E., and Tully, R. B.: 1995, *ApJ* **454**, 15

Sigad, Y., Eldar, A., Dekel, A., Strauss, M. A., and Yahil, A.: 1998, *ApJ* **495**, 516

Skillen, I., Fernley, J. A., Stobie, R. S., and Jameson, R. F.: 1993, *MNRAS* **265**, 301

Skrutskie, M. F., Cutri, R. M., Stiening, R., Weinberg, M. D., Schneider, S., Carpenter, J. M., Beichman, C., Capps, R., Chester, T., Elias, J., Huchra, J., Liebert, J., Lonsdale, C., Monet, D. G., Price, S., Seitzer, P., Jarrett, T., Kirkpatrick, J. D., Gizis, J. E., Howard, E., Evans, T., Fowler, J., Fullmer, L., Hurt, R., Light, R., Kopan, E. L., Marsh, K. A., McCallon, H. L., Tam, R., Van Dyk, S., and Wheelock, S.: 2006, *AJ* **131**, 1163

Smith, H. A., Church, J. A., Fournier, J., Lisle, J., Gay, P., Kolenberg, K., Carney, B. W., Dick, I., Peterson, R. C., and Hakes, B.: 2003, *PASP* **115**, 43

Smoot, G. F., Bennett, C. L., Kogut, A., Wright, E. L., Aymon, J., Boggess, N. W., Cheng, E. S., de Amici, G., Gulkis, S., Hauser, M. G., Hinshaw, G., Jackson, P. D.,

Janssen, M., Kaita, E., Kelsall, T., Keegstra, P., Lineweaver, C., Loewenstein, K., Lubin, P., Mather, J., Meyer, S. S., Moseley, S. H., Murdock, T., Rokke, L., Silverberg, R. F., Tenorio, L., Weiss, R., and Wilkinson, D. T.: 1992, *ApJl* **396**, L1

Soifer, B. T., Boehmer, L., Neugebauer, G., and Sanders, D. B.: 1989, *AJ* **98**, 766

Stothers, R. B.: 1983, *ApJ* **274**, 20

Strauss, M. A., Huchra, J. P., Davis, M., Yahil, A., Fisher, K. B., and Tonry, J.: 1992, *ApJS* **83**, 29

Strauss, M. A. and Willick, J. A.: 1995, *PhR* **261**, 271

Teerikorpi, P.: 1990a, *AAP* **234**, 1

Teerikorpi, P.: 1990b, *A&A* **234**, 1

Teerikorpi, P.: 1995, *Astrophysical Letters Communications* **31**, 263

Teerikorpi, P.: 1997, *ARAA* **35**, 101

Teerikorpi, P.: 1998, *AAP* **339**, 647

Theureau, G., Rauzy, S., Bottinelli, L., and Gouguenheim, L.: 1998, *AAP* **340**, 21

Tinto, M., Estabrook, F. B., and Armstrong, J. W.: 2002, *PhRvD* **65(8)**, 082003

Tonry, J. L., Schmidt, B. P., Barris, B., Candia, P., Challis, P., Clocchiatti, A., Coil, A. L., Filippenko, A. V., Garnavich, P., Hogan, C., Holland, S. T., Jha, S., Kirshner, R. P., Krisciunas, K., Leibundgut, B., Li, W., Matheson, T., Phillips, M. M., Riess, A. G., Schommer, R., Smith, R. C., Sollerman, J., Spyromilio, J., Stubbs, C. W., and Suntzeff, N. B.: 2003, *ApJ* **594**, 1

Trachternach, C., de Blok, W. J. G., McGaugh, S. S., van der Hulst, J. M., and Dettmar, R. .: 2009, *ArXiv e-prints*

Triay, R., Lachieze-Rey, M., and Rauzy, S.: 1994, *A&A* **289**, 19

Tully, R. B. and Fisher, J. R.: 1977, *AAP* **54**, 661

Udalski, A., Soszynski, I., Szymanski, M., Kubiak, M., Pietrzynski, G., Wozniak, P., and Zebrun, K.: 1999, *Acta Astronomica*

Valentine, H., Saunders, W., and Taylor, A.: 2000, *MNRAS* **319**, L13

Wakamatsu, K., Colless, M., Jarrett, T., Parker, Q., Saunders, W., and Watson, F.: 2003, in S. Ikeuchi, J. Hearnshaw, and T. Hanawa (eds.), *The Proceedings of the IAU 8th Asian-Pacific Regional Meeting, Volume I*, Vol. 289 of *Astronomical Society of the Pacific Conference Series*, pp 97–104

Wang, L., Goldhaber, G., Aldering, G., and Perlmutter, S.: 2003, *ApJ* **590**, 944

Wang, L., Strovink, M., Conley, A., Goldhaber, G., Kowalski, M., Perlmutter, S., and Siegrist, J.: 2006, *ApJ* **641**, 50

Weinberg, D.: 1995, in S. J. Maddox & A. Aragon-Salamanca (ed.), *Wide Field Spectroscopy and the Distant Universe*, pp 129–+

Wheeler, J. C., Piran, T., and Weinberg, S. (eds.): 1990, *Jerusalem Winter School for Theoretical Physics. Supernovae. Volume 6, Jerusalem, Dec. 28, 1988- Jan. 5, 1989.*

Willick, J. A.: 1991, *Ph.D. thesis*, California Univ., Berkeley.

Willick, J. A.: 1994, *ApJS* **92**, 1

Willick, J. A.: 1996, *ArXiv Astrophysics e-prints*

Willick, J. A., Davis, M., Dekel, A., and Shaya, E.: 2000, in S. Courteau & J. Willick (ed.), *Cosmic Flows Workshop*, Vol. 201 of *Astronomical Society of the Pacific Conference Series*, pp 321–+

Willick, J. A. and Strauss, M. A.: 1998, *ApJ* **507**, 64

Wright, E. L., Meyer, S. S., Bennett, C. L., Boggess, N. W., Cheng, E. S., Hauser, M. G., Kogut, A., Lineweaver, C., Mather, J. C., Smoot, G. F., Weiss, R., Gulkis, S., Hinshaw, G., Janssen, M., Kelsall, T., Lubin, P. M., Moseley, Jr., S. H., Murdock, T. L., Shafer, R. A., Silverberg, R. F., and Wilkinson, D. T.: 1992, *ApJ1* **396**, L13

Yahil, A., Strauss, M. A., Davis, M., and Huchra, J. P.: 1991, *ApJ* **372**, 380